

**Low Temperature Transport  
and Evidence for Nuclear Order  
in GaAs Quantum Wires**

Inauguraldissertation

zur

Erlangung der Würde eines Doktors der Philosophie

vorgelegt der

Philosophisch-Naturwissenschaftlichen Fakultät

der Universität Basel

von

**Christian Ph. Scheller**

aus Basel, Schweiz



Basel, 2014

Genehmigt von der Philosophisch-Naturwissenschaftlichen Fakultät auf Antrag von

Prof. D. M. Zumbühl

Prof. O. Auslaender

Dr. B. Braunecker

Basel, den 23. April 2013

Prof. Dr. Jörg Schibler  
(Dekan)

## Abstract

In this thesis we focus on low temperature transport through cleaved edge overgrowth (CEO) quantum wires. This thesis is motivated by recent theoretical work on one hand that predicts the formation of a nuclear helimagnet in presence of a Luttinger liquid (LL) below a critical system temperature [1] and previous measurements on CEO wires on the other hand that might indicate the onset of such a phase transition [2].

The first task for this thesis was to create suitable measurement conditions to approach the theoretically predicted strongly correlated state of matter. More precisely, electron sample temperatures much lower than the predicted ordering temperature of 75 mK for GaAs CEO wires have to be demonstrated. For this purpose, cryogenic microwave filters with very low cut-off frequency and good thermalization properties were developed and installed for all measurement cables. With that a minimum electron temperature of 7.5 mK was reached in metallic coulomb thermometers [3], and furthermore, for the first time in these devices, a deviation from pure electron-phonon cooling is observed [4].

At low refrigerator temperatures  $T_R$ , the CEO (double) wires show pronounced and completely reproducible conductance oscillations as a function of density. We show that these oscillations, also present in the zero magnetic field tunneling current between the parallel quantum wires, emerge as 1D Fabry Perot resonances in the ballistic CEO wires [5]. We analyze the maximum transmission ( $T = 1$ ) through these wires, i.e. the oscillation maxima, in the single mode regime as a function of temperature. While the quantum wires approach universal conductance quantization of  $2e^2/h$  for a single quantum wire only at quite large  $T_R \gtrsim 15$  K, we find that the conductance saturates below  $T_R \approx 75$  mK at  $\approx 1e^2/h$  [6]. Furthermore, we give strong evidence that the conductance saturation is not related to insufficient thermalization, i.e. the CEO wires cool far beyond the saturation temperature of  $\approx 75$  mK. This seems to indicate lifting

of electron spin degeneracy at zero external magnetic field, consistent with the theoretically predicted low temperature limit for a clean LL in the ordered helical state [1]. We can further exclude other potential mechanisms (temperature dependent contact resistance, freeze-out of weakly disordered LL, Wigner crystal formation/incoherent LL), leaving only nuclear spins as candidates for the source of the (possibly) observed lifted spin degeneracy as spin-orbit coupling is rather weak in GaAs, and the saturation at  $1e^2/h$  is observed in absence of an external magnetic field. This might resolve the long-standing mystery of the temperature-dependent (non-universal) conductance quantization in GaAs cleaved edge overgrowth quantum wires, and furthermore might give first experimental evidence for a new, strongly correlated state of matter, namely (helical) nuclear order induced by the strongly interacting electrons via hyperfine coupling.

We also measure real-time tunneling in a GaAs few electron double quantum dot (DQD) by means of an adjacent quantum dot as charge sensor. At low temperatures, in the limit of negligible interdot tunneling and low tunnel rates to source and drain, we observe metastable charge state switching. The metastability only occurs within diamond shaped regions that are centered between associated triple points of the charge stability diagram (CSD). We show that these charge fluctuations arise as an intrinsic property in DQDs, and take place via fast intermediate states that include an electron exchange with the leads [7]. Due to the geometrical shape of the diamond (in very good agreement with our model of thermally activated electron exchange with the leads), its large energy scale ( $>1.7\text{K}$ ) and due to its visibility even at charge sensor bias voltages as small as  $5\mu\text{V}$ , we exclude extrinsic effects such as phonon or photon assisted tunneling. Furthermore, the simultaneous observation of the diamond shaped region of metastable charge state switching at various points in the CSD and its pinning to associated triple points upon reshaping the DQD, make charge traps and other defects a very unlikely explanation.

# Contents

<b>1</b>	<b>Background</b>	<b>9</b>
1.1	Measurement environment . . . . .	10
1.1.1	Refrigerator temperature . . . . .	10
1.1.2	CMN thermometer . . . . .	11
1.2	GaAs quantum dots . . . . .	13
1.3	GaAs double quantum dots . . . . .	19
1.4	Resistively detected NMR . . . . .	22
1.4.1	Introduction to NMR . . . . .	22
1.4.2	RDNMR setup and assembly . . . . .	25
1.4.3	RDNMR in the (fractional) quantum hall regime . . . . .	27
1.4.4	Identification of different isotopes . . . . .	28
<b>2</b>	<b>Silver Epoxy Microwave Filters for Thermalization below 10 mK</b>	<b>31</b>
2.1	Motivation and main experimental results . . . . .	32
2.2	Cryogenic microwave filters . . . . .	33
2.2.1	Filter thermalization and attenuation . . . . .	33
2.2.2	Filter fabrication and characterization . . . . .	34
2.3	Electron temperature measurements . . . . .	36
2.3.1	Quantum dot thermometer . . . . .	36
2.3.2	Electron temperature with CMFs . . . . .	37
2.3.3	Electron temperature without CMFs . . . . .	39
2.3.4	Metallic coulomb blockade thermometer . . . . .	40
2.4	Summary . . . . .	41
2.5	Supplemental Materials . . . . .	43

<b>3</b>	<b>Metallic Coulomb Blockade Thermometry down to 10 mK and below</b>	<b>47</b>
3.1	Motivation . . . . .	48
3.2	Strategy to approach submilikelvin sample temperatures . . . . .	48
3.2.1	Nuclear refrigerator and microwave filtering scheme . . . . .	48
3.2.2	Performance of the nuclear refrigerators . . . . .	50
3.3	Electron temperature measurements . . . . .	50
3.3.1	CBT sample overview . . . . .	50
3.3.2	CBT performance for different sensors . . . . .	51
3.4	CBT cooling mechanism . . . . .	52
3.4.1	Theoretical model including EP and WF cooling . . . . .	52
3.4.2	Measured cooling power-laws versus theory . . . . .	53
3.5	Summary . . . . .	54
<b>4</b>	<b>Luttinger Liquid Theory and GaAs CEO Wires</b>	<b>57</b>
4.1	Basic introduction to Luttinger liquids . . . . .	59
4.1.1	Luttinger liquid versus Fermi liquid . . . . .	59
4.1.2	Physical properties of Luttinger liquids . . . . .	60
4.1.3	Conductance quantization in 1D . . . . .	61
4.2	Luttinger liquid and nuclear spins . . . . .	63
4.2.1	Nuclear magnetism and electron order in a Luttinger liquid . . . . .	63
4.2.2	Spin selective Peierls in a 1D wire with SOI . . . . .	65
4.3	Nonuniversal conductance quantization in quantum wires . . . . .	66
4.4	GaAs cleaved edge overgrowth (double) quantum wires . . . . .	69
4.4.1	Sample fabrication . . . . .	70
4.4.2	Sample properties before and after LED illumination . . . . .	72

4.4.3	Disentangling lower and upper wire modes . . . . .	75
4.4.4	Ballistic addition of wires . . . . .	77
4.4.5	Electron localization in the pinch off regime . . . . .	80
4.4.6	Electron density of upper and lower wire modes . . . . .	83
4.5	CEO wires as 1D electronic Fabry-Perot resonators . . . . .	90
4.5.1	Fabry-Perot resonances in the tunneling current . . . . .	90
4.5.2	Fabry-Perot resonances in the upper quantum wire . . . . .	94
<b>5</b>	<b>Possible Evidence for Helical Nuclear Spin Order in GaAs Quantum Wires</b>	<b>97</b>
5.1	Motivation . . . . .	98
5.2	Main experimental findings . . . . .	98
5.3	CEO wire sample . . . . .	99
5.4	Temperature dependence . . . . .	100
5.5	DC bias and B-field dependence . . . . .	102
5.6	Comparison with theoretical predictions . . . . .	104
5.7	Summary and Conclusions . . . . .	107
<b>6</b>	<b>Thermally Activated Charge Fluctuations in a Few Electron GaAs Double Quantum Dot</b>	<b>109</b>
6.1	Motivation . . . . .	110
6.2	Experimental findings . . . . .	110
6.3	Sample fabrication and charge stability diagram . . . . .	111
6.4	Metastable region in the CSD . . . . .	112
6.5	Analysis of the measured real-time data . . . . .	114
6.6	Time resolved 4-level system in the metastable region . . . . .	116

6.7	Extension of the orthodox theory for transport in DQDs . . . . .	117
6.7.1	Discrepancies between measured data and theoretical predictions	120
6.8	Summary . . . . .	121
<b>7</b>	<b>Summary and Outlook</b>	<b>123</b>
	<b>Bibliography</b>	<b>130</b>
	<b>List of Figures</b>	<b>148</b>
	<b>Acknowledgments</b>	<b>151</b>
	<b>CV</b>	<b>153</b>



# 1 Background

Temperature is the most important tunable knob in this thesis with focus on transport measurements in cleaved edge overgrowth quantum wires. In fact, our main experimental finding is a low temperature saturation of reduced conductance steps in these wires that is not related to a saturating electron temperature. To back up our conclusions, reliable and verified thermometry is a basic requirement.

In this chapter we will introduce different thermometers that were used to determine the refrigerator temperature, and give the background for electron temperature measurements with a GaAs quantum dot. While dilution refrigerators with low base temperature in the few millikelvin regime are commercially available, quite some additional efforts have to be made in order to reduce the electron sample temperature down to a similar regime. In chapter 2 we present new cryogenic microwave filter that were developed for this purpose, together with electron temperature measurements using a GaAs quantum dot and metallic coulomb blockade thermometers (CBTs) [3]. Electron temperatures in CBTs are further investigated in chapter 3 with focus on the underlying cooling mechanism [4].

In chapter 4 we give a brief introduction to Luttinger liquid physics and nuclear order in 1D conductors, followed by previous experimental findings and an introduction to the CEO wires used in this work. We measure the electron density using tunnel spectroscopy [8] and verify the transition to electron localization [8, 9] at low densities as well as ballistic transport [10]. Furthermore we identify Fabry-Perot resonances [5], a manifestation of ballistic transport. Then we move on to transport measurements in CEO wires (chapter 5), i.e. we analyze the reduced conductance steps in CEO wires as a function of temperature [6].

In the last chapter we focus on intrinsic temperature activated metastable charge state switching in a GaAs few electron double quantum dot.

## 1.1 Measurement environment

A very broad range of temperatures has been addressed in experimental physics, ranging from several hundreds of picokelvins [11, 12], achieved in Bose-Einstein condensates and nuclear cooling of Rhodium spins, up to a few trillion degrees in quarks-gluon plasmas [13]. Depending on the regime and the system under study, measuring temperature can be quite challenging, and requires thermometers that are suitable for the specific situation. All experiments in this work were performed on  $^3\text{He} - ^4\text{He}$  dilution refrigerators (DRs), where temperature can be typically varied from a few milikelvin up to a few Kelvin.

### 1.1.1 Refrigerator temperature

The DRs are equipped with  $\text{RuO}_2$  resistors that are commonly used as thermometers in that regime. They are mounted on the mixing chamber plate which is very well thermally coupled to the mixing chamber (MC), the core of any DR. Actual samples are mounted on a sample holder that is attached to a coldfinger (CF). Our CF is an extension made from copper that is attached to the mixing chamber plate, and allows sample measurements in (large) external magnetic fields while B-fields at the MC-plate are kept small. Due to small gradients between the MC-plate and the sample holder, the actual temperature of e.g. the sample backplane is slightly larger than the MC-temperature. In the following we will ignore these small temperature gradients and use the temperature, measured with a  $\text{RuO}_2$  resistor at the MC-plate, as a synonym for the refrigerator temperature  $T_R$ . The  $\text{RuO}_2$  resistors are precalibrated with a fixed point device to convert between the measured resistance and refrigerator temperature  $T_R$  using a 7<sup>th</sup> order polynomial. The fixed point device itself is a primary thermometer where a series of superconductors with different (known) transition temperatures serves as an absolute temperature scale. In the following section, we cross check the precalibrated  $\text{RuO}_2$  thermometer with a CMN thermometer.

### 1.1.2 CMN thermometer

CMN is a paramagnetic salt, with a ferromagnetic ordering temperature  $T_C$  in the low milikelvin regime ( $T_C = 1-2$  mK, see e.g. Pobell, "Matter and Methods at Low Temperatures" [14]). In the high temperature phase (para phase), the magnetic susceptibility  $\chi_m$  follows a Curie-Weiss law:

$$\chi_m(T) = \frac{C}{T - \Delta} \quad (1)$$

The Weiss constant  $\Delta$  depends on experimental details such as the shape of the sample and crystal symmetry of the salt. The Curie constant  $C$  depends on the amount of CMN salt used (number of moles  $N_0$ ) and is given by  $C = N_0 J(J+1) \mu_0 \mu_B^2 g^2 / 3k_B$  [14]. Here  $J$  denotes the total angular momentum quantum number,  $\mu_B = 58.9 \mu\text{eV}/\text{T}$  the Bohr magneton,  $\mu_0$  the vacuum permeability and  $k_B$  the Boltzmann constant. The Curie-Weiss law, shown in eq.1 is the basic principle of a CMN thermometer. The magnetic susceptibility is measured indirectly via the mutual inductance  $L$  of a pair of concentric coils with the CMN salt as center material. The primary coil is excited with an alternating current  $I(\omega)$  leading to an oscillating magnetic field  $B(t) = (1 + \chi_m) B_0(t)$ .  $B_0(t)$  denotes the magnetic field in absence of the paramagnetic salt (or equivalently, with the salt but in the limit of high temperatures). The change in magnetic flux induces a voltage in the secondary coil. According to Lenz' rule, the induced voltage is given by:

$$U_{ind} = -L(t) \frac{dI}{dt} = - \left( 1 + \frac{C}{T_{CMN} - \Delta} \right) \underbrace{\frac{\mu_0 N_P N_S A}{l}}_{L_0} \underbrace{\frac{dI}{dt}}_{\omega I_0 \cos(\omega t)} \quad ; \quad I(\omega) = I_0 \sin(\omega t) \quad (2)$$

$N_P$ ,  $N_S$  are the number of windings for the primary and secondary coil,  $A$  the cross section and  $l$  the length of the coils. As evident from eq.2, the induced voltage scales linearly with the excitation frequency. Changing the frequency is a good experimental

tool for testing whether or not the measured signal is purely inductive. A measurement of the mutual inductance as a function of refrigerator temperature  $T_R$  is shown in fig. 1. In practice for a CMN thermometer to work properly, external magnetic fields have to be suppressed since the CMN temperature  $T_{CMN}$  is gained through a B-field measurement. For this purpose a Nb-shield covers the active part of the device. In the superconducting state the Nb-shield expels external B-fields due to the Meissner-Ochsenfeld effect [15].

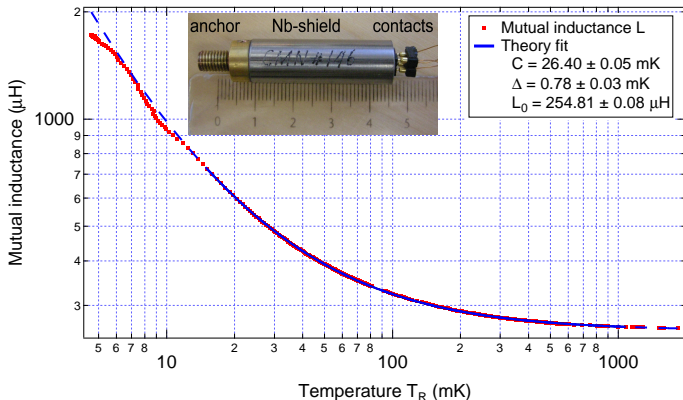


Figure 1: Mutual inductance of a CMN thermometer versus mixing chamber temperature  $T_R$ , measured with a  $\text{RuO}_2$  thermometer. The solid blue trace is a fit to the data in the regime  $15 \text{ mK} < T_R < 1 \text{ K}$  using eq. 2. The same fit is shown for the whole temperature range as dashed blue trace. Fit parameters are indicated in the legend. The inset shows a picture of the CMN thermometer (small coil, from Leiden Cryogenics).

Using eq.2, we fit the data in fig.1 in the temperature range  $15 \text{ mK} < T_R < 1 \text{ K}$  (solid blue trace), where we believe the  $\text{RuO}_2$  calibration to be quite accurate. For comparison, in dashed blue, we also show the same fit but plotted over the whole temperature range. From the curve fit, we can extract the mutual inductance between the coils (in absence of the CMN salt),  $L_0 \approx 250 \mu\text{H}$ , the Curie constant  $C \approx 26 \text{ mK}$  and a Weiss constant of  $\Delta = 0.8 \text{ mK}$ . Also, the measured mutual inductance can be converted back to a temperature  $T_{CMN}$  if  $T_R$  is well above the ordering temperature of the CMN salt ( $T_R \gtrsim 5 \text{ mK}$ , see ref. [14]). As shown in fig. 2, CMN and  $\text{RuO}_2$  thermometer temperature agree quite well and only start deviating a little towards base temperature of the DR. As

a guideline to the eye, we also plot the ideal case, where CMN and RuO<sub>2</sub> thermometer agree perfectly,  $T_{CMN} = T_R$ .

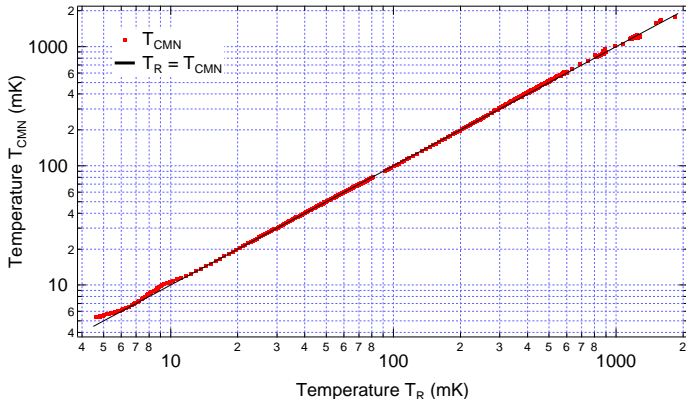


Figure 2: Mutual inductance of a CMN thermometer, converted to temperature  $T_{CMN}$  and plotted versus mixing chamber temperature  $T_R$  (RuO<sub>2</sub> thermometer). The black trace is a guideline to the eye and indicates the ideal case  $T_{CMN} = T_R$ .

The larger deviations at lower temperatures probably arise from different time constants in the thermalization of the paramagnetic salt and the RuO<sub>2</sub> semiconductor respectively. The system temperature was increased from base temperature by switching off the turbo pumps for the <sup>3</sup>He – <sup>4</sup>He circulation system of the DR. This initially leads to a quite fast temperature changes which then, due to different thermalization time constants, inevitably lead to different CMN and RuO<sub>2</sub> temperatures.

## 1.2 GaAs quantum dots

GaAs quantum dots (QDs) are tiny islands with a small but adjustable amount of electrons. Because of their small size (tens of nanometers up to microns) which is comparable to the typical Fermi wavelength in these system  $\lambda_F \approx 50 - 100$  nm, a quantum mechanical description is required leading to discrete energy states. Due to their similarities in the energy spectrum, quantum dots can be viewed as artificial (tunable) atoms [16, 17]. QDs have been extensively studied in the past decades in many different

material systems. Examples are SETs (single electron transistors), self assembled QDs e.g. in InAs-InGaAs heterostructures (here, strain due to lattice mismatch is responsible for the formation of QDs), etched QDs on Graphene, NV-centers in Diamond (Nitrogen Vacancies), surface gated QDs e.g. on GaAs/AlGaAs heterostructures and many more. The QD experiments in chapters 2, 6 are done on GaAs double quantum dots (DQDs) fabricated by Kristine Bedner and Daniel Biesinger respectively. Starting point for the fabrication is a GaAs heterostructure. The triangular potential well which forms at the GaAs-AlGaAs interface, traps free electrons from the above Si-doping layer. At temperatures below  $\approx 100$  K only the lowest subband of the triangular well remains populated [18], resulting in a very clean two dimensional electron gas (2DEG) with mobilities  $\mu$  of several million  $\text{cm}^2/\text{Vs}$ . Standard electron beam lithography is used to pattern Ti/Au surface gates and Au/Ge Ohmic contacts. The surface gates allow for depletion and shaping of the underlying electron gas, whereas the Ohmics serve as source and drain contacts for electrical studies on the QD. The focus of this section will be on simple transport through a QD, which will allow to use QDs as electron thermometers. An overview on QDs can be found e.g. in ref. [19]. A schematic of a QD is shown in fig. 3.

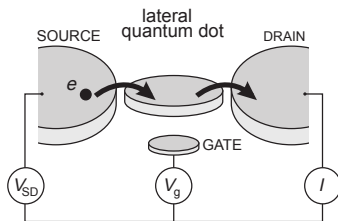


Figure 3: Schematic of a lateral quantum dot, taken from ref. [20]. The quantum dot, indicated as disc, is separated by tunnel barriers from source and drain contacts. A capacitively coupled gate  $V_g$  controls the chemical potential in the quantum dot.

The quantum dot is a small region of the 2DEG that was separated from the surrounding 2DEG (by means of surface gates), leaving only tunneling contacts to source and drain. A capacitively coupled gate  $V_g$  allows the chemical potential  $\mu$  to be changed in the quantum dot. For sufficiently large negative gate voltage  $V_g$  all electrons are pushed out of the quantum dot, leaving an empty island. Upon increasing  $V_g$  to less negative

voltages, electrons can be filled in one by one. The addition energy  $E_{add}$  for adding the next electron depends on the number  $N$  of electrons already present in the QD and is defined via the QD chemical potential [20]:

$$E_{add.} = \mu(N + 1) - \mu(N) = E_C + \Delta E \quad (3)$$

$E_C$  denotes the charging energy, a purely electrostatic term and  $\Delta E$  is the quantum mechanical level spacing. In practice, this addition energy can easily be extracted by measuring the differential conductance through the QD. Hereby, the source is modulated with a small AC excitation  $V_{SD}$  (few  $\mu\text{V}$  and frequency typically in the hertz regime), and the alternating current is measured at the drain. The differential conductance  $dI/dV_{SD}$  peaks whenever source or drain are aligned with a quantum dot level (see left inset in fig. 4). A schematic differential conductance trace as a function of gate voltage  $V_g$  and zero source-drain bias is shown in fig. 4.

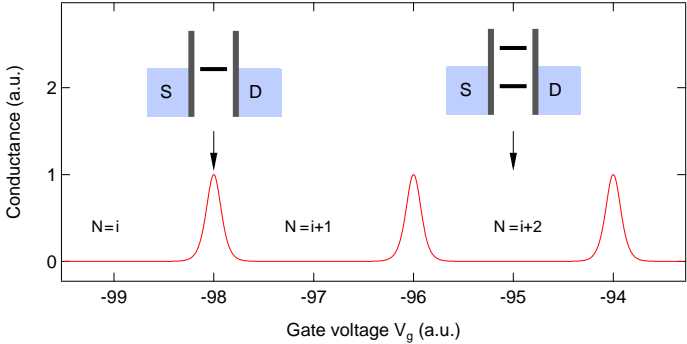


Figure 4: Schematic differential conductance trace (red) as a function of gate voltage. The situation is depicted for the case of zero applied DC-bias, i.e. source and drain chemical potential are aligned. Electron numbers  $N$  are indicated. Insets show the energy level diagram for the resonant (conductance peak, alignment of source-drain-dot level) and off-resonant case (in between peaks).

In the following, we will use the term conductance to label the differential conductance unless explicitly stated differently. Since between conductance peaks the charge on the QD is fixed, and at least the charging energy  $E_C$  has to be provided to fill in the next

electron; these peaks are referred to as coulomb blockade peaks. The off-resonant case in between coulomb blockade peaks is depicted in the inset on the right in fig. 4. In the limit of large tunneling rates  $\Gamma_{S/D}\hbar \gg k_B T$  the peak width is determined by lifetime broadening of the QD level, i.e. by the rate  $\Gamma_t$  at which electrons tunnel out of the QD [21]:

$$G = \frac{2e^2}{h} \frac{\Gamma_S \Gamma_D}{\Gamma_S + \Gamma_D} \left( \frac{\Gamma_t}{\left(\frac{\Gamma_t}{2}\right)^2 + \left(\frac{e\alpha}{h} \Delta V_g\right)} \right); \quad \Gamma_t = \Gamma_S + \Gamma_D \quad (4)$$

The conversion between  $V_g$  and corresponding energy  $E = -e\alpha\Delta V_g$  is done by means of the leverarm  $\alpha = C_G/C_{tot}$ , defined as ratio of gate capacitance  $C_G$  to the total quantum dot capacitance  $C_{tot}$ . It is therefore a measure of how efficient  $V_g$  shifts the QD levels.

At lower tunnel rates  $k_B T \approx \Gamma_{S/D}\hbar$  both, life time broadening and thermal broadening of the Fermi function in the leads, contribute to the peak width. When reducing the tunnel rates even further ( $\Gamma_{S/D}\hbar \ll k_B T$ ) a regime is entered where the conductance peak width is determined solely by the electron temperature in the leads. The transition between temperature and life time broadened conductance peaks is demonstrated in ref. [22]. For a QD with large level spacing  $\Delta \gg k_B T$  compared to temperature  $T$ , the conductance (in the  $k_B T \ll \Gamma_{S/D}\hbar$  limit) as a function gate voltage  $\Delta V_g$ , measured in relation to the center of the conductance peak, reads [21]:

$$G = \frac{2e^2}{h} \frac{\Gamma_S \Gamma_D}{\Gamma_S + \Gamma_D} \frac{\hbar}{4k_B T} \cosh^{-2} \left( \frac{e\alpha \Delta V_g}{2k_B T} \right) \quad (5)$$

Once the leverarm  $\alpha$  is known, the measured conductance peak width  $\Delta V_g$  can be converted to the corresponding electron temperature of the leads. The leverarm can be measured by applying a known DC bias and observing the splitting of the coulomb blockade peaks into two conductance peaks that correspond to alignment of the QD level with either source or drain.

An example of a coulomb blockade peak, measured in the temperature broadened



regime, is shown below in fig. 5 (red trace) together with a theory curve (dashed curve), created using eq. 5. At the position of the conductance peak, where source and drain chemical potential align with the QD level (red trace), the simultaneously recorded DC current remains zero since no DC bias is applied (dark blue trace).

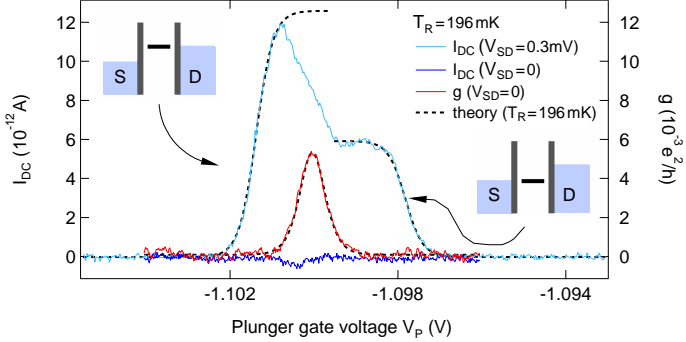


Figure 5: DC-current through the QD (light blue) measured at 196 mK and finite source-drain bias  $V_{SD} = 0.3$  mV. Insets schematically depict the QD energy level configuration at the raising and falling edge of the DC current, corresponding to alignment of QD level with drain and source. We additionally plot the measured conductance  $g$  at zero source drain bias (red) as a function of gate voltage  $V_g$  along with the simultaneously recorded DC-current (dark blue). Dashed lines represent theory current and conductance curves for  $T_R = 196$  mK.

To get rid of (drifting) DC-offsets arising from small offsets in the measurement instrumentation (e.g. IV-converter), we use a feedback mechanism that minimizes the DC-current in the effectively zero bias measurements.

Along with the zero bias measurements, fig. 5 shows the DC current  $I_{DC}$ , recorded at finite source drain bias  $V_{SD} = 0.3$  mV. Current transport only takes place when a QD level lies in between source and drain chemical potential. In a simple model, the magnitude of  $I_{DC}$  is given by the tunnel barriers and is independent of the applied DC bias as long as it is small enough for excited states not to contribute to the current. For the DC current shown in fig. 5, recorded at moderate DC bias, this is not the case and a double step is observed. A mapping of the excited states in a GaAs QD and comparison to a theoretical model has been done by Foxman *et al.*, see ref. [22]. In this work we

will use the DC current to (separately) monitor the electron temperature of source and drain. Apart from the tunnel barriers, the current through the device depends on the number of available states in the leads, i.e. the density of states (DOS) and on the quantum statistics for the particles involved (Fermi-Dirac statistics for electrons and fermions in general). For two dimensional leads the density of states (DOS) is independent of energy,  $DOS_{2D} = m/\pi\hbar^2$ . In this case and in the limit of small tunneling rates to source and drain ( $\Gamma_S, \Gamma_D \ll k_B T/\hbar \ll \Delta$ ), the raising (falling) edge of the current profile reflects the Fermi-Dirac distribution in the leads.

$$f(T) = (1 + \exp(\alpha\Delta V_g/k_B T))^{-1} \quad (6)$$

$\Delta V_g$  is the gate voltage  $V_g$ , measured from the position at which the corresponding current step reaches (drops to) half its height. As for the conductance peak, the lever-arm  $\alpha$  is required to convert between measured width of the Fermi distribution and temperature. In contrast to the conductance measurements, a single current trace is in principle self calibrating since  $\alpha = eV_{SD}/(V_{G2} - V_{G1})$ , where  $V_{G1}, V_{G2}$  denote inflection points of the Fermi distributions. In practice, accurate temperature measurements require precise knowledge of the applied bias  $V_{SD}$ , which can only be gained by compensating the DC offset beforehand. From the width of the current window in fig. 5, recorded at a refrigerator temperature of 196 mK and  $V_{SD} = 0.3 \text{ mV} + V_{\text{offset}}$ , we extract  $\alpha = 83 \mu\text{eV/mV}$ . Theory curves (dashed lines in fig. 5) for the current and conductance profile in the temperature broadened regime using  $T=196 \text{ mK}$  and  $\alpha = 83 \mu\text{eV/mV}$  agree very well with measured curves.

In comparison, the DC-method allows extraction of both source and drain reservoir temperatures separately, an advantage over the  $V_{DC} = 0$  AC-method. In addition, the DC method does not require careful zeroing of the DC voltage bias (although  $V_{DC}$  drifts still need to be small on the time-scale of the  $I_{DC}$  measurement). Also, applying a large DC voltage bias  $e \cdot V_{DC} \gg k_B T$  does not induce self-heating here since tunnel-rates and resulting currents (in the temperature broadened case) are very small and independent of  $V_{DC}$ . The absence of such  $V_{DC}$  bias-induced self heating was also experimentally

investigated where no dependence of the extracted electron base temperature was found for various applied  $200 \mu\text{V} \gtrsim V_{DC} \gg k_B T$ . Further, the temperatures extracted from  $I_{DC}$  at large  $V_{DC}$  are the same as temperatures extracted at  $V_{DC} = 0$  with the AC-method via the differential conductance, confirming the DC-method as valid and very useful resource. However, for the temperatures extracted with the AC-method, careful zeroing of the DC voltage bias is crucial and great care must be taken to keep the  $V_{AC}$  bias small ( $\ll k_B T$ ) to prevent AC modulation induced broadening of the CB peak. Thermometry using GaAs QDs and metallic coulomb blockade thermometers as well as cooling mechanisms and limitations on the measured electron temperature are the topic of chapters 2 and 3.

### 1.3 GaAs double quantum dots

It seems straight forward to extend the theory for QDs to double quantum dots (DQDs). Two gates  $V_{G1}$  and  $V_{G2}$  capacitively coupled to QD1 and QD2 respectively, are necessary to achieve full control over the charge states in the DQD system, whereas a single one was sufficient for a single QD (see fig.3). In the limit of negligible capacitive coupling between the dots, gate  $V_{G1}$  only affects the number of electrons  $N_1$  on QD1 and vice versa, i.e. the addition energy for QD1 does not depend on the charge state of QD2. In this limit, the DQD is equivalent to a system composed of two individual quantum dots that are separated enough such that mutual coulomb interactions are negligible. This leads to electron configurations  $(N_1, N_2)$  in the charge stability diagram (CSD) where four different charge states coexist. The situation is depicted in fig. 6(a). A red dot indicates the quadruple point where the charge states  $(0,0)$ ,  $(1,0)$ ,  $(0,1)$  and  $(1,1)$  are degenerate.

Upon reducing the distance between individual QDs the coulomb interaction gains in strength and finally, for closely spaced QDs, introduces large interdot coupling. The situation for a DQD with significant interdot coupling is depicted in fig. 6(b). Due to the coupling, a change in the chemical potential  $\mu_2(N_1, N_2)$  on QD2 also alters the chemical potential  $\mu_1(N_1, N_2)$  on QD1. Note that no actual change in the electron number  $N_2$

on QD2 is necessary to change the chemical potential on QD1. Due to the (capacitive) interdot coupling, charge transition lines are no longer horizontal and vertical with respect to the gates  $V_{G1}$  and  $V_{G2}$ . More drastically, however, the quadruple points split up in pairs of triple points. For example, the lowest quadruple point (red dot in fig. 6a), sharing the charge states (0,0), (1,0), (0,1) and (1,1), splits up into a lower triple point (0,0), (1,0), (0,1) and a higher triple point (1,0), (0,1), (1,1), indicated as red and blue point in fig. 6(b).

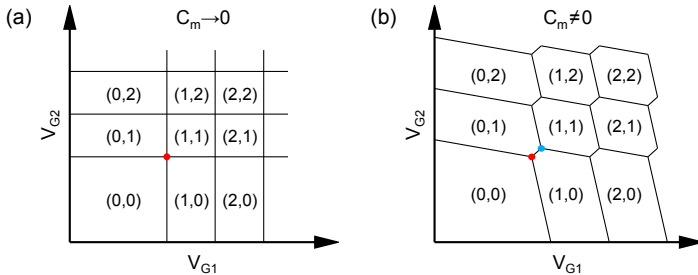


Figure 6: Charge stability diagram for a double quantum dot with and without interdot coupling  $C_m$  is shown in (b) and (a) respectively. The electron numbers  $N_1$  and  $N_2$  on quantum dots 1 and 2 are controlled by capacitively coupled gates  $V_{G1}$  and  $V_{G2}$ . The lowest quadruple point in (a) and corresponding triple points in (b), are indicated as colored dots. This graph was taken and modified from ref. [23].

Along the zero detuning line  $\mu_1(1,0) = \mu_2(0,1)$ , connecting the lower and higher triple point in fig. 6(b), the two charge states (1,0) and (0,1) are degenerate. A zoom in on the CSD in the  $N_1 = 0/1$ ,  $N_2 = 0/1$  region is given in fig. 7.

Fat black lines split up the CSD in four regions with the energetically most favorable charge states  $(N_1, N_2)$  as indicated. In the (0,0) region both chemical potentials  $\mu_1(1,0)$  and  $\mu_2(0,1)$  lie above the chemical potential of the leads  $\mu_{\text{leads}}$ . Consequently (0,0) is the only charge configuration that is energetically allowed in the (0,0) region. Similar arguments hold for (1,1) region. The situation is more complicated when one electron is present in the DQD. We only focus on the (0,1) region since the situation for the (1,0) configuration is given by symmetry arguments. The (0,1) region can be separated into the light blue and purple colored parts as shown in fig. 7. For the light blue area

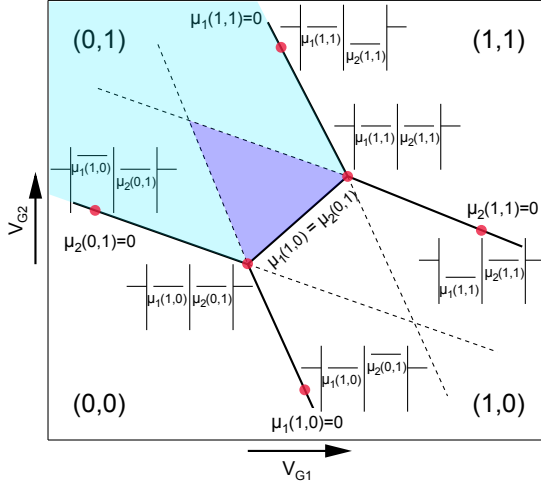


Figure 7: Double quantum dot charge stability diagram (CSD) in the vicinity of the  $\mu_1(1,0) = \mu_2(0,1)$  zero detuning line. Insets schematically depict the alignment of the quantum dot levels with respect to source and drain chemical potential for prominent points (red) in the CSD. The  $(1,0)$  charge configuration is separated into light and dark blue colored regions according to whether or not  $\mu_2(0,1) < \mu_{1\text{leads}}$  is satisfied, see main text. This was graph taken and modified from ref. [23].

the situation is similar to the case of the  $(0,0)$  and  $(1,1)$  charge configurations i.e. only the  $(0,1)$  charge state is energetically allowed. In the purple area however both,  $\mu_1(1,0)$  and  $\mu_2(0,1)$  lie below the chemical potential of the leads. In the limit of small tunnel rates to source and drain, low electron temperatures and negligible interdot tunneling, an electron can spend a noticeable amount of time in the energetically less favorable  $(1,0)$  state before the  $(0,1)$  configuration is restored through electron exchange with the leads via the intermediate  $(0,0)$  or  $(1,1)$  states. We note that though larger interdot tunneling obscures the presence of this metastability, it does not suppress the effect. Finally, these considerations are not restricted to the  $(0,1)$ - $(1,0)$  transition in GaAs DQDs but equally apply to any transition  $(k,m+1)$ - $(k+1,m)$  in a DQD system.

The metastability, which results from two simultaneously available charge states in a DQD and its consequences e.g. for spin manipulation experiments, are studied in detail in chapter 6.

## 1.4 Resistively detected NMR

### 1.4.1 Introduction to NMR

Nuclear Magnetic Resonance (NMR) provides a very sensitive tool to measure the magnetic environment in a noninvasive way. It is widely used in various fields e.g. chemistry for structure analysis, for the study of biological samples (RNA, DNA, proteins) or medical applications such as MRI (Magnetic Resonance Imaging).

Here we use resistively detected nuclear magnetic resonance (RDNMR) in an attempt to directly measure (possible) nuclear order in GaAs quantum wires. We note, however, that from a theoretical point of view it is difficult to predict the response of a nuclear spin helix to NMR excitation (flipping of single nuclear spins becomes energetically extremely unfavorable in the ordered state). While we observe clear RDMNR signals in the quantum hall regime, no conclusive data could be gained for the quantum wires. As a consequence, only a few preliminary (not understood) measurements on QWs are shown in the outlook. In this section, after introducing the basic principles of NMR and RDNMR, we present the assembly of our RDNMR setup and some proof-of-principle experiments in the (fractional) quantum hall regime.

When placing a particle with spin in an external magnetic field  $B_0$ , its energy becomes spin dependent. As a consequence, the initially degenerate spin states shift in energy  $\Delta E$ . Using standard nomenclature for NMR, the energy shift can be expressed as:

$$\Delta E = -\mu B_0 = -\gamma m \hbar B_0 \quad (7)$$

Here,  $\mu$  denotes the magnetic moment,  $m$  the magnetic quantum number,  $\gamma$  the gyro-magnetic ratio and  $\hbar = 2\pi\hbar$  is the Planck constant. In the case of a free electron the magnetic quantum number can take the values  $m = \pm\frac{1}{2}$ . In an external magnetic field an electron can therefore take two different spin states that are separated by the energy  $E = \gamma\hbar B_0$  or equivalently and commonly used for the case of electrons  $E = g\mu_B B_0$ . Here,  $g$  denotes the Landé factor ( $g \approx 2$  for a free electron) which is directly related to

the gyromagnetic ratio by  $g = \gamma\hbar/\mu_B$ .

Using a second, oscillating magnetic field  $B_1$  applied perpendicular to  $B_0$ , one can drive transitions between the two spin states provided that the resonance condition is met, i.e. the frequency  $\nu$  of the oscillating field has to match the energy difference  $E = h\nu = \gamma\hbar B_0$ . These driven transitions are known under the name Electron Spin Resonance (ESR) in the case of electrons, Muon Spin Resonance ( $\mu SR$ ) for muons or Nuclear Magnetic Resonance (NMR) in case of nuclei. The main difference between them is the mass of the corresponding particle leading to very different resonance conditions. While typical frequencies for ESR lie in the GHz regime, they are in the MHz regime for NMR, roughly a factor of thousand smaller. The situation gets slightly more complicated for nucleons compared to isolated electrons due to the fact that more than just two energy states can be involved here. The  $^{69}Ga$ ,  $^{71}Ga$  and  $^{75}As$  isotopes for example have a nuclear spin  $I = \frac{3}{2}$  and the magnetic quantum number may take the values  $m = \pm\frac{1}{2}, \pm\frac{3}{2}$  corresponding to four different energy states with 3 different transitions in between them, without taking two- and three-photon processes into account. However, to leading order the four states are equidistant in energy and therefore often only a single resonance line is observed in the experiment.

How is a NMR signal detected? The strong static field  $B_0$  causes an imbalance in the population of the contributing spins. In the simple case of free electrons, the population  $N_U$  of the more energetic up state is suppressed by the Boltzmann factor compared to the one of the down state  $N_D$

$$\frac{N_U}{N_D} = e^{-\frac{E}{k_B T}} \quad (8)$$

where  $T$  stands for temperature,  $E$  for the energy difference of the two contributing states and  $k_B$  for the Boltzmann constant. It is straight forward to extend this concept to nuclei with larger nuclear spin. Going to low temperatures and large static fields is the key for building up a significant spin polarization, i.e. a population difference. The magnetization of the polarized nuclear spins adds up to the external field  $B_0$ , hence increasing or decreasing its value depending on the sign of the gyromagnetic ratio.

However, when tuning the frequency of the oscillating field to the resonance condition, the spin polarization will be destroyed which manifests itself in a small change of the total magnetic field. In standard NMR, this change in magnetic field is measured with an (additional) pick up coil. Though actual magnetic fields due to the thermal nuclear polarization are quite small, a NMR response is observed in GaAs when measuring the longitudinal resistance  $R_{XX}$  (resistively detected NMR, RDNMR). The reason for that is as follows: Electronic spin  $\mathbf{S}$  and nuclear spin  $\mathbf{I}$  couple through the hyperfine interaction, also known under Fermi contact interaction. The coupling strength is characterized through the hyperfine coupling constant  $A$  and depends on the electronic density at nuclear sites. Due to their s-type character, electrons in the conduction band of GaAs have a significant weight at nuclear sites, leading to a large hyperfine constant in GaAs ( $A \approx 90 \mu\text{eV}$ ) and consequently to a significant hyperfine (contact) interaction. In presence of an external B-field, the total electronic Zeeman energy reads [24]:

$$E = g\mu_B B S_z + A \langle I_z \rangle S_z \quad (9)$$

Here,  $\langle I_z \rangle$  denotes the nuclear spin polarization (in our case thermodynamic polarization) and  $S_z$  is the z-component of the electron spin. First and second part on the right-hand side in eq. 9 are referred to as Zeeman term and Overhauser term. As can be seen from eq. 9, the nuclear polarization  $\langle I_z \rangle$  acts like an effective magnetic field, known as nuclear Overhauser field  $B_N = A \langle I_z \rangle / g\mu_B$ . Though this effective field is much larger than the actual B-field contribution of the (partially) ordered nuclear spins to the external B-field (the maximum Overhauser field for GaAs is 5.3 T [25]), it does not induce orbital effects e.g. it does not cause any Lorentz force or Landau levels. Therefore the Overhauser field does not affect the filling factor. However, the longitudinal resistance  $R_{XX}$  depends on the energy gap in the density of states ( $R_{XX} \sim \exp(-\Delta/2k_B T)$  in the thermally activated regime) which depends on the total electronic Zeeman energy [24].



### 1.4.2 RDNMR setup and assembly

Doing RDNMR at low temperatures  $< 100$  mK is challenging since signal cables for the NMR coil should be broad band to transmit the required RF-frequencies and well thermalized at the same time to prevent heating effects that could raise the sample temperature. As a starting point, we take broad band coax cables (few GHz bandwidth,  $\approx 10$  dB attenuation at 20 GHz) with inner conductor (IC) made from silver-plated Cu-Ni and outer conductor (OC) made from Cu-Ni. Its low thermal conductivity (as low as stainless steel [14]) and good soldering properties make Cu-Ni an ideal material for this purpose. Still, additional heat sinking of the coax cables at several temperature stages of the dilution refrigerator is crucial. For the OC, this is a quite simple task. Since it is on ground potential, it can simply be connected electrically with e.g. the mixing chamber plate. A low electrical resistance then guarantees good thermal contact. For the IC carrying the NMR signal the situation is different. Since electrical insulation from ground is required, the IC has to be cooled through an insulating layer by means of phonons. However, standard coax cables use Teflon as a dielectric, whose thermal conductivity is very poor. We therefore built thermalization stages where we use Stycast 1266 epoxy as a dielectric, which was shown to possess good thermal properties at cryogenic temperatures [26] (at least compared to Teflon). The assembly of such a HF-thermalizer is shown in fig. 8.

We solder standard MCX plugs (rounded with a turning machine) to a 5 cm long copper rod of 1 mm diameter as shown in fig. 8(a). Next, using a Teflon mold, we add a layer of insulating Stycast 1266 epoxy. The radii  $R_{IC}$  and  $R_{OC}$  of inner and outer conductor, together with the dielectric constant  $\epsilon_r$  of the insulator, determine the characteristic impedance  $Z_0$  of the HF-thermalizer [27]:

$$Z_0 = \frac{1}{2\pi} \sqrt{\frac{\mu}{\epsilon}} \ln \left( \frac{R_{OC}}{R_{IC}} \right) \quad (10)$$

The dielectric constant of Stycast 1266 epoxy, measured at 1 KHz, drops by a factor of 0.63 upon cooling from room temperature down to 70 mK [26]. Assuming the

same scaling behavior for higher frequencies, we estimate  $\epsilon_r = 1.89$  at 1 MHz and low temperatures ( $\epsilon_r = 3$  at 1 MHz and room temperature [26]). Assuming  $\mu_r = 1$ , we calculate an outer conductor diameter  $R_{OC}$  of 3.2 mm ( $R_{IC} = 1$  mm) for a desired characteristic impedance  $Z_0$  of  $50\Omega$ . Reflection measurements using a vector network analyzer show transmission characteristics that are close to  $50\Omega$  with a reflection parameter  $S_{11}$  smaller than  $-15$  dB (measured at 4.2 K) up to one 1 GHz.

After adding the 1.1 mm thick ( $R_{OC} - R_{IC}$ ) insulation layer, in a final fabrication step, the body of the HF-thermalizer is glued into a copper housing with Ag-epoxy, see fig. 8(c). Three HF-thermalizers were mounted at different temperature stages of the DR, one at the MC-plate, one at the 50 mK-plate and a last HF-thermalizer is mounted at the 1 K-plate.

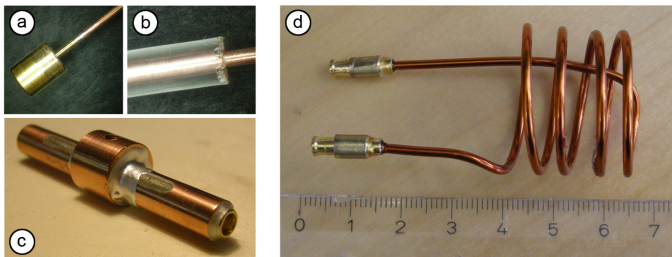


Figure 8: (a)-(c) shows the assembly of an impedance matched high frequency (HF) thermalizing stage. (a) Rounded MCX connector, soldered to a 1 mm diameter copper rod. (b) Prefabricated Epoxy rod (dielectric) with inserted copper rod (c) Fully assembled stage, with the center body of (a), (b) glued into a copper housing using Ag-Epoxy. (d) NMR coil made from an insulated, 1.4 mm diameter copper rod.

Besides the broad band signal cables, NMR obviously requires a coil with sufficiently large bandwidth to generate the required oscillating magnetic field. Good results are obtained with free-standing few-turn coils made from thick copper wire, see fig. 8(d). We use an 1.4 mm thick, insulated copper rod (rigid copper wire) that we shape in the geometry of a coil by bending it around a wooden slat. The RF-setup consisting of coax cables, HF-thermalizers and NMR coil, shows a broad bandwidth of almost 1 GHz. We

note that non-resonant heating through the NMR setup is small. Thermometry using the 5/3 fractional quantum hall state in presence of RF-irradiation strong enough to see NMR, yields an upper limit on the electron temperature of 27.5 mK.

### 1.4.3 RDNMR in the (fractional) quantum hall regime

Before trying to find a NMR response from the CEO wires, we perform a few standard RDNMR experiments to test the NMR coil and get familiar with RDNMR measurements in general. With GaAs heterostructures RDNMR has been demonstrated in the quantum hall regime for a variety of integer and fractional filling factors  $\nu$  [24, 28–32]. Here, we will follow the measurements from Desrat *et al.* in [24] and reproduce some of their results (see fig. 9). As discussed earlier, the longitudinal resistance  $R_{XX}$  depends on the gap of the corresponding state to which the total electronic Zeeman energy contributes (i.e. the sum of Zeeman and Overhauser term). Changes in the total electronic Zeeman energy, e.g. when destroying the nuclear polarization with resonant RF-irradiation, manifest themselves as a change in  $R_{XX}$ . We use this fact and measure  $R_{XX}$  (see fig. 25) as a function of perpendicular magnetic field  $B_z$  and RF-frequency  $f_{NMR}$ . The results are shown below in fig. 9(a). The output power for the RF-frequency is set to -30 dBm ( $1 \mu W$ ). The optimal output power depends on details of the setup and has to be established experimentally, e.g. by optimizing the signal size. The bright (asymmetric) spot in fig. 9(a), moving linear in frequency as a function of  $B_z$ , is identified as  $^{75}As$  resonance. The asymmetry becomes more evident in single line scans as shown in fig. 9(b).

When crossing the resonance frequency from left to right (smaller to larger frequencies),  $R_{XX}$  first stays constant then abruptly changes and finally exponentially relaxes back. The opposite is observed when reversing the sweep direction. The reason for this is quite simple. The nuclear spin system stays undisturbed until the resonance frequency is hit and the nuclear polarization is destroyed immediately. However, a finite time, in the order of seconds for the present system, is needed to repolarize the nuclear spins. This asymmetry is therefore observed in fast frequency scans compared to the time scale

of the repolarization time. Lowering the frequency sweep rate from 0.26 MHz/min, as used for the measurements in fig. 9(c), to 3.5 kHz/min, reveals the quadrupolar splitting of  $^{75}\text{As}$ .

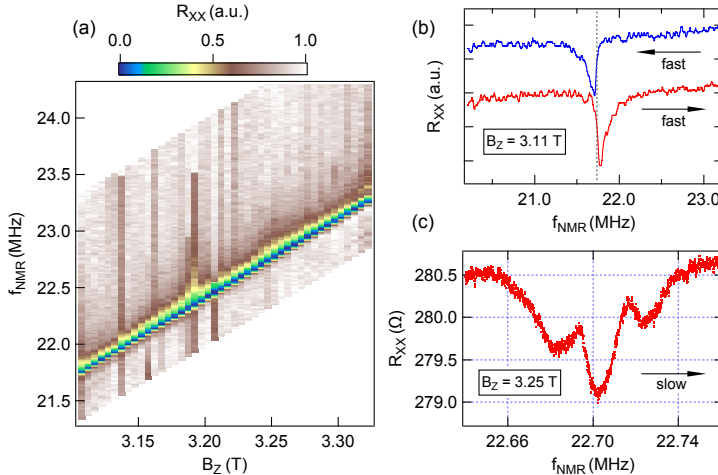


Figure 9: (a) Longitudinal resistance  $R_{XX}$  (in arbitrary units) as a function of perpendicular magnetic field  $B_z$  and RF-frequency  $f_{NMR}$  in the vicinity of the  $^{75}\text{As}$  resonance. Each line scan is renormalized to emphasize the small NMR signal on a largely varying background (b) Fast frequency scans (0.26 MHz/min) with scan direction indicated by black arrows. A black dashed line marks the position of the resonance frequency. (c)  $^{75}\text{As}$  quadrupolar splitting, revealed in a slow (3.5 kHz/min) frequency scan.

The standard RDNMR data presented in fig. 9 agrees well with findings from previous measurements such as [24], which makes us confident that the RDNMR setup works properly.

#### 1.4.4 Identification of different isotopes

The question naturally arises whether or not other resonances besides  $^{75}\text{As}$  can be detected. In order to answer that question, we scan the RF-frequency across a very large window ( $1 \text{ MHz} < f_{NMR} < 100 \text{ MHz}$ ). Fig. 10(a) shows  $\Delta R_{XX}$  ( $R_{XX}$  with a smooth background subtracted) at a fixed magnetic field of  $B_z = 3.75$  T.

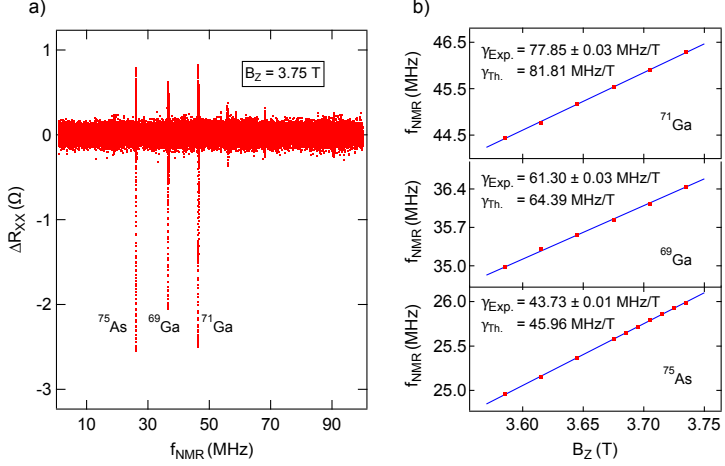


Figure 10: (a) Longitudinal resistance  $\Delta R_{XX}$  in a high resolution frequency scan (1 MHz – 100 MHz) for a fixed magnetic field of  $B_z = 3.75$  T. A smooth background has been subtracted from the data to emphasize the NMR resonances, attributed to  $^{69}\text{Ga}$ ,  $^{71}\text{Ga}$  and  $^{75}\text{As}$  isotopes and labeled accordingly. (b) B-field evolution for the three resonances in (a). The blue traces are linear fits to the measured data (red points). Extracted gyromagnetic ratios ( $\gamma = 2\pi \cdot f_{\text{NMR}}$ ) are indicated in the respective panels together with literature values from [33].

The three clear RDNMR signals observed in fig. 10(a) are assigned to  $^{75}\text{As}$ ,  $^{69}\text{Ga}$  and  $^{71}\text{Ga}$  resonance lines. To confirm that hypothesis, we check that all peaks move linear in  $f_{\text{NMR}}$  as a function of  $B_z$  (fig. 10(b)). Furthermore, from the linear fit in fig. 10(b) we extract the gyromagnetic ratio and see that it is only slightly above the literature value for all three resonances. One could think of several reasons for the systematic deviation (experimental values are  $\approx 5\%$  smaller than literature values). It could be that the magnet does not completely reach its setpoint or simply that the calibration for the field constant is slightly off. Also, a slight misalignment of the sample away from the center of the field would lead to an overestimation of the B-field and consequently to an underestimation of the gyromagnetic ratio (equivalent to a slight overestimation of the field constant). Besides the three prominent resonances, other signals with smaller amplitudes are observed. The resonant feature around 56 MHz was reproducible, it was

not tested though whether or not the resonance moves linearly in frequency as a function of  $B_z$  (NMR resonance frequencies in that regime are only expected for  $^{115}\text{Sn}$  and  $^{119}\text{Sn}$  out of all elements listed in [33]).

In summary, these proof-of-principle experiments demonstrate a fully operational RDNMR setup. In the outlook at the end of the thesis we present some preliminary measurement results for a CEO wire under RF irradiation.

## 2 Silver Epoxy Microwave Filters for Thermalization below 10 mK

C. P. Scheller, S. Heizmann, D. Giss, D. M. Zumbühl

*University of Basel, Klingelbergstrasse 82, CH-4056 Basel, Switzerland*

K. Bedner

*Paul Scherrer Institut, CH-5232 Villigen PSI, Switzerland*

M. Meschke

*Low Temperature Lab., Aalto University, School of Science, 00076 Aalto, Finland*

J. D. Zimmerman, A. C. Gossard

*Materials Department, University of California, Santa Barbara, California 93106*

### Abstract

We present cryogenic filters with very low cut-off frequency and good attenuation that allow for thermal heat sinking in a dilution refrigerator. They consist of several meters of thin copper wire with minimized parasitic capacitive coupling between windings, casted into conductive silver epoxy. The measured attenuation reaches 100 dB or more above  $\approx 150$  MHz and - when capacitors are added - already above  $\approx 30$  MHz. Combined with  $\approx 1.5$  m of thermocoax, we measure electron temperatures as low as  $18 \pm 3$  mK using a GaAs surface gated quantum dot in deep Coulomb Blockade as an electron thermometer. Between  $\approx 40$  mK and 0.6 K, the quantum dot electron temperature agrees very well with RuO<sub>2</sub> and CMN thermometers on the mixing chamber. Using an improved setup with thermalized sample holder, chip carrier and additional filtering stage, we demonstrate electron temperatures as low as 7.5 mK in metallic coulomb blockade thermometers.

This chapter is in preparation for publication

## 2.1 Motivation and main experimental results

Advancing to lower system temperatures is of fundamental interest, as it allows to resolve smaller energy scales and hence to visualize effects that were previously smeared out by temperature broadening. Examples of quantum mechanical effects with small energy scales include fractional quantum hall states[34–39], phase transitions[1, 40–42] and many more. Though  $^3\text{He}/^4\text{He}$ -dilution refrigerators with base temperatures as low as 5 mK are readily available, typical electron temperatures  $T_e$  in semiconductor nanoscale devices are considerably higher due to insufficient thermalization, filtering of high frequency radiation and low frequency noise from the measurement setup, e.g. ground loops. Part of the microwave radiation stems from the room temperature measurement setup, connected to the sample via the leads, but also from higher temperature stages (1 K-4.2 K) of the refrigerator[43–45]. Various types of cryogenic microwave filters (CMFs) have been developed in the past to suppress this radiation such as metal powder filters[46–49], micro fabricated filters[50–53], thermocoax cables[54, 55], copper tapeworm filters[56, 57], thin film filters[58] and lossy transmission lines[59]. An overview on CMFs is given in ref.[60].

While achieving low electron temperatures relies on efficient filtering strategies, reduction of heat leaks and proper heat sinks for sample holder, backplane, current leads etc. are equally important ingredients. We note that electron-phonon coupling, scaling as  $T^5$ , is highly suppressed at low temperatures which makes further cooling very challenging. However, additional cooling through the current leads introduces a much weaker  $T^2$  scaling (electron-electron coupling) which eventually becomes the dominant mechanism[39].

In this Letter we present miniature CMFs that unit excellent RF-filtering properties and efficient thermalization, suitable for e.g. low temperature quantum transport measurements. The filters are modular, robust against thermal cycling, and possess a predictable attenuation spectrum. Their performance is tested in thermometry experiments using a GaAs quantum dot and metallic coulomb blockade thermometers (CBTs).



In the latter case,  $T_e$  down to 7.5 mK are demonstrated.

## 2.2 Cryogenic microwave filters

The CMFs (inset of fig.11), mounted at the mixing chamber (MC) plate of a dilution refrigerator with  $T_{MC} = 5$  mK at base temperature, are connected to the room temperature measurement setup through 1.5 m long thermocoax cables - very efficient microwave filters in the few GHz regime (green trace in fig.11). The coaxes are heat sunk at 4.2 K, the 1 K pot, at the 50 mK plate and the MC-plate.

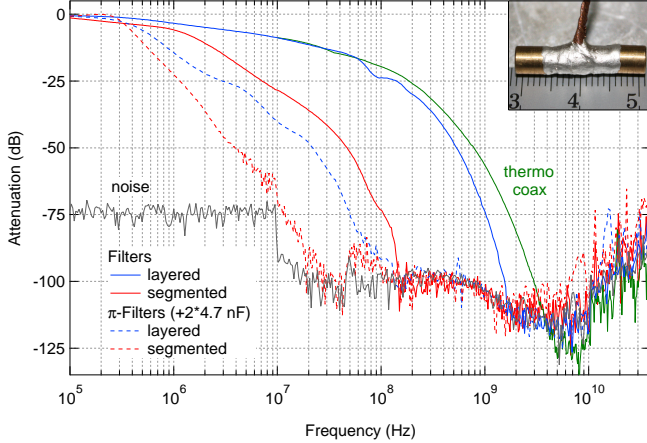


Figure 11: Room temperature attenuation characteristics of a thermocoax cable (green) and different CMFs. Blue and red represent layered and segmented filters respectively. For the dashed characteristics, a 4.7 nF capacitor was added to both filter ends. A picture of a CMF and centimeter scalebar is shown in the inset.

### 2.2.1 Filter thermalization and attenuation

The CMFs consist of insulated copper wire, casted into conductive Ag-epoxy[61] to facilitate cooling. Note that the Ag-epoxy stays conductive down to the lowest  $T_{MC}$ . A thick copper braid, also embedded into the epoxy layer and attached to the mixing chamber plate on its other end, ensures a well thermalized outer conductor which in

return cools the inner conductor through the Cu-wire's  $d_{\text{Ins.}} = 8 \mu\text{m}$  thick polyurethane insulation.

The attenuation profile can be described as a lossy transmission line with frequency dependent (skin effect) resistance per length  $R_{\text{IC}}$  and  $R_{\text{OC}}$  of inner and outer conductor, respectively. While DC-currents are supported by the whole cross section  $A = \pi D^2/4$  of the Cu-wire with inner conductor diameter  $D$ , the skin effect forces AC-currents with frequency  $\nu$  to an annulus of width  $\delta = 1/\sqrt{\sigma_{\text{Cu}}\mu_{\text{Cu}}\nu\pi}$  (skin depth). Here,  $\sigma_{\text{Cu}}$  denotes the conductivity of the Cu-wire and  $\mu_{\text{Cu}}$  its magnetic permeability. The effective cross section therefore reduces to  $A = D\pi\delta$  and consequently  $R_{\text{IC}}$  increases as a function of  $\nu$ . Equivalent arguments hold for the outer conductor. Note that due to its smaller conductivity  $\sigma_{\text{epoxy}} \ll \sigma_{\text{Cu}}$ , the Ag-epoxy outer conductor is dominating the total resistance  $R_{\text{tot}}(\nu) = R_{\text{IC}}(\nu) + R_{\text{OC}}(\nu)$  at high  $\nu \gtrsim 2 \text{ MHz}$ . The resulting attenuation is  $\propto -\nu^{3/4}$  for low frequencies  $2\pi\nu L \ll R_{\text{tot}}(\nu)$  and  $\propto -\nu^{1/2}$  for high frequencies in the GHz regime with a smooth transition in between. Here,  $L = \mu_0/2\pi \cdot \ln((D + 2d_{\text{Ins.}})/D)$  denotes the inductance per length (see supplementary material for details on the theory and comparison with experimental data).

## 2.2.2 Filter fabrication and characterization

2.5 m of Cu-wire ( $D = 0.1 \text{ mm}$ ) are wound around a prefabricated 2.5 mm thick Ag-epoxy rod to form a 5-layer coil of 8 mm length. During the winding process we continuously wet epoxy rod and coil with Ag-epoxy to ensure good electrical and thermal contact throughout the device. Standard MCX connectors are soldered and, after gluing parts together with Stycast 2850 epoxy, a Cu-braid is attached that serves as a thermal anchor. The resulting layered CMFs are 22 mm long, 5 mm in diameter with a room temperature DC resistance of  $\approx 5 \Omega$  (below  $50 \text{ m}\Omega$  at 4.2 K), a capacitance of  $\approx 4 \text{ nF}$ , and more than 100 dB attenuation above 1.5 GHz (solid blue trace in fig.11).

Parasitic capacitive couplings drastically degrade the transmission characteristics of layered filters. However, a different filter design (segmented CMF), where the single continuous coil is split up into several coils in series, allows for significant reduction of

capacitive couplings. For layered filters the first and the last layer of the coil, corresponding to start (first 20%) and end (last 20%) of the current path through the CMF or vice versa, are separated only by 3 layers of Cu-wire or equivalently 0.3 mm distance. In contrast, the first and the last 20% of the current path are separated by  $\approx 5$  mm for the segmented filters (dashed blue trace in fig.11). In a naive plate capacitor model this enhancement of separation corresponds to a reduction of capacitive couplings by a factor of 10-20. Indeed, we obtain 100 dB at 1.5 GHz for the layered CMFs while a similar attenuation is already reached at 150 MHz for segmented filters.

The CMFs may be extended to  $\pi$ -filters through addition of capacitors to both filter ends. Here, 4.7 nF discoidal ceramic capacitors with negligible temperature dependence were used, available from PA&E [62]. Layered and segmented  $\pi$ -filters are shown as solid and dashed red curves in fig. 11. The addition of capacitors further reduces the cut off frequency such that 100 dB attenuation are obtained at 30 MHz for segmented  $\pi$ -filters. However, in order not to reduce the bandwidth for future experiments by adding capacitive parts and because of noise reasons (IV-Converter), the low capacitance segmented CMFs were chosen for the following measurements.

We note that replacing the material of the central rod with a mixture of Stycast 2850 and Fe powder as in ref.[47] or replacing the copper wire with resistive wire, did not improve the filter performance.

All spectra were recorded with an Agilent Network Analyzer and a Signal Analyzer for the low frequency range. Changing between instruments is also responsible for the jump in the noise floor at 10 MHz in fig.11. Going to cryogenic temperatures does not significantly alter the CMF transmission profile (not shown). Ultimately, the objective of the CMFs is to reach lower electron temperatures  $T_e$  in real devices, which is the focus of the following section.

## 2.3 Electron temperature measurements

### 2.3.1 Quantum dot thermometer

We use a surface gated GaAs/AlGaAs quantum dot (QD) in deep coulomb blockade, probing the Fermi Dirac distribution in the reservoirs, as an electron thermometer [63–67]. A SEM image of a similar device is shown in the lower inset of fig.12.

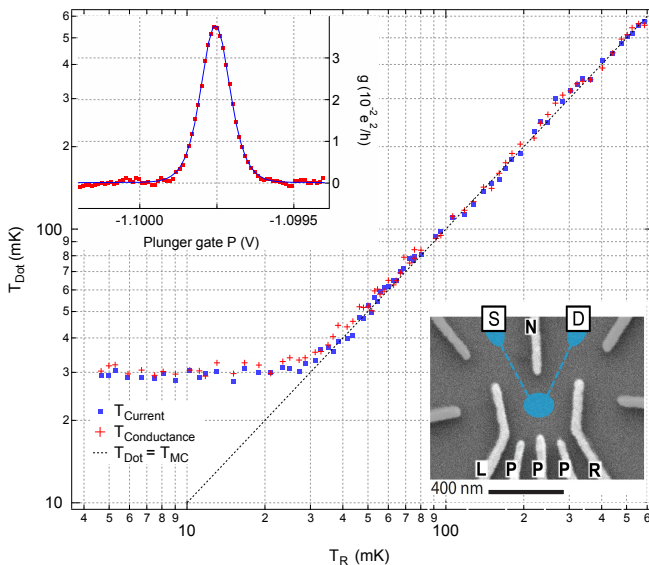


Figure 12: Electron temperature extracted from current and conductance measurements versus refrigerator temperature  $T_{MC}$ . The case of perfect thermalization  $T_e = T_{MC}$  is also indicated. The upper inset shows a typical base temperature conductance trace and fit. A SEM image of similar device is shown in the lower inset. Gates N,L,R and P (light grey) form the QD, while gates in dark grey are left grounded.

Surface depletion gates N,L,R and P isolate the QD from the surrounding two dimensional electron gas (2DEG), while source (S) and drain (D) ohmic contacts serve for current injection and detection. Details on sample fabrication are given in Ref. [68].

The QD differential conductance  $g$  peaks whenever one of its energy levels is aligned with the chemical potential of source and drain (upper inset of fig.12). The conversion

between measured peak width  $\Delta V_G$  and energy  $\Delta E$  is done by means of the lever arm  $\alpha$ ,  $\Delta E = \alpha \cdot \Delta V_G$ . In order to determine  $\alpha$ , a known DC-bias  $V_{SD}$  is applied to the source. As a consequence, the zero bias differential conductance peak splits up into two peaks corresponding to resonant tunneling between quantum dot and either source or drain.  $\alpha$  is then simply given by the separation  $V_{sep}$  of these peaks divided by the applied bias,  $\alpha = V_{sep}/(eV_{SD})$ . In the limit of small tunnel rates to source and drain (and large QD level spacing) compared to temperature, the width  $\Delta V_G$  of these conductance peaks provides a primary electron thermometer[19]. Extracted electron temperatures  $T_{COND}$  are shown in fig.12. All conductance data is recorded with standard Lock in technique using an experimentally chosen AC-excitation to avoid heating ( $2\mu V$  at base temperature).

Instead of measuring  $g$ , we can also monitor the DC current, which shows a finite value whenever a QD level lies between the chemical potentials of source and drain. Measuring the resulting temperature broadened current step as shown in fig.13, allows one to individually map the Fermi Dirac distribution for source and drain and therefore to extract their temperature separately. Here,  $\alpha$  is simply given by the ratio of the applied bias  $V_{SD}$ , divided by the separation of the inflection points for the two Fermi Dirac distributions (for an overview on electron transport in quantum dots, see e.g. ref.[19, 69, 70]). We stress that the DC current, determined by the tunneling rates to source and drain, does not depend on the applied DC voltage as long as excited states (and cotunneling) do not contribute to the transport. Since no systematic deviation is observed between source and drain temperatures, we conclude that energetic electrons from the source with  $100\mu eV$  or more get efficiently thermalized at the drain (reducing the DC bias did not affect  $T_e$ ).

### 2.3.2 Electron temperature with CMFs

Fig. 12 compares extracted electron temperatures from the same warump using both, AC and DC method. We repeatedly measure first the differential conductance as a function of gate voltage  $V_P$  with a finite AC excitation  $V_{AC}$  and zero DC bias  $V_{SD} = 0$ .

Then we measure the DC current step at finite  $V_{SD}$  and repeat the cycle. When fitting the measured current step, source and drain temperatures are forced to be identical in order to obtain more reliable fitting results i.e.  $T_S = T_D =: T_{CURR}$ . From the fit, we get  $T_{CURR}$  and the lever arm  $\alpha$ , which is also used to calibrate the conductance measurements. We note that for the differential conductance measurements, already a small DC offsets results in a broader conductance peak, leading to an overestimation of  $T_{COND}$ . Therefore, a feedback mechanism was implemented that compensates the DC offset by minimizing the DC current in the  $V_{SD} = 0$  conductance measurements, therefore ensuring excellent alignment of source and drain during the more than 40 hours lasting measurement in fig.12.

Over the whole temperature range these two methods of measuring the  $T_e$  agree well with each other and, above 40 mK, also with  $T_{MC}$ , measured with a  $RuO_2$  thermometer. The  $RuO_2$  thermometer, precalibrated with a fixed point device, agrees very well with a CMN thermometer which uses the mutual inductance of the paramagnetic cerium magnesium nitrate salt as a measure of temperature (not shown). Below 40 mK,  $T_e$  starts deviating from  $T_{MC}$  and saturates at 30 mK, defining an upper bound on the electron temperature.

The temperature saturation of the electronic system is due to noise in the measurement setup and insufficient thermalization (e.g. ground plane of the chip carrier is not heat sunk). We therefore switch to a simpler, pure DC setup which facilitates noise reduction. As a consequence,  $T_e$  is reduced down to  $18 \pm 3$  mK, averaged several traces. An example of such a trace including curve fits and individually extracted source/drain temperatures, is presented in the upper panel of fig.13.

The inset shows a zoom in on the drain lead in logarithmic scale, where the linear current increase clearly indicates the temperature broadened regime.

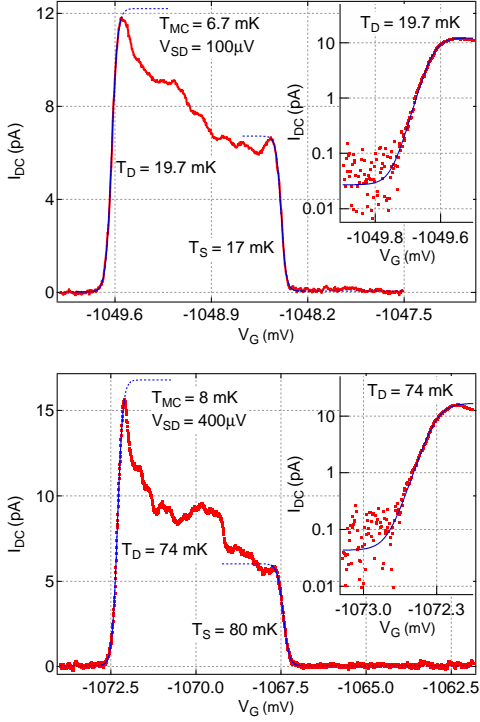


Figure 13: DC current through the quantum dot with individual Fermi Dirac fits for source and drain leads taken at base temperature. The inset shows the same data and fits in log-scale for the drain side. Upper and lower panel correspond to measurements with and without CMFs. For the traces shown, we extract electron temperatures of  $T_S = 17$  mK ( $T_D = 19.7$  mK) and  $T_S = 80$  mK ( $T_D = 74$  mK) without CMFs.

### 2.3.3 Electron temperature without CMFs

The CMFs are now replaced with simple adapters and the same DC current temperature measurement is repeated. As shown in the lower panel of fig.13, without CMFs the electron temperature drastically increases to  $T_e \approx 75$  mK, demonstrating the filters efficiency. Note that due to the elevated electron temperature, more DC bias is applied to clearly separate the source and drain current steps. However, the larger DC bias of

$400\ \mu\text{V}$ , compared to  $100\ \mu\text{V}$  does not increase the system temperature, as discussed earlier (smaller bias was tested). All QD temperature measurements were performed in the single electron regime.

### 2.3.4 Metallic coulomb blockade thermometer

Despite the success of the CMFs, there is still room for improvement considering that the mixing chamber reaches  $5\ \text{mK}$ . Therefore, another filtering/thermalization stage is placed directly inside the Faraday cup i.e. inside the shielded sample can. Furthermore, a heat sunk sample holder made from conductive Ag-epoxy is used and the ceramic chip carrier (known to possess heat release) is replaced with a standard plastic dip socket equipped with a  $1\ \text{mm}$  thick gold plated and heat sunk copper backplane. We proceed to measure electron temperatures with the two stage filtering/thermalization setup. For simplicity, metallic coulomb blockade thermometers (CBTs) are used that do not require gate tuning in contrast to QDs.

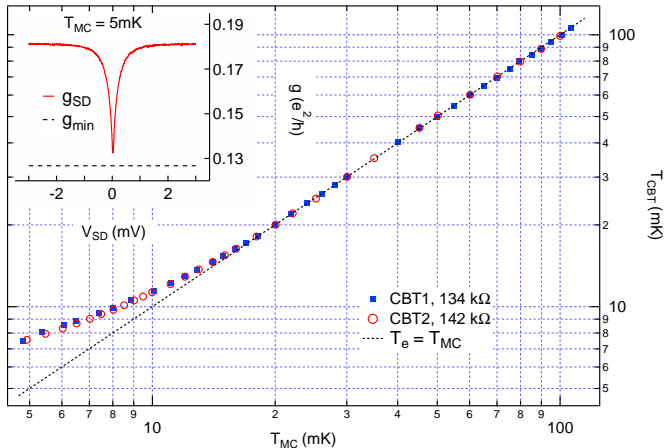


Figure 14: Electron temperature  $T_e$  versus mixing chamber temperature  $T_{\text{MC}}$  for two metallic coulomb blockade thermometers on the same wafer. The case of ideal thermalization,  $T_e = T_{\text{MC}}$ , is also indicated. The inset shows the  $V_{\text{SD}}$  bias conductance dip at base temperature (red). The minimum conductance  $g_{\text{min}}$ , measured while resting at  $V_{\text{SD}} = 0$ , is indicated as dashed line.



The CBTs consist of 7 parallel arrays with 64 angle evaporated tunnel junctions between metal islands [71, 72]. They operate in the regime where the charging energy  $E_C$  is comparable to temperature [73], in contrast to the quantum dot measurements in figures 12, 13. The full width at half maximum of the bias voltage dependent conductance dip can serve as a primary thermometer [74, 75]. Here, however, we use the conductance dip  $\Delta g/g$  as a secondary thermometer to avoid heating at finite bias. At high temperatures where the CBTs are in thermal equilibrium with the mixing chamber,  $E_C$  can be extracted from the temperature dependent  $\Delta g/g$  using the relation [73]  $\Delta g/g = u/6 - u^2/60 + u^3/630$ , where  $u = E_C/k_B T_e$ . With the known  $E_C$ , the measured  $\Delta g/g$  can then be converted to the corresponding electron temperature  $T_e$  in the full temperature range. Two CBTs (on the same wafer) with resistances around 140 k $\Omega$  were measured using standard Lock in technique with an AC excitation of 4  $\mu$ V, experimentally chosen to avoid heating effects. Extracted electron temperatures from both devices agree very well with each other and start deviating from  $T_{MC}$  below 15 mK (see fig.14), reaching a minimum  $T_e$  of 7.5 mK (corresponds to a residual heat leak of 13 aW per junction, if electron-phonon coupling is assumed to be dominant).

At the lowest temperatures, long times constants in order of minutes are observed. The conductance  $g(V_{SD} = 0)$  drops as a function of time and saturates at a value  $g_{\min}$ , clearly lower than the minimum conductance in  $V_{SD}$  scans, see fig. 14. We therefore use  $g_{\min}$  in order to compute the relative conductance dip  $\Delta g/g$  and consequently the electron temperature  $T_e$ . We note that fitting the data in fig. 14 with a power law  $T_e = (T_S^p + T_{MC}^p)^{1/p}$ , where  $T_S = 6.9 \pm 0.1$  is the CBT saturation temperature, gives  $p = 2.7 \pm 0.2$ , clearly lower than  $p = 5$  (electron-phonon coupling) [4]. This might indicate additional cooling through the current leads.

## 2.4 Summary

In conclusion, we presented CMFs with significantly reduced cut-off frequency due to a reduction of parasitic capacitive couplings. Their attenuation reaches 100 dB at 150 MHz or, when capacitors are added, already at 30 MHz. In addition, the CMFs

are optimized for thermalization of the filtered current leads. One stage of CMFs allowed to reduce the electron temperature, measured with a GaAs quantum dot, from  $\approx 75$  mK down to  $\approx 18$  mK. With an improved setup (filtering, thermalization), electron temperatures as low as 7.5 mK are demonstrated in CBTs, clearly supporting the present cooling strategy. It remains to be checked experimentally to what temperature a quantum dot (2DEG) would cool in latter configuration.

### **Acknowledgments**

This work was supported by the Swiss Nanoscience Institute(SNI),NCCR QSIT, Swiss NSF, ERC starting grant, and EU-FP7SOLID and MICROKELVIN.

We acknowledge J. P. Pekola for his support and thank M. Steinacher, A. de Waard and G. Frossati for valuable inputs on the CMF design.

## 2.5 Supplemetal Materials

The attenuation of a coaxial cable can be calculated by means of transmission line theory[27], which extends the description of discrete electronic components to distributed elements. For a coaxial cable with resistance  $R_{\text{tot}}$  [ $\Omega/\text{m}$ ], given by the sum of inner and outer conductor resistance  $R_{\text{IC}}$  and  $R_{\text{OC}}$ , with inductance  $L$  [ $\text{H}/\text{m}$ ], capacitance  $C$  [ $\text{F}/\text{m}$ ] and shunt conductance  $G$  [ $\text{S}/\text{m}$ ] (note that all parameters are per length), the attenuation in units of decibel as a function of frequency  $\nu$  reads:

$$\text{Attenuation}(\nu) = 20 \log \left| e^{-\gamma z} \right|, \quad \gamma = \sqrt{(R_{\text{tot}} + 2\pi i \nu L)(G + 2\pi i \nu C)} \quad (11)$$

Here,  $z$  denotes the wire length in units of m. Parameters  $R_{\text{tot}}$ ,  $L$ ,  $C$  and  $G$  may be calculated from geometric dimensions of the coaxial cable (inner conductor diameter  $D$ , thickness  $d_{\text{Ins.}}$  of the polyurethane insulation and  $d_{\text{epoxy}}$  for the epoxy outer conductor), and material properties such as the dielectric constant  $\epsilon_{\text{Ins.}}$  of the polyurethane insulation and the conductivity  $\sigma_{\text{Cu}}$ ,  $\sigma_{\text{epoxy}}$ ,  $\sigma_{\text{Ins.}}$  of inner conductor, outer conductor and the insulator, respectively:

$$\begin{aligned} R_{\text{tot}} &= \frac{1}{\sigma_{\text{Cu}} \left(\frac{D}{2}\right)^2 \pi} + \frac{1}{\sigma_{\text{epoxy}} \left( \left(\frac{D}{2} + d_{\text{Ins.}} + d_{\text{epoxy}}\right)^2 - \left(\frac{D}{2} + d_{\text{Ins.}}\right)^2 \right) \pi} \\ C &= \frac{2\pi\epsilon_0\epsilon_{\text{Ins.}}}{\ln\left(\frac{D/2 + d_{\text{Ins.}}}{D/2}\right)} \\ L &= \frac{\mu_{\text{Ins.}}}{2\pi} \ln\left(\frac{D/2 + d_{\text{Ins.}}}{D/2}\right) \\ G &= \frac{\sigma_{\text{Ins.}}}{\epsilon_{\text{Ins.}}} C \end{aligned} \quad (12)$$

As discussed in the main text, the skin effect forces AC currents to the conductor surface i.e. the skin depth  $\delta_{\text{Cu}} = 1/\sqrt{\sigma_{\text{Cu}}\mu_{\text{Cu}}\nu\pi}$  in case of copper and  $\delta_{\text{epoxy}} = 1/\sqrt{\sigma_{\text{epoxy}}\mu_{\text{epoxy}}\nu\pi}$  for the epoxy outer conductor (the permeabilities  $\mu_{\text{Cu}}$ ,  $\mu_{\text{epoxy}}$  and  $\mu_{\text{Ins.}}$  are assumed to be equal to the vacuum permeability  $\mu_0$ , since all those materials, copper and Ag-epoxy and polyurethane, are not magnetic). As a consequence, the

resistance is modified to:

$$R_{IC} = \frac{1}{\sigma_{Cu} \left( \left( \frac{D}{2} \right)^2 - \left( \frac{D}{2} - \delta_1 \right)^2 \right)}, \quad \delta_1 = \min(\delta_{Cu}, D/2)$$

$$R_{OC} = \frac{1}{\sigma_{epoxy} \left( \left( \frac{D}{2} + d_{Ins.} + \delta_2 \right)^2 - \left( \frac{D}{2} + d_{Ins.} \right)^2 \right)}, \quad \delta_2 = \min(\delta_{epoxy}, d_{epoxy})$$
(13)

Note that eq.13 gives an approxiated solution for  $R_{IC}(\nu)$  that is, however, very close to the exact solution which can be expressed in terms of bessel functions.

Next, experimental results are compared with attenuation curves obtained from transmission line theory, i.e. using eq.11 ( $C$ ,  $L$  and  $G$  are calculated from eq.12 and the frequency dependent resistance is given in eq.13). Fig.15 shows the measured attenuation profile for a microwave filter with  $z = 1.51$  m of copper wire, a total DC resistance and capacitance of  $R_0 = 3.36 \Omega$  and  $C = 2.54$  nF, respectively. In contrast to the filters in the main text, here the wire is wound as a 6 cm long and thin single layer coil to suppress parasitic capacitive couplings (due to the single layer design interlayer couplings are absent).

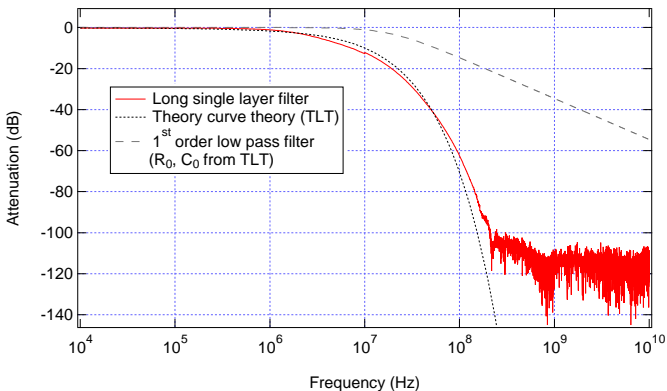


Figure 15: Measured room temperature attenuation characteristics for a single layer microwave filter (no interlayer coupling) with  $z = 1.51$  m of copper wire (red data). A theory curve using eq.11 and the parameters from Tab.1, is shown as dotted, black curve. In dashed grey, a standard first order low-pass filter ( $R_0 = R_{tot}z$  and  $C_0 = Cz$  from theory curve) is shown for comparison.

The measured attenuation is in very good agreement with theoretical predictions for a 1.51 m long coax cable (black dashed line in Fig. 15) with inner and outer conductor made from copper and silver epoxy, respectively. We stress that the input parameters for the theory curve, given in Tab. 1, arise from independently measured quantities and literature values that completely fix the attenuation profile without adjustable parameters. While the conductivity of copper  $\sigma_{\text{Cu}}$ , the thickness  $d_{\text{epoxy}}$  of the epoxy layer have a minor influence on the transmission profile (given the low conductivity  $\sigma_{\text{Ins.}}$  of polyurethane, the shunt term is negligible), the other quantities affect it quite strongly.

We note that since  $R_{\text{tot}}$  is dominated by the outer conductor at high frequencies, a replacement of the inner conductor with e.g. resistive wire, does not improve the filter performance, provided that the resistivity of the inner conductor stays well below that of silver epoxy. For the same reason, the transmission does not significantly alter at cryogenic temperatures, though the conductivity of the copper wire significantly increases (a residual resistance ratio of  $RRR = 128$  was measured for the present wire, whereas  $RRR \sim 3$  for the silver epoxy).

$D$	$97 \pm 2 \mu\text{m}$	measured ( $D = 100 \mu\text{m}$ , manufacturer[76])
$d_{\text{Ins.}}$	$8 \pm 2 \mu\text{m}$	measured
$d_{\text{epoxy}}$	$\approx 2 \text{ mm}$	cross section of the filter
$z$	1.51 m	measured
$\epsilon_{\text{Ins.}}$	$4.6 \pm 1$	chosen to match the measured capacitance
$\sigma_{\text{Ins.}}$	$< 9.3 \cdot 10^{-14} \text{ S/m}$	measured
$\sigma_{\text{Cu}}$	$5.95 \cdot 10^7 \text{ S/m}$	Ref. [77]
$\sigma_{\text{epoxy}}$	$\geq 2 \cdot 10^5 \text{ S/m}$	Ref. [61]

Table 1: Material parameters and geometrical dimensions used for the theory curve shown in Fig. 15.

From eq. 12 the filter DC resistance  $R_0 = (R_{\text{IC}}(\nu = 0) + R_{\text{OC}}(\nu = 0)) \cdot z \approx R_{\text{IC}}(\nu = 0) \cdot z$  can easily be calculated,  $R_0 = 3.43 \pm 0.15 \Omega$ , in good agreement with the measured resistance of 3.36  $\Omega$ .

To emphasize the filter performance, the theoretical attenuation profile for a standart first order low-pass filter with  $R_0 = 3.36 \Omega$  and  $C_0 = 2.54 \text{ nF}$  is shown in fig. 15 (dashed grey) in addition to the data and transmission line model.



### 3 Metallic Coulomb Blockade Thermometry down to 10 mK and below

L. Casparis, D. Maradan, A. C. Clark, C. P. Scheller,  
K. K. Schwarzwalder, D. M. Zumbuhl

*Department of Physics, University of Basel, CH-4056 Basel, Switzerland*

M. Meschke, J. P. Pekola

*Low Temperature Laboratory (OVLL), Aalto University, 00076 Aalto, Finland*

#### Abstract

We present an improved nuclear refrigerator reaching 0.3 mK, aimed at microkelvin nanoelectronic experiments, and use it to investigate metallic Coulomb blockade thermometers (CBTs) with various resistances  $R$ . The high- $R$  devices cool to slightly lower  $T$ , consistent with better isolation from the noise environment, and exhibit electron-phonon cooling  $\propto T^5$  and a residual heat-leak of 40 aW. In contrast, the low- $R$  CBTs display cooling with a clearly weaker  $T$ -dependence, deviating from the electron-phonon mechanism. The CBTs agree excellently with the refrigerator temperature above 20 mK and reach a minimum- $T$  of  $7.5 \pm 0.2$  mK.

This chapter was published in *Rev. Sci. Instrum.* **83**, 083903 (2012).

## 3.1 Motivation

Advancing to even lower temperatures can open the door for the discovery of new physics: for example, submillikelvin temperatures in quantum transport experiments could lead to novel nuclear-spin physics [41, 42] in nanoscale semiconductor devices [78] or could facilitate the study of non-Abelian anyons, Majorana fermions and topological quantum computation in fractional quantum Hall samples [79, 80]. However, cooling of nanoscale devices below  $T \sim 1$  mK is a formidable challenge due to poor thermal contact as well as microwave and other heating, often resulting in device and/or electron temperatures raised well above the refrigerator temperature. Therefore, significant progress beyond the status quo in both cooling techniques and thermometry is necessary.

## 3.2 Strategy to approach submillikelvin sample temperatures

One approach to overcome these difficulties uses Ag sinters [14, 81, 82] to thermalize the sample wires [35], pioneered by the Florida group [39, 83]. Another approach — pursued by our Basel group [84] — is to use nuclear cooling [14, 81, 82] on the sample wires, with the potential to advance well into the microkelvin range. Thermometry in this regime [14, 81, 82] typically faces similar challenges as cooling nanostructures and is ideally integrated on-sample. Among numerous sensors [57], Coulomb blockade thermometers [72] (CBTs) are simple to use and self-calibrating yet offer high accuracy, demonstrated down to 20 mK [75]. Here, we present an improved nuclear refrigerator (NR) for cooling nanoelectronic samples and use it to investigate CBTs and their mechanisms of cooling.

### 3.2.1 Nuclear refrigerator and microwave filtering scheme

We employ a novel scheme for cooling electronic nanostructures into the microkelvin regime by thermalizing each sample wire directly to its own, separate nuclear refrigerator [84]. In this scheme, the sample cools efficiently through the highly conducting wires via electronic heat conduction, bypassing the phonon degree of freedom since it becomes inefficient for cooling at low  $T$ . A prototype of this refrigerator presented in Ref. [84]



has been significantly improved in a second generation system, briefly outlined below and in Fig. 16.

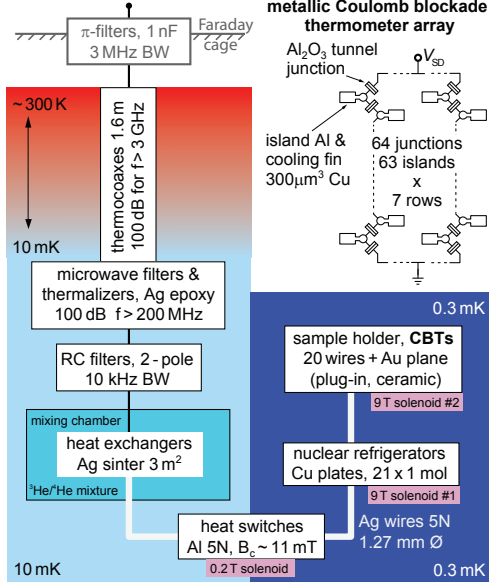


Figure 16: Layout of novel nanosample microkelvin refrigerator and CBT array. Radiation shields (not drawn) are attached to the still and cold plate ( $\sim 50$  mK). The RC filters are  $820 \Omega / 22$  nF and  $1.2$  k $\Omega / 4.7$  nF. The 21 NR plates are  $0.25 \times 3.2 \times 9.0$  cm<sup>3</sup> each, amounting to 64 g Cu per plate.

A network of 21 parallel NRs is mounted on a rigid tripod intended to minimize vibrational heating. Two separate 9 T magnets allow independent control of the NR and sample magnetic field.

Several stages of thermalization and filtering are provided on each sample wire (see Fig. 16). After  $\pi$ -filter and thermocoax [54], each lead passes through a Ag-epoxy microwave filter [3], followed by a RC filter. Each wire then feeds into a Ag-sinter in the mixing chamber, emerging as a massive high-conductivity Ag wire. After Al heat-switches with fused joints, each lead traverses a separate Cu-NR via spot welded contacts, terminating in an easily-exchangeable chip carrier plugged into Au-plated pins

which are spot welded to the Ag wires. Therefore, excellent thermal contact ( $< 50 \text{ m}\Omega$ ) is provided between the bonding pads and the parallel network of 21 Cu pieces — the micro kelvin bath and heart of the nuclear refrigerator — while maintaining electrical isolation of all wires from each other and from ground, as required for nanoelectronic measurements.

### 3.2.2 Performance of the nuclear refrigerators

The performance of the NRs is evaluated in a series of demagnetization runs. The temperature  $T_{Cu}$  of the Cu pieces is obtained using a standard technique [14, 82, 84]: after demagnetization, we apply power on heaters mounted on some of the NRs and evaluate the warm-up time-dependence  $T_{Cu}(t)$  measured with Lanthanum Cerium Magnesium Nitrate (LCMN) thermometers above 2 mK. This allows us to determine both the temperature  $T_{Cu}$  of the Cu-NRs after demagnetization as well as a small field-offset. For each demagnetization run, the NRs are precooled to  $T_i \sim 12 \text{ mK}$  in a  $B_i = 9 \text{ T}$  magnetic field and then demagnetized to temperatures as low as  $T_f \sim 0.3 \text{ mK}$  after the field has been slowly ramped down to  $T_f \sim 0.135 \text{ T}$ , giving efficiencies  $(T_i/T_f)/(B_i/B_f) \gtrsim 60\%$ . Reruns showed excellent repeatability, allowing us to chart  $T_{Cu}$  for various  $B_f$ . To determine  $T_{Cu}$  during the CBT experiments, we use the LCMN thermometers above 2 mK, warm-up curves at the lowest  $B_f$  and in-between, the pre-charted  $T_{Cu}$  values.

## 3.3 Electron temperature measurements

### 3.3.1 CBT sample overview

The network with 21 NRs allows measurements of several CBTs (2-wire each). The CBT devices are Au-wire bonded and glued to the Au backplane of the chip carrier which is also cooled with a NR. Each CBT consists of 7 parallel rows of 64 Al/Al<sub>2</sub>O<sub>3</sub> tunnel-junctions in series with an area of  $2 \mu\text{m}^2$  fabricated using e-beam lithography and shadow evaporation. The process used allows oxidation at elevated temperatures, giving junction resistances up to  $1 \text{ M}\Omega/\mu\text{m}^2$ . Each island extends into a large cooling fin made

from Cu, since Cu gives excellent electron-phonon (EP) coupling. A small  $B \sim 150$  mT is applied perpendicular to the sensor wafer to suppress the superconductivity of the Al. The differential conductance through a CBT sensor was measured with a standard lock-in technique adding a small ac excitation  $V_{ac}$  to a dc bias  $V_{SD}$ . Note that only 1/64 of the applied voltage drops across each junction and the sensor resistance is 64/7 times the junction resistance  $R_j$ , assuming identical junctions.

### 3.3.2 CBT performance for different sensors

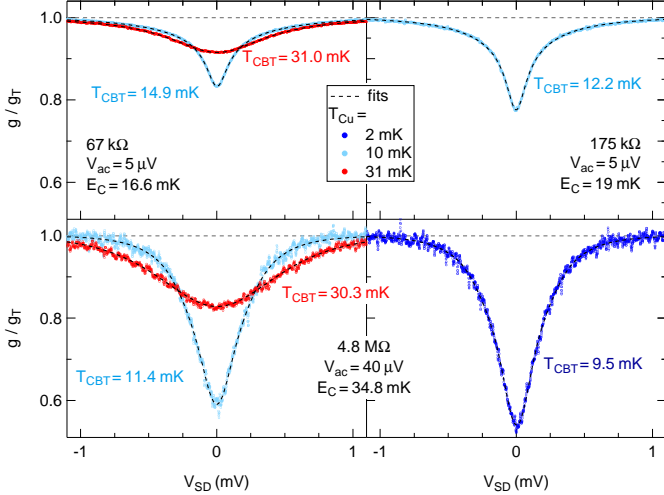


Figure 17: CBT normalized differential conductance  $g/g_T$  versus source-drain dc bias  $V_{SD}$  for various NR temperatures  $T_{Cu}$  as color-coded, with resulting  $T_{CBT}$  ( $\delta g$  method, see text) given adjacent to each trace. Data from a 67 k $\Omega$ , 175 k $\Omega$  and 4.8 M $\Omega$  CBT is shown. Dashed curves are fits to a model (see text). Note lower noise in low- $R$  sensors due to larger resulting currents.

We investigated CBTs with various  $R$ , see Fig. 17. Due to Coulomb blockade effects, the conductance around  $V_{SD} = 0$  is suppressed below the large-bias conductance  $g_T$ . Both width and depth  $\delta g = 1 - g(V_{SD} = 0)/g_T$  of the conductance dip are related to the CBT electron temperature  $T_{CBT}$ . To extract  $T_{CBT}$ , we perform fits (dashed curves)

using a numerical model from Ref. [71]. We find excellent agreement between model and data (see Fig. 17). Independently,  $T_{CBT}$  can be obtained [71] from the conductance dip  $\delta g = u/6 - u^2/60 + u^3/630$  with  $u = E_C/(k_B T_{CBT})$  and charging energy  $E_C$ . We first extract  $E_C$  at high- $T$  assuming  $T_{Cu} = T_{CBT}$  and then use this  $E_C$  to extract  $T_{CBT}$  from  $\delta g$  everywhere. While both methods produce very similar  $T_{CBT}$  (deviating slightly only at the lowest  $T$ ), the  $\delta g$  approach makes no *a priori* assumptions about the cooling mechanism, allowing us an unbiased investigation, though now requiring high- $T$  calibration against another thermometer. All  $T_{CBT}$  values given here are from the  $\delta g$  method.

### 3.4 CBT cooling mechanism

#### 3.4.1 Theoretical model including EP and WF cooling

The thermalization properties of  $T_{CBT}$  of the lowest and highest  $R$  CBTs are displayed in Fig. 18 for a wide range of  $T_{Cu}$  from 0.5 mK to 100 mK. As seen, excellent agreement is found between  $T_{CBT}$  and  $T_{Cu}$  at high temperatures, as expected. Further,  $T_{CBT}$  is seen to lie well above  $T_{Cu}$  at the lower temperatures (see Fig. 17 and 18), decoupling fully from  $T_{Cu}$  well below 10 mK. We note that  $V_{ac}$  was experimentally chosen to avoid self-heating. Also, the 4.8 M $\Omega$  sensor reaches lower temperatures than the other, lower impedance CBTs, consistent with better isolation from the environment, since the power dissipated is proportional to  $V_{env}^2/R_j$ , with environmental noise voltage  $V_{env}$ .

To model the CBT thermalization[71], we write down the heat flow  $\dot{Q}_i$  onto a single island  $i$  with electron temperature  $T_i$ :

$$\dot{Q}_i = \frac{V_j^2}{R_j} + \sum_{\pm} \frac{\pi^2 k_B^2}{6e^2 R_j} (T_{i\pm 1}^2 - T_i^2) - \Sigma \Omega (T_i^5 - T_p^5) + \dot{Q}_0 \quad (14)$$

where  $\dot{Q}_0$  is a parasitic heat leak and  $V_j$  is the voltage drop across the junction, appearing here in the Joule heating term.  $\Sigma$  is the Cu EP coupling constant,  $\Omega = 300 \mu\text{m}^3$  the island volume and  $T_p$  the phonon bath temperature assumed to be equal to  $T_{Cu}$ .

This is well justified by the high thermal conductance between the NRs and bonding pads. Note that at  $T \ll 1$  K, the sample-to-Au-backplane interface resistance (Kapitza) is small compared to the EP coupling resistance [71]. Within this model, two cooling mechanisms are available: Wiedemann-Franz (WF,  $T^2$  term) and EP cooling. Note the strong  $T^5$  dependence of the EP term, ultimately rendering WF cooling dominant at sufficiently low  $T$ . Assuming one mechanism and simplifying to only one island gives a saturation curve  $T_{CBT} = (T_S^p + T_{Cu}^p)^{1/p}$ , with a CBT saturation temperature  $T_S$  and an exponent  $p$ , corresponding to  $p = 2$  for WF-electron cooling and  $p = 5$  for EP cooling.

### 3.4.2 Measured cooling power-laws versus theory

We study the mechanism of thermalization by fitting the saturation curve first to the 4.8 M $\Omega$  data. We find very good agreement, giving  $p = 4.9 \pm 0.4$  (see Fig. 18), indicating that EP coupling presents the dominant cooling mechanism, limiting  $T_{CBT}$  to 9.2 mK even though  $T_{Cu} = 0.75$  mK. Using  $\dot{Q}_0 = \Sigma \Omega T_{CBT}^5$ , a small parasitic heat leak  $\dot{Q}_0 = 40$  aW results for each island, with  $\Sigma = 2 \times 10^9$  Wm $^{-3}$ K $^{-5}$  from Ref. [71]. We speculate that  $\dot{Q}_0$  could be caused by electrical noise heating such as microwave radiation, intrinsic residual heat release from materials used or other heat sources. Considering the high- $R$  junctions and correspondingly weak WF cooling, it is not surprising that EP coupling is dominant here.

When analogously examining the low- $R$  sensors, on the other hand, we find  $p = 3.9 \pm 0.4$  and  $T_S = 13.4$  mK for the 67 k $\Omega$  sensor (see inset Fig. 18), and even  $p = 2.7 \pm 0.2$  and  $T_S = 6.9 \pm 0.1$  mK for a 134 k $\Omega$  sensor (not shown) mounted on a conventional dilution refrigerator (base- $T \sim 5$  mK) with improved filtering and chip carrier. Note that  $T_S$  is the extrapolated  $T_{Cu} = 0$  saturation- $T$ . The lowest  $T$  measured here was  $7.5 \pm 0.2$  mK. These power-laws far below  $p = 5$  indicate that EP cooling is no longer dominant but, rather, a more efficient mechanism  $p < 5$  takes over at the lowest- $T$  in the low- $R$  sensors.

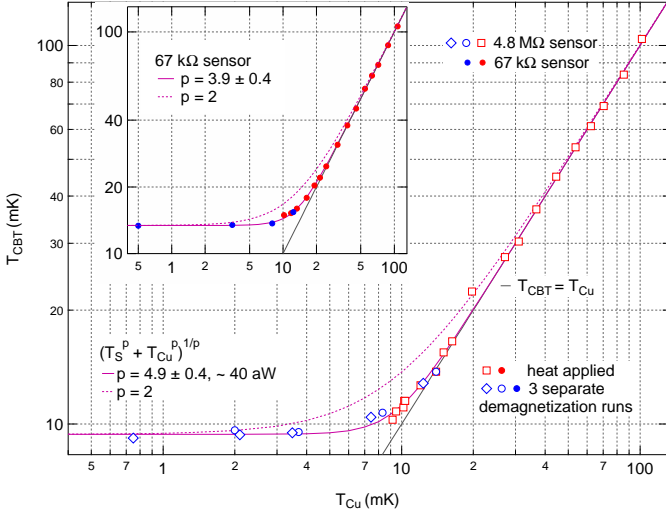


Figure 18: CBT electron temperature  $T_{CBT}$  versus NR temperature  $T_{Cu}$  for 4.8 M $\Omega$  (open markers) and 67 k $\Omega$  sensors (filled markers, same axes on inset as main figure). Below 10 mK, the data is obtained in 3 demagnetization sweeps (blue markers) with  $B = 9$  T, 5 T, 2 T, 1 T and 0.4 T in a typical run, ramped at 1 T/h above 1 T and 0.5 T/h below. Error bars are about the size of the markers. Purple curves are  $T_{CBT}$  saturation curves (see text).

### 3.5 Summary

In summary, we have demonstrated operation of the NRs down to 0.3 mK while the CBTs cool as low as 7.5 mK. Though the high- $R$  sensor is obviously cooled by EP coupling, the low- $R$  sensors, interestingly, appear to be entering a different cooling regime. However, the low- $R$  sensors have slightly higher  $T_{CBT}$  given the same environment, consistent with stronger coupling to the environment. The lowest CBT temperatures are limited by the parasitic heat leak, which is drained by the cooling channels available.

To further improve the sensor performance, the cooling-fin volume can be increased or the heat leak can be reduced, potentially using improvements in microwave shielding and filtering, e.g. using on-chip capacitors, metal planes or alternative array designs. Such efforts will strongly enhance thermalization if a more efficient cooling mechanism is

indeed present, since otherwise, in the EP regime, reducing  $\dot{Q}_0$  by 5 orders of magnitude will only reduce  $T_{CBT}$  by a factor of ten.

An alternative avenue based on quantum dot CBTs, e.g. in GaAs, might also be rewarding, taking advantage of a much larger  $E_C$  and level spacing  $\Delta$ . The resulting reduced sensitivity to the environment might allow a single dot to be used, rather than an array, cooling the reservoirs directly via the WF term, rather than through a long series of junctions.

### **Acknowledgments**

We would like to thank R. Blauwgeers, G. Frossati, R. Haley, G. Pickett, V. Shvarts, P. Skyba and A. de Waard for very useful discussions. This work was supported by the Swiss Nanoscience Institute (SNI), NCCR QSIT, Swiss NSF, ERC starting grant, and EU-FP7 SOLID and MICROKELVIN.





## 4 Luttinger Liquid Theory and GaAs CEO Wires

Whereas Fermi liquid theory is very successful in describing two and three dimensional electronic systems by means of perturbation theory, it completely breaks down for 1D-conductors. This is due to the enhanced coulomb interaction in one dimensional systems which leads to a failure of any perturbative approach. However, such systems can be described in the framework of Luttinger liquid theory. In contrast to higher dimensional systems, where spin and charge are bound in long lived quasi-particles, the fundamental excitations of 1D-conductors are collective spin and charge density waves. Interacting many-body quantum systems are of fundamental interest in physics. They can arrange themselves in complicated ways to reduce their energy which can lead to exotic phases of matter. Unlike in higher dimensions where such theories do not exist, Luttinger liquid theory (LL) offers a model to solve interacting 1D problems exactly (a linear dispersion is assumed).

In a recent theory from B. Braunecker, P. Simon and D. Loss interactions between a LL and the nuclear spins in the host material were studied [1, 40]. Though direct interactions between nuclear spins are weak, it turns out that they are well coupled through the electronic system in a RKKY-type of interaction. The authors from ref. [1] predict that below a critical temperature  $T^*$  the system undergoes a phase transition and forms a new, strongly correlated state of matter: a fully polarized nuclear spin helix. In the ordered phase half of the conducting electron modes are frozen out and consequently the conductance is predicted to drop by a factor of two.

Measurements in GaAs cleaved edge overgrowth (CEO) quantum wires by A. Yacoby *et al.* showed reduced, nonuniversal conductance quantization [2]. Furthermore, the deviation from universal conductance quantization was found to increase with decreasing temperature, measured down to 300 mK. Despite significant efforts from both, experimental and theoretical side, there is no satisfactory explanation for these observations so far.

Motivated by the recent theoretical work from B. Braunecker *et al.* on nuclear magnetism in the LL-regime with an estimated ordering temperature of  $T^* \approx 75$  mK (for CEO quantum wires in [2]) and previous measurements on CEO wires by A. Yacoby *et al.* where observed reduced conductance steps might indicate the onset of such a phase transition, low temperature transport measurements were performed at University Basel on these quantum wires. The measurements were done in collaboration with the Yacoby group from Harvard University at Cambridge USA on the same kind of CEO wire samples (grown by Loren Pfeiffer and coworkers at Bell Labs more than 10 years ago) as used in previous experiments by the Yacoby group. We also worked in close collaboration with people from several theory groups, in particular B. Braunecker, D. Loss, P. Simon, T. Meng and D. Maslov. Furthermore, we greatly benefited from discussions with O. Auslaender and his explanations on tunnel spectroscopy measurements in CEO wires.

This chapter is structured as follows: At first a short introduction to LLs is given in sec. 4.1 and subsequently nuclear order in 1D quantum wires is discussed in more detail (sec. 4.2). Before giving a detailed overview on the CEO wires used in this work (sec. 4.4), Yacobys findings [2] on reduced conductance steps will be reviewed in sec. 4.3. Many important physical parameters can be extracted from tunnel spectroscopy measurements on the CEO double wire samples such as density, subband spacing and interaction strength  $K_C$ . Such spectroscopy measurements were first demonstrated by O. Auslaender *et al.* in [85] on quantum wires nominally identical to the CEO wires in this thesis. We use the gate modulation technique (tunneling transconductance) from [8] to measure the density in our wires. The electron density is a very important quantity that e.g. determines the Fermi energy, the interaction parameter  $K_C$  and consequently the spin and charge velocities. Only the precisely known electron density (as a function of top gate voltage) allowed to identify measured conductance oscillations in the tunneling current (and in direct transport measurements) as Fabry-Perot resonances which is the topic of sec. 4.5.

Finally, chapter 5 is devoted to the reduced conductance step size in CEO wires, i.e. we extend A. Yacoby's measurements down to lower system temperatures and find that the first upper wire conductance step in a CEO double quantum wire saturates below  $T_R \approx 75$  mK at  $1 e^2/h$ , consistent with the predicted low temperature limit (for a clean LL) by B. Braunecker *et al.* in [1].

## 4.1 Basic introduction to Luttinger liquids

### 4.1.1 Luttinger liquid versus Fermi liquid

Fermi liquid theory is a very powerful tool for solving many-Fermion problems in two and three dimensions. It assumes that interactions are small enough to only slightly modify the single particle wave function. This allows one to solve first the non-interacting case and then approach the interacting case by means of perturbation theory (applied to the solution for the non-interacting case). For temperatures much smaller than the Fermi temperature  $T \ll T_F$ , the system can be described by its Fermi surface (the ground state) and its low-energy excitations, the so called quasi-particles. They possess the same quantum numbers as the original particles, but their kinematic (e.g. effective mass) and thermodynamic parameters (specific heat, susceptibility) get renormalized by interactions [86].

The situation drastically changes upon reducing the dimensionality. The fact that electrons in 1D systems electrons can not avoid each other leads to a collective behavior and consequently to a complete breakdown of Fermi liquid theory, where free fermions are assumed. Instead of quasiparticles with defined charge and spin, the fundamental excitations in these systems are spin and charge density waves of bosonic character.

Inspired by Bloch's work on the stopping power of charged particles [87], Tomonaga proposed a 1D model of interacting fermions and solved it by means of acoustic sound waves. The assembly of fermionic quasi-particles is hereby treated as sound quanta, i.e. bosonic particles. The important mathematical step is a replacement of the quantized field variables  $\Psi$  and  $\Psi^*$  with the ones for the sound field, being the density  $\rho$  and its

appropriate conjugate. The model proposed by S. Tomonaga in 1950 [88] was generalized by J.M. Luttinger in 1963 [89] and correctly solved by D.C. Mattis and E.H. Lieb in 1965 [90].

#### 4.1.2 Physical properties of Luttinger liquids

The fundamental excitations of these Tomonaga-Luttinger liquids (LL) are the charge and spin density waves. In the limit of the non-interacting case  $K_c = K_s = 1$ , with  $K_c, K_s$  being the interaction parameters for charge and spin ( $K > 1$ : attractive,  $K < 1$  repulsive interactions), both waves travel with the Fermi velocity  $v_F$ . While repulsive interactions increase the velocity for charge density waves  $v_c = v_F/K_c$ , they do not affect the one for spin density waves, at least up to first order. The fact that spin and charge density waves travel at different velocities leads to spin-charge separation in 1D systems, first observed in tunnel spectroscopy measurements by O. Auslaender *et al.* in 2005 [8] on GaAs cleaved edge overgrowth double quantum wires. Momentum is conserved for electrons tunneling between the parallel quantum wires (translational invariance) and can be tuned with a magnetic field  $B_y$  applied in-plane with orientation perpendicular to the wires. Together with a source drain bias (energy control) this allows for spectroscopy measurements i.e. extraction of the quantum wire dispersions which, due to interactions, are different for spin and charge modes. Spin charge separation was later on verified on CEO wires in [91] and on surface gated GaAs 1D wires [92]. This behavior is completely different from 2D and 3D systems where spin and charge are inseparably bound in the quasi-particles that carry both properties.

Another peculiar effect in LLs is the so called charge fractionalization, demonstrated on CEO wires by H. Steinberg *et al.* in 2008 on CEO double quantum wires. Since only two directions of motion exist in 1D, all excitations can be grouped into either left or right movers. Charge that is injected into a LL will decompose into left and right moving charge density waves. In contrast to the quasi-particles in 2D and 3D, the charge of these waves is not quantized, i.e. can take any arbitrary value. Injection of a right moving electron into the bulk of a LL liquid is predicted to result in right and left

moving charge density waves with fractional charges  $f_0e$  and  $(1 - f_0)e$  respectively. In the non-interacting limit,  $f_0$  approaches unity and the injected electron will continue as right mover.

The correlations between the spin and charge excitations translate into interaction-dependent (non-universal) power laws in many physical properties, whereas ordinary metals are characterized by universal powers [86]. For example tunneling into a clean LL is strongly suppressed at the Fermi energy. The tunneling conductance  $G$  is predicted to vanish in a power law fashion  $G(T) \propto T^\alpha$  for small bias voltage  $eV \ll k_B T$ . This is in clear contrast to Fermi liquid theory where the tunneling conductance is energy independent resulting in bias and temperature independent tunneling conductance [93]. Experimentally such power laws in the tunneling conductance have been observed in carbon nanotubes [93, 94], in GaAs cleaved edge overgrowth wires [85, 95, 96] and for tunneling into fractional quantum hall states [97–99]. Correlation functions were also studied for Bose-Einstein condensates (BEC). Interference of two quasi one dimensional condensates of variable length also indicate LL behavior [100, 101].

In addition, O. Auslaender *et al.* studied low temperature conductance of a one-dimensional island embedded in a single mode CEO wire [102]. They observe that the intrinsic linewidth decreases in a power law fashion with temperature and find good agreement with Furusaki’s model for resonant tunneling in a LL.

A well known effect is the conductance quantization in 1D system (see next section), i.e. the current through a narrow channel (order of Fermi wavelength) drops in a staircase manner as a function of channel width. While clear conductance steps with long and flat plateaus are seen in CEO wires (see e.g. [2, 85]), a first observation of conductance steps was reported in [103] for carbon nanotubes.

#### 4.1.3 Conductance quantization in 1D

The Landauer-Büttiker formalism [104–106] predicts that in absence of external magnetic fields, transport through one dimensional systems with adiabatic contacts (smooth variation of the contact potential on the scale of the Fermi wavelength) is quantized

in units of  $T \cdot 2e^2/h$ ,  $g = NT \cdot 2e^2/h$ . Here,  $N$  denotes the number of transmitted channels and  $T$  is the transmission probability ( $T=1$  in the ballistic case). This effect was observed first by B. J. van Wees *et al.* and D. A. Wharam *et al.* in 1988 [106, 107] in GaAs quantum point contacts (narrow constriction of the order  $\lambda_F$ ) which can be viewed as short wires. The universal conductance quantization does not depend on microscopic details and has been reported for quantum point contacts in various different material systems. It is a consequence of the reduced Fermi velocity  $v_F$ , when moving along a conductance plateau toward the pinch off regime ( $v_F = \hbar k/m = n\hbar\pi/2m$  in 1D), that is compensated by the increased density of states  $DOS_{1D}$  in one dimensional systems ( $DOS_{1D} = 2m/\hbar^2\pi k$ ).

For a correct description of one dimensional systems including interactions, Luttinger liquid theory has to be invoked. It was shown theoretically (W. Apel, T. M. Rice [108] and C. L. Kane, M. P. A. Fisher [109, 110]) that the universal conductance quantization is modified for an infinitely long LL in the presence of interactions. In case of repulsive interactions  $K < 1$ , the conductance reduces to  $g = K \cdot e^2/h$  per spin orientation. However, in every real transport measurement the Luttinger liquid is finally connected to non-interacting Fermi leads. D. Maslov and M. Stone [111], I. Safi and H. J. Schulz [112] and V. V. Ponomarenko [113] showed in 1995 that the conductance for a clean Luttinger liquid connected to noninteracting reservoirs is  $2e^2/h$  regardless of interactions in the wire. In the same year, D. Maslov showed that this result is again modified in the presence of weak disorder. Here, the correction to the universal conductance quantum does indeed depend on interactions in the wire and is temperature dependent [114]. Such a reduction in weakly disordered  $2 - 10 \mu\text{m}$  long side gated GaAs quantum wires has been observed by S. Tarucha *et al.* in 1995 [115]. In contrast to Yacobys measurements on CEO wires, the conductance plateaus are short (small density variation within one conductance plateau) and show signs of disorder. In addition, the observed reduction is only a few percent compared to a 25% reduction in the CEO wires despite their long and flat conductance plateaus. Measurements performed by E. Levy *et al.* in 2006 on weakly disordered GaAs quantum wires [116], showed good agreement with Maslovs theory for transport through dirty LLs.

## 4.2 Luttinger liquid and nuclear spins

### 4.2.1 Nuclear magnetism and electron order in a Luttinger liquid

The system considered in [1] is a one dimensional conductor in the LL state, surrounded by a 3D matrix of nuclear spins from the surrounding host material. The Kondo-lattice-type Hamiltonian for the considered system reads:

$$H = H_{el}^{1D} + \sum_i A_0 \mathbf{S}_i \cdot \mathbf{I}_i + \sum_{ij, \alpha, \beta} v_{ij}^{\alpha\beta} I_i^\alpha I_j^\beta \quad (15)$$

$A_0$  is the hyperfine coupling constant,  $\mathbf{S}_i$  and  $\mathbf{I}_j$  represent electron and nuclear spin operators respectively. Indices  $i$  and  $j$  run over 3D lattice sites. The first term describes the electronic interacting 1D system, the second term couples electronic and nuclear system, also known as hyperfine coupling, and the last term represents the nuclear dipole-dipole interaction (quadrupolar splitting for  $i = j$ ). Since associated temperature scales in the order of  $1 \mu\text{K}$  are much lower than what is achieved in experiments, the last term in eq. 15 is neglected in the following.

Furthermore, the 1D conductor considered here is assumed to be confined to a single transverse mode with higher harmonics clearly split off (large subband spacing). Taking this into account, the 3D system can be converted into the equivalent 1D Hamiltonian:

$$H = H_{el}^{1D} + \sum_i \frac{A_0}{N_\perp} \mathbf{S}_i \cdot \tilde{\mathbf{I}}_i \quad (16)$$

Here  $i = i_{II}$  runs over all lattice sites of the 1D chain.  $\tilde{\mathbf{I}}_i$  represents the ferromagnetic component of all nuclear spins  $N_\perp$  that lie on the same cross section of the 1D conductor. The size of the cross sectional area is given by the confinement. For the present GaAs cleaved edge overgrowth wires in the single mode regime this area is roughly 50 lattice constants in both directions (perpendicular to the 1D channel), resulting in  $N_\perp \approx 2500$ . It is shown in ref. [1] that the maximal alignment  $\tilde{I} = N_\perp I$  minimizes the effective Ruderman-Kittel-Kasuya-Yoshida (RKKY) interaction i.e. the coupling of

nuclear spins through the conducting electrons and hence the assembly of nuclear spins within a section behaves like a single large nuclear spin  $N_{\perp} I$ . This situation is schematically depicted below in fig. 19.

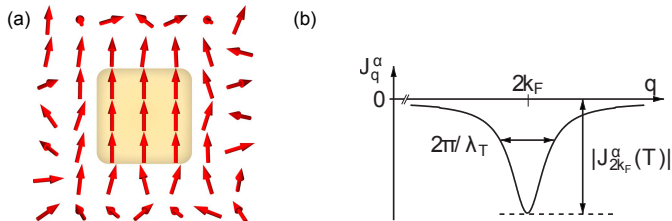


Figure 19: (a) Cross section through a 1D conductor showing the  $N_{\perp} \approx 2500$  ferromagnetically locked nuclear spins behaving like a single large spin  $\tilde{I} = N_{\perp} I$ . A sketch of the RKKY interaction is shown in (b).  $\lambda_T$  is the thermal wavelength and  $q$  represents the momentum transfer. Both graphs were taken from ref. [1].

Since timescales for the electronic system are much faster than for the nuclear spin system, the Overhauser field (generated by the assembly of nuclear spins) can be treated as a static effective B-field for the electrons. The corresponding Hamiltonian for the electronic system is given by the Tomonaga-Luttinger model. The dispersion relation is then linearized around the two Fermi points. It is important to note that though excitations of the system are low energetic (close to the Fermi energy), coupling to higher energies is possible through interactions which makes a description necessary that includes a large energy window. The cut-off is done at the highest energy scale for the system  $\Delta_a = \hbar v_F/a$ , given by the lattice spacing  $a$  (5.65 Å in GaAs).

The calculated RKKY interaction reaches its minimum at  $q = \pm 2k_F$ . Its width (fig. 19(b)) is given by the thermal length  $\lambda_T = \hbar v_F/k_B T$  (for  $T = 0$  the RKKY interaction diverges at  $2k_F$ ). Nuclear spins minimize their ground state energy when aligning in the shape of a helix with periodicity  $2k_F$ . Each individual cross section is hereby fully polarized as shown in fig. 19(a). As for the regular Peierls transition [117], where the system turns insulating in an external perturbation with periodicity  $2k_F$  (see fig. 20(b)), a gap opens at the Fermi energy due to the nuclear helix. However, due to the



chirality of the helix only left moving electrons with spin down and right movers with spin up are mixed by the  $2k_F$  perturbation which leads to a partially gapped system as shown in fig. 20(a).

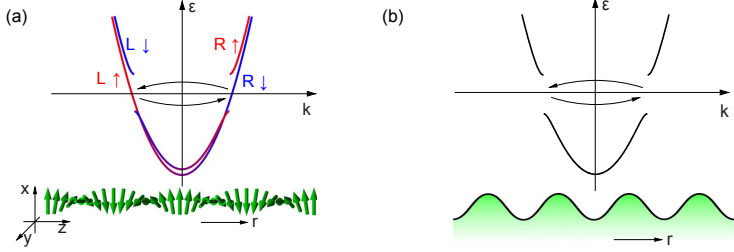


Figure 20: (a) Electronic dispersion in the ordered state, indicated by the nuclear spiral helix (green arrows). Black arrows indicate spin selective scattering between  $L\downarrow$  (blue) and  $R\uparrow$  (red) with  $2k_F$  momentum transfer that leads to a partial gap. Gapless modes are also indicated. (b) depicts the situation for the regular Peierls transition where due to scattering (black arrows) in an external potential with periodicity  $2k_F$  (green) the system turns insulating. Both figures were taken from ref. [118].

Since half of the of the low energy modes remain, the conductance is predicted to drop by a factor of two when the system reaches its ordered state. A closer inspection of the remaining modes ( $L\uparrow$  and  $R\downarrow$ , see fig. 20(a)) reveals that the system acts as a perfect spin filter in the ordered phase.

The opening of a partial gap in the electronic dispersion can therefore be seen as spin selective Peierls transition. B. Braunecker *et al.* showed in [118] that the spin orbit gap that opens for a 1D conductor with strong spin orbit interaction in a perpendicular (to the spin orbit axis) magnetic field can be mapped onto a spin selective Peierls transition.

#### 4.2.2 Spin selective Peierls in a 1D wire with SOI

In a 1D conductor with strong spin orbit interaction (SOI), the dispersion splits up into two branches that are symmetrically shifted away from  $k = 0$  by the momentum  $\sigma k_{SO}$ . The degeneracy point at  $k = 0$ , where the two spin-split subbands cross, can be lifted in an external magnetic field applied perpendicular to the spin orbit axis which leads

to the opening of a gap  $\Delta$  (intrinsic SOI may also lift the degeneracy).

It was shown by B. Braunecker *et al.* [118] that the spin-dependent gauge transformation  $\Psi_\sigma(r) \rightarrow e^{i\sigma k_{SO}r} \Psi_\sigma(r)$  eliminates the  $\sigma k_{SO}$  shift, i.e. the hamiltonian  $H = H_0 + H_{SO} + H_\Delta$  reduces to  $H = H_0 + H_\Delta$ . In return, the uniform gap  $\Delta$  is replaced by a spiral field  $\Delta(r)$  with periodicity  $\lambda_{SO}/2$ . In other words, a 1D conductor with strong SOI in an external B-field  $\Delta$  is equivalent to a 1D conductor placed into a spiral magnetic field with periodicity  $\lambda_{SO}/2$ .

For  $k_{SO} = k_F$ , the consequences for the electronic system are the same as in the phase transition discussed in the previous section, i.e. the conductance drops from  $2e^2/h$  to  $1e^2/h$  and the remaining modes provide a perfect spin filter composed of  $R\uparrow$  and  $L\downarrow$  movers [119, 120]. The observation of such a spin-orbit gap was reported for a GaAs cleaved edge overgrowth hole gas in [121].

In contrast to the 1D conductor with strong SOI, the self ordering process from sec. 4.2.1 opens the gap automatically at the Fermi energy. Therefore, without external magnetic field, the conductance of a quantum wire is expected to drop by exactly a factor of two upon lowering the system temperature below  $T^*$  where half of the conducting modes freeze out. For a clean LL connected to Fermi leads with predicted Landauer conductance quantization (regardless of interactions in the wire [111]) this implies a conductance reduction from  $2e^2/h$  to  $1e^2/h$ .

The authors from ref. [1], using typical experimental parameters, estimate a crossover temperature in the milikelvin regime for GaAs cleaved edge overgrowth wires ( $T^* \approx 75$  mK) and also for  $^{13}\text{C}$  carbon nanotubes ( $T^* \approx 11$  mK in CNTs).

### 4.3 Nonuniversal conductance quantization in quantum wires

Cleaved edge overgrowth (CEO) allows for the fabrication of one dimensional ballistic quantum wires in GaAs [10]. In 1996, A. Yacoby *et al.* observed nonuniversal conductance quantization in CEO quantum wires which was reported in ref. [2]. Fig. 21, taken from [2], shows the conductance through a  $2\mu\text{m}$  long CEO wire as a function of its top gate.

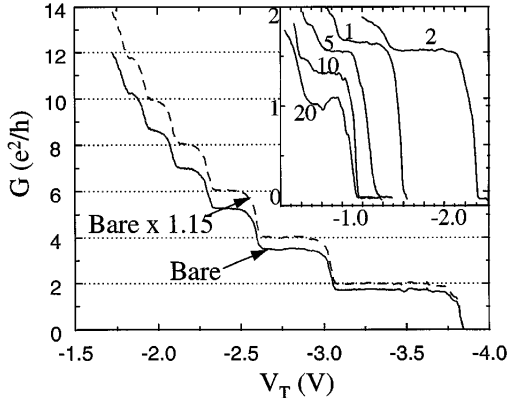


Figure 21: Conductance of a CEO wire as a function of top gate voltage (solid trace). A scaling with a factor of 1.15, maps the measured data on universal conductance steps (dashed trace). The inset shows the conductance for the lowest mode in CEO wires of various length. This graph was taken from [2].

The conductance drops in clear steps of equal height as the electron density in the wire is lowered with the top gate. However, the step height is found to be suppressed below the universal conductance quantum of  $2e^2/h$ . In fact, a rescaling of the measured conductance with a scaling factor of 1.15 restores the universal conductance steps. This excludes a series resistance as possible origin for the reduction. A stronger reduction was observed in longer quantum wires as shown in the inset of fig.21. However, in contrast to the short wires, the conductance plateaus are not completely flat for the long quantum wires, probably a sign of finite disorder. The temperature dependence for the first mode in a  $2\mu\text{m}$  long CEO wire is shown in fig.22. Due to the large subband spacing, the lowest mode in the measured CEO wires stays flat even at large temperatures  $T_R \gg 4.2\text{K}$ . Upon increasing the temperature, the conductance step height increases and approaches  $2e^2/h$  at the highest temperatures.

A similar behavior was found when measuring the conductance at low temperature as a function of applied source drain bias. Here the differential conductance  $g = dI/dV$  even exceeds  $2e^2/h$  for large bias, the linear conductance  $G = I/V$  however stays below the universal conductance quantum even at the highest DC bias.

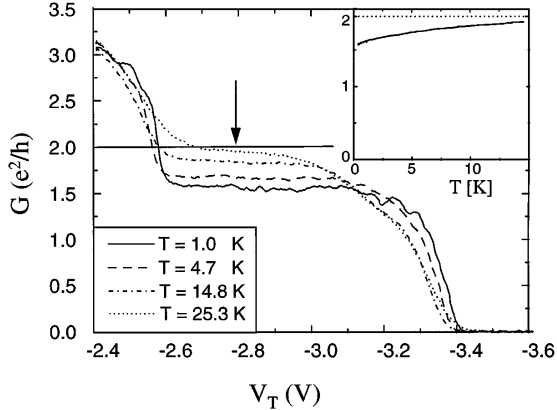


Figure 22: Zoom in on the first conductance step of a cleaved edge overgrowth wire for various temperatures. The inset shows the conductance as a function of temperature for fixed gate position, indicated by the black arrow. This graph was taken from [2].

In contrast to previous experiments, where conductance reduction as a function of temperature was observed [115], the CEO wires measured in [2] (figs. 21, 22) show flat conductance steps which indicates energy independent transmission. Indeed, electron transport through these wires was later on shown to be ballistic, a demonstration of low disorder within the wires. These results are surprising as clean Luttinger liquids (attached to Fermi leads) are predicted to exhibit universal conductance quantization [111] as discussed in sec. 4.1.3.

Three models were proposed in [2] in an attempt to explain the nonuniversal conductance quantization in CEO quantum wires. In the first model, noninteracting electrons were assumed in both, wire and leads. A conductance reduction may then result from nonideal electron transmission. However, long and flat conductance plateaus indicate energy independent transmission which, in a noninteracting theory, leads to temperature independent conductance [2], in contradiction with the experiment. In a second model,  $e - e$  interactions were considered. The conductance for a clean, finite LL connected to Fermi liquid leads is predicted to be  $2e^2/h$  regardless of interactions within the wire [111]. Therefore, in this scenario, finite disorder would have to be assumed in

order to explain reduced conductance. As the strength of  $e - e$  interactions and the temperature dependence are both determined by the electron density in the wire (which significantly changes along the conductance plateau), this is in contradiction to the observation of flat conductance plateaus. In a third model, backscattering within the 1D channel was studied, in combination with scattering between edge channels and 2DEG. Using a Boltzmann approach, the conductance for a CEO was calculated and found to be reduced below the universal one,  $g = 2e^2/h \cdot 1/\sqrt{1 + 2l_{2D \leftrightarrow 1D}/l_{BS}}$ , where  $l_{2D \leftrightarrow 1D}$  is the 2D-1D scattering length and  $l_{BS}$  denotes the backscattering length. LL theory predicts enhanced backscattering and reduced 2D-1D coupling at low temperatures. Therefore, within this model, the conductance is predicted to continuously decrease as a function of temperature. This is in clear contradiction to our experimental findings (see chapter 5), where a low temperature conductance saturation at  $\approx 1e^2/h$  was observed (below  $T_R \approx 75$  mK). We note that A. Yacoby *et al.* already pointed out problems with this model, as it would be very difficult to explain their observation of equally reduced conductance steps for different modes in the wire. In summary, the nonuniversal conductance quantization in CEO quantum wires remains an unsolved problem.

A. Yacoby's previous observations together with the recent theoretical work by B. Braunecker *et al.* on the formation of a nuclear helimagnet for a 3D system of nuclear spins in a LL (with a predicted conductance drop by a factor of two) initiated and motivated this thesis. Further motivation came from low temperature measurements on surface gated GaAs quantum wires [122] where a 0.7 like structure ( $0.7 \cdot 2e^2/h$ ) transformed into a plateau at  $1e^2/h$  (for zero B-field) as a function of side gate voltage, i.e. increased confinement and density.

#### 4.4 GaAs cleaved edge overgrowth (double) quantum wires

GaAs cleaved edge overgrowth (CEO) is a special growth technique that allows very strong confinement in two spacial directions, resulting in quantum wires with very large subband spacings up to 20 meV [123]. Together with a high quality 2DEG, used as a

starting point for the wire fabrication, CEO wires result in one of the best experimental realizations of a Luttinger liquid. Consequently, also the strongest indications for LL behavior were given for these wires (e.g. spin charge separation and charge fractionalization next to power law behavior that was also shown for other 1D systems, see sec. 4.1.2).

In addition to their outstanding physical properties, these wires can be well contacted to 2DEG reservoirs and a single gate allows flexible density tuning e.g. into the single mode regime. Together with a reasonably large estimated crossover temperature of  $T^* \approx 75$  mK compared to 11 mK for CNTs made from pure  $^{13}\text{C}$  (natural abundance of  $\approx 1\%$ ), these wires seem to be the ideal candidates to experimentally approach the predicted phase transition from sec. 4.2.1.

All measurements on CEO quantum wires in this thesis were performed on samples provided by the Yacoby group from Harvard University at Cambridge USA. The fragile (more than 10 year old) samples were shipped already bonded and glued onto a 16 pin DIP socket. In fact, in order not to risk damaging these unique samples by placing them on a different chip carrier that fits our standard sample holders, two new coldfingers were built in regard to the CEO wire measurements.

The CEO wire fabrication process, done by L. N. Pfeiffer *et al.* [123–126], is very challenging and deserves special notice. The main fabrication steps are captured in the following section before proceeding to actual measurements.

#### 4.4.1 Sample fabrication

Starting point for the fabrication of the CEO double wires is a standard GaAs heterostructure grown along the [100] crystal direction with two GaAs quantum wells (QW) [126]. The lower, 30 nm wide quantum well is separated from the upper, 20 nm thick quantum well by a 6 nm thick, 300 meV high  $\text{Al}_{0.3}\text{Ga}_{0.7}\text{As}$  tunnel barrier [85]. Excessive electrons from the silicon  $\delta$ -doping layer, present only above the upper QW, result in a clean 2DEG located 500 nm below the surface (in the upper QW).

After evaporating narrow tungsten top gates the sample is cleaved in ultra high vacuum

and the atomically sharp sample edge is immediately overgrown along the  $[001]$  crystal axis with a modulation doping sequence [126]. This additional doping layer at the sample edge, next to contributing free electrons that are collected in the edge channels and the 2DEG, pulls electrons toward the positively charged Si-donor layer at the cleaved side of the sample thus creating two one-dimensional edge channels (see fig. 23). The purpose of the prefabricated tungsten top gate (yellow stripe in fig. 23) is twofold. First, it allows separating the 2DEG into two parts that act as source and drain contacts for the quantum wire. The width of the top gate hereby defines the length of the quantum wire. Second, it allows density control in the edge channel underneath. A sample schematic is shown in fig. 23. The 2DEG and the two edge channels, upper and lower wire (UW and LW), are schematically indicated in blue.

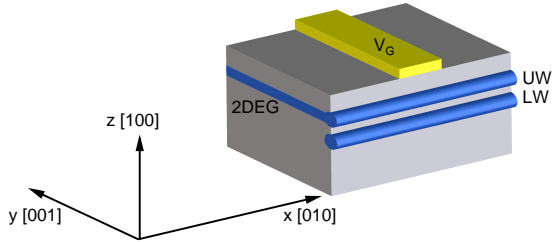


Figure 23: Schematic of the CEO double wire sample. The tungsten top gate (yellow) separates the underlying 2DEG (blue) into source and drain contacts to the edge channels denoted UW and LW (blue tubes). A coordinate system indicates the sample orientation and crystal growth directions.

Crystal growth directions are indicated in the coordinate system adjacent to the sample schematic. We will use this sample orientation for all CEO wire measurements, i.e. we choose the  $x$ -axis along the double wire system and the  $z$ -axis perpendicular to the 2DEG.

#### 4.4.2 Sample properties before and after LED illumination

Fig. 24 shows a picture of a quantum wire sample. Tungsten top gates g2-g7 (light gray) and ohmic indium solder contacts (labeled o1-o4, o7 and o8 in light blue) are visible. A four wire differential conductance measurement as a function of top gate voltage  $g_3$  (faint red gate in the inset), is shown in the main graph as black trace. In the following we only use the term conductance to label the differential conductance. Ohmic o1, o8 serve as source-drain contacts and the voltage drop is measured across ohmics o2 and o7. At zero top gate voltage the whole 2DEG in the upper QW contributes to the current resulting in large conductances around  $600 e^2/h$  ( $\approx 20\Omega/\square$ ). Upon decreasing the gate voltage  $g_3$  the conductance abruptly drops to  $\approx 20e^2/h$  (light gray arrow in fig. 24) when the 2DEG below  $g_3$  is depleted and all current is carried by edge channels. Decreasing  $g_3$  even further will also deplete the edge channels in the gated region and the system turns insulating (black arrows).

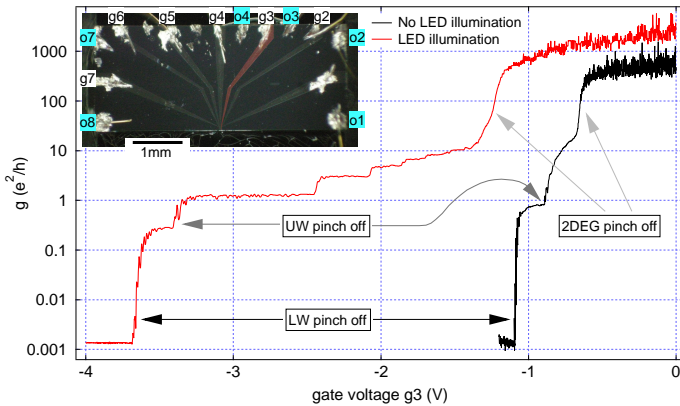


Figure 24: Conductance as a function of top gate voltage  $g_3$  (see artificially red colored gate in the inset) for a GaAs CEO double quantum wire. Black and red represent conductance measurements before and after LED illumination. Arrows indicate the depletion region for the 2DEG (below gate  $g_3$ ). Further arrows indicate depletion of upper and lower edge channels. The inset shows an optical image of the sample with available gates g2-g7 and ohmic contacts o1-o4, o7, o8 as labeled. The cleaved edge is located at the lower sample side.



An AlGaAs infrared (875 nm) light emitting diode (LED) was used to irreversibly increase the electron density in the 2DEG and the quantum wires (warmup to room temperature will recover the initial state). The LED flash is done at 4.2 K with typical currents of few milliampere and illuminations times of a few tens of seconds. After LED illumination, clear conductance steps with long and flat plateaus are observed, see red trace in fig. 24.

Because of the elevated electron density after illumination, more negative top gate voltage is needed to deplete the underlying 2DEG and quantum wires. Due to screening the gating effect of  $g_3$  is stronger on upper than on lower wire modes. Therefore, after depleting all upper wire modes one is still left with the lowest mode of the lower wire ( $LW_1$ ), indicated by dark gray arrows in fig. 24 (also the width of upper and lower QW has to be chosen properly for this situation to apply).

Extracting the density for a given mode (e.g.  $UW_1$ ) as a function of its corresponding top gate is a non trivial task but can be done by means of spectroscopy and will be discussed later. It is fairly simple, however, to measure the 2DEG density by means of the hall resistance  $R_{XY}$ . It turns out that the CEO wire sample allows for decent quantum hall measurements, see fig. 25. At  $B_z = 4$  T the filling factor increases from  $\nu = 1$  to  $\nu = 2$  upon LED illumination (blue and red dashed traces in fig. 25), corresponding to an approximate density change by a factor of 2. Precise information about the 2DEG density is gained by fitting the transversal resistance  $R_{XY}$  (blue and red solid line in fig. 25) in the classical regime (small B-fields) where hall plateaus have not yet developed. We obtain  $n = (1.00 \pm 0.02) \cdot 10^{11} \text{ cm}^{-2}$  before and  $n = (1.91 \pm 0.03) \cdot 10^{11} \text{ cm}^{-2}$  after LED illumination. For visibility reasons the curve fits (black dashed lines in fig. 25), performed in the low B-field regime, are drawn across the whole B-field range.

We note that the actual error margins on the measured 2DEG densities are larger than what is presented in fig. 25, since no corrections have been done to account for the imperfect hall bar geometry in the measurement. Together with the sheet resistance  $R_{\text{sheet}}$ , the 2DEG density  $n$  determines the Drude mobility  $\mu = \sigma/en = 1/enR_{\text{sheet}}$ . Before LED illumination the longitudinal resistance  $R_{XX}$ , recorded in a 4 wire measurement setup to subtract ohmic contact resistances (I: ohmics o1, o8, V: ohmics o2, o7, see inset

of fig. 24), is  $R_{XX} = 45 \pm 17 \Omega$ . The rectangular geometry of the sample under study is well approximated by the sum of two adjacent squares. We therefore obtain a sheet resistance of  $R_{\text{sheet}} = 23 \pm 8 \Omega/\square$  and consequently a mobility of  $\mu = (2.8 \pm 1) \cdot 10^6 \text{ Vs/cm}^2$  before LED illumination, consistent with [123].

For the red trace in fig. 25 the LED was only partially flashed (after full illumination the wire DW pinch off shifts from  $-3.6 \text{ V}$  to  $-4.5 \text{ V}$ ). In order to obtain at least a lower limit on the mobility in that case, we use the larger density  $n = 1.91 \cdot 10^{11} \text{ cm}^{-2}$  for the case of saturated LED illumination to compute  $\mu$ . Using  $R_{\text{sheet}} = 4.3 \pm 1.5 \Omega/\square$  we obtain  $\mu = (7.6 \pm 2.6) \cdot 10^6 \text{ Vs/cm}^2$  after the LED flash.

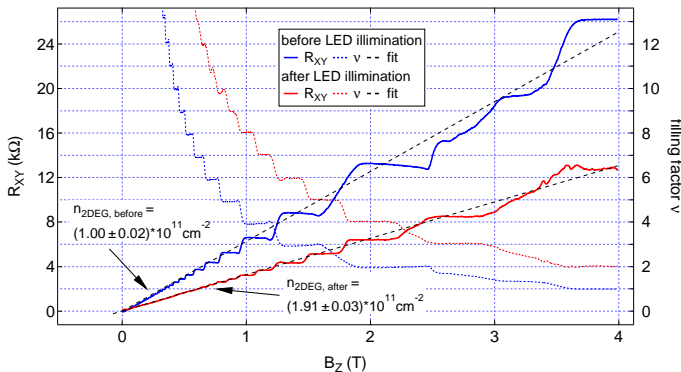


Figure 25: Longitudinal resistance  $R_{XY}$  as a function of perpendicular (to the 2DEG) magnetic field  $B_z$ . Blue and red traces represent measurements before and after LED illumination. Filling factors  $\nu = h/e^2 R_{XY}$  are drawn as dashed lines. The indicated 2DEG electron densities (and errors) are obtained from linear curve fits to the measured hall resistance  $R_{XY}$  in the low  $B$ -field regime. For clarity, the linear fits (black dashed traces) are drawn for the entire  $B$ -field range. No corrections were done to account for the imperfect hall bar geometry.

We note that the large error bars result from the voltage biased 4 wire measurement. At zero gate voltage (electron transport through the whole 2DEG) only a small fraction of the applied few  $\mu\text{V}$  AC excitation drops across the 2DEG (few tens of nV) which is difficult to measure and results in large uncertainties for the voltage measurement. Obviously, this could be easily circumvented with a current biased measurement. How-

ever, at negative gate voltage when current transport takes place only via the edge channels this would lead to a large voltage drop across the system. Therefore the 4 wire measurement setup with voltage bias is more suitable for transport measurements with these quantum wires.

#### 4.4.3 Disentangling lower and upper wire modes

As mentioned previously, the present sample hosts a 2DEG and two edge channels at the cleaved sample side. Whereas the upper channel (wire) is well coupled to the 2DEG states, the lower wire is separated by a 300 meV tunnelbarrier from the upper channel (and even more from the 2DEG). For the upper wire (UW) we therefore expect conductance steps in units of  $2e^2/h$  [111], apart from the conductance reduction observed by Yacoby *et al.* We note that the criterion of adiabatic contacts, a necessary ingredient for conductance quantization, is automatically given in typical GaAs samples with  $\lambda_F \sim 50$  nm and a separation of  $> 100$  nm between 2DEG and top gate structures i.e. potential variations are smooth at the depth of the 2DEG compared to  $\lambda_F$  (especially for the CEO wire samples used in this thesis where the 2DEG lies 500 nm below the surface). The situation is different for the lower wire (LW). The additional tunnel process introduces a transmission factor  $T < 1$  that reduces the conductance through the LW-system from  $g_{LW}$  down to  $T \cdot g_{LW}$ . This transmission factor depends on experimental details and varies e.g. for different combinations of upper and lower wire modes  $UW_i$  and  $LW_k$  which possess different wave function overlap. For  $LW_1$ , the first mode in the lower wire, tunneling is quite strong in our case with  $g = 0.3e^2/h$  after LED illumination and even  $g = 0.8e^2/h$  before illumination (fig. 24). The large tunnel conductance, however, is a result of the coupling between upper and lower edge channel taking place over an extended distance  $L$  much larger than the top gated region. Within the length of the double wires ( $L = 2 \mu\text{m}$ ) tunnel coupling is quite weak and UW, LW can be viewed as independent conductors. This was confirmed through reduction of the coupling length by means of neighboring top gates (not shown). In order to do so, the DW-system was completely pinched off with a neighboring gate such that current is

only injected through a  $6\ \mu\text{m}$  wide section of the 2DEG in between top gates. For such a reduced injection region we measure a tunneling step height of  $0.08\ e^2/h$ . A tunneling step of  $0.02\ e^2/h$  was measured for a  $2\ \mu\text{m}$  long injection region in [8] on nominally identical CEO double quantum wires.

To clearly distinguish between upper and lower wire modes we perform conductance measurements in a parallel magnetic field  $B_x$  applied along the axis of the wires (fig. 26). While not much is expected to happen to UW modes at moderate B-fields (due to a large wave function overlap with the 2DEG states), reshaping of the wave function drastically affects the tunneling process, thus changing the conductance through the LW. This can be seen when recording  $g(B)$  at fixed gate voltage  $g_5$  set such that only  $\text{LW}_1$  is transmitted underneath the gate, see inset of fig. 26 (gate position  $g_5$  is indicated by the black arrow in the main graph).

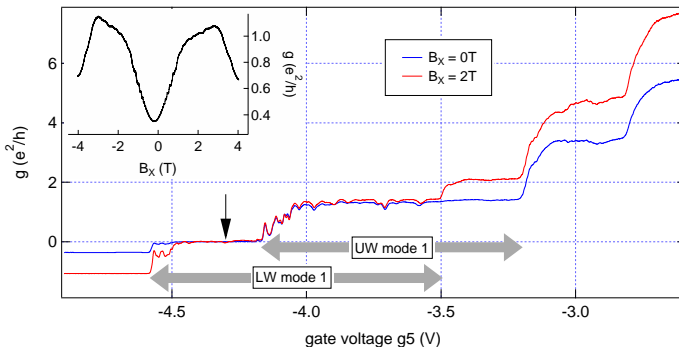


Figure 26: Conductance as a function of top gate voltage  $g_5$ , measured at  $T=560\ \text{mK}$  and zero external magnetic field (blue trace). For the red trace an external B-field of  $B_x = 2\ \text{T}$  is applied along the wires. Both traces are vertically shifted to align  $g = 0$  with the first conductance step. Fat gray arrows indicate the gate voltage range where only the lowest mode is available in the upper (lower) wire. The inset shows a B-field scan at fixed gate position, indicated by the black arrow in the main graph.

A gate scan for an external parallel B-field of 2 T (red trace) is shown in the main graph along with a conductance trace recorded without external B-field applied (blue trace). To emphasize the big effect on the LW conductance and the small effect on

the UW conductance at the same time, traces were shifted such that  $g(\text{LW}_1) = 0$ . The conductance step size of  $\text{LW}_1$ , which can now be read off in the pinch off regime, increases from  $\approx 0.3e^2/h$  at zero magnetic field to  $\approx 1e^2/h$  for  $B_x = 2\text{ T}$ .

The next conductance step, starting at  $g_5 \approx -4\text{ V}$ , is only slightly affected by the parallel magnetic field and is therefore attributed to an upper wire mode ( $\text{UW}_1$ ). At less negative top gate voltage around  $-3.5\text{ V}$ , the magnetic field reveals a clear conductance step that is barely visible at zero field. Due to the strong B-field dependence this step is identified as the second conductance step of the lower wire ( $\text{LW}_2$ ). The gate voltage range where only one mode is present in the lower (upper) wire, i.e. the system is truly in the Luttinger liquid state, is indicated in fig. 26 with light gray arrows.

#### 4.4.4 Ballistic addition of wires

The special CEO wire fabrication process presented in sec. 4.4.1, allows for the production of high quality quantum wires with a backscattering mean free path  $l_{BS}$  as large as  $20\text{ }\mu\text{m}$  [127]. Since  $l_{BS}$  clearly exceeds the length  $L = 2\text{ }\mu\text{m}$  of the CEO wires under study, electron transport through them is expected to be ballistic. This means that the measured conductance for such a quantum wire arises only from coupling into and out of the 1D modes. The resistance within the wire is essentially zero, i.e. all applied voltage drops across the wire contacts. Ballistic transport in CEO wires was demonstrated by Picciotto *et al.* [10] in 2001. In order to do so, three adjacent, closely spaced quantum wires were tuned to the single mode regime. In the diffusive limit the resistance of the combined system (three wires in series) is simply given by the sum of resistances, i.e. three times the resistance of a single wire. This is because in the diffusive limit scattering causes electrons to couple into and out of each wire separately. In the ballistic limit, however, when only coupling into the first and out of the last wire is required, the conductance is the same for one wire or three series (if the spacing between adjacent gates is much smaller than the 2D-1D coupling length [127]). In [10], instead of measuring the resistance of three wires in series, it was shown that there is only a negligible voltage drop across the middle wire, consistent with the

assumption of ballistic transport in these wires.

In the following, the situation is investigated for the present DW samples. We slightly modify the measurement scheme from ref.[10], and record the conductance as a function of two neighboring gates instead of using three adjacent top gates. The sample schematic in fig.27(a) (front view) shows a zoom in for two adjacent double wires (dark blue) and corresponding top gates (yellow). Schematic conductance traces  $g_{\text{DW}3}$ ,  $g_{\text{DW}4}$  for the two neighboring double wires DW3 and DW4 are plotted in fig. 27(b) as a function of their respective gates  $g_3$  and  $g_4$ .

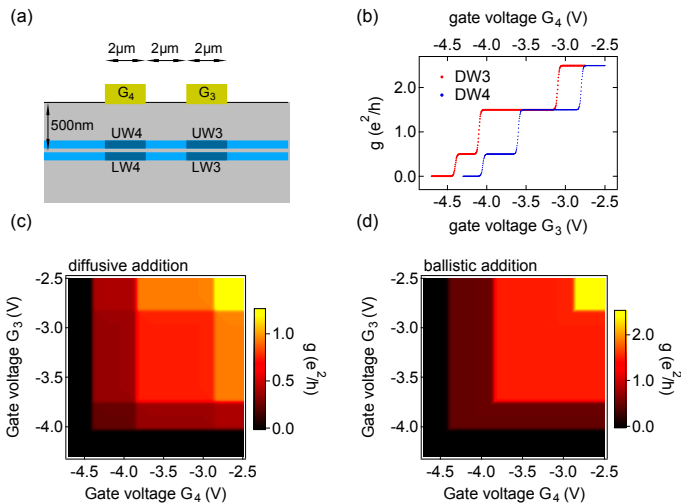


Figure 27: (a) Sample schematic showing two adjacent gates (yellow). The corresponding upper and lower wires (dark blue) are part of the 1D channels that extend along the entire sample edge (light blue). Geometric dimensions are indicated. (b) Simulated conductance trace for DW3 (DW4) versus gate voltage  $g_3$  ( $g_4$ ) (c) Calculated conductance of the combined DW system in the diffusive limit where series resistors simply add up. (d) Same as (c) but in the ballistic limit. Here the wire  $i$  with the lower conductance limits the total transmission

We assume that each double wire system  $\text{DW}i$  can be modeled as a pair of independent parallel resistors  $R_{\text{UW}i}$  and  $R_{\text{LW}i}$ . For classical resistors (equivalent to the diffusive

limit) the total conductance  $g_{tot}$  of the combined DW system in fig. 27(a) can easily be calculated. In units of  $e^2/h$  the conductance  $g_{tot}$  reads:

$$g_{tot} = \frac{h}{e^2} \left( \left( \frac{1}{R_{UW3}} + \frac{1}{R_{LW3}} \right)^{-1} + \left( \frac{1}{R_{UW4}} + \frac{1}{R_{LW4}} \right)^{-1} \right)^{-1} \quad (17)$$

Fig. 27(c) shows  $g_{tot}$  for the schematic DW traces in fig. 27(b), calculated using eq. 17. The resulting checkerboard pattern reflects the fact that changing the value of any resistor in the diffusive case changes the total resistance of the system.

For the ballistic limit we assume that e.g. right moving electrons in fig. 27(a) can only be backscattered upon coupling into UW4 (LW4) on the left hand side and upon coupling out of UW3 (LW3) on the right hand side. In other words the combined DW system in fig. 27(a) can be viewed as a single  $6 \mu\text{m}$  long double wire, composed of DW4, DW3 and the  $2 \mu\text{m}$  long ungated section in between.

The conductance  $g_{tot}$  of the  $6 \mu\text{m}$  long combined system is given by:

$$g_{tot} = \frac{h}{e^2} \left( \frac{1}{\max(R_{UW4}, R_{UW3})} + \frac{1}{\max(R_{LW4}, R_{LW3})} \right) \quad (18)$$

As for the diffusive case, we plot  $g_{tot}$  for the schematic DW traces given in fig. 27(b), see panel (d). In contrast to the checkerboard pattern, a L-shaped structure appears for the ballistic addition of conductors. A four wire conductance measurement of the conductance as a function of  $g_3$ ,  $g_4$  is shown in fig. 28.

The close match of measured L-shaped pattern in fig. 28 and the simulated conductance of the combined DW system in fig. 28(d) shows that the  $2 \mu\text{m}$  long CEO wires add like ballistic conductors. Indeed, a careful inspection of individual traces (see fig. 37 in sec. 4.5.2) confirms ballistic transport with small deviations. More precisely, the average conductance  $\langle g_{UW1} \rangle$  as a function of  $g_3$  (in the gate voltage range indicated by the black rectangle in fig. 37) for two quantum wires in series (neighboring DW2 tuned to its first UW mode) is only slightly smaller than the conductance recorded for DW3 without neighboring gates activated. The conductance for the combined DW system (separated by a  $2 \mu\text{m}$  long ungated section) reaches  $95 \pm 3\%$  of the individual DW conductance,

in good agreement with [127] where a 6% reduction was found for the combined DW system.

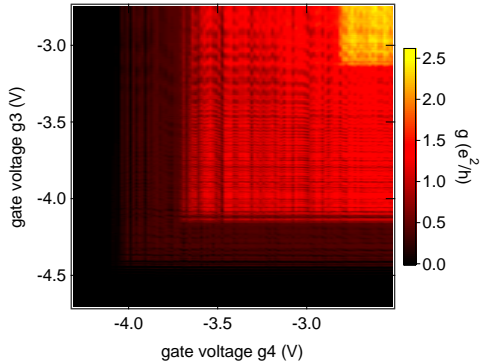


Figure 28: Measured conductance  $g$  as a function of top gate voltage  $g_3$  and  $g_4$ . The two neighboring,  $2\ \mu\text{m}$  wide gates are separated  $2\ \mu\text{m}$  in distance. The observation of a L-shaped pattern rather than a checkerboard pattern for the combined system indicates ballistic addition of the two subsystems.

#### 4.4.5 Electron localization in the pinch off regime

As the top gate voltage is lowered, the electron density  $n$  beneath the gate is continuously reduced for both, upper and lower wire. Below a critical density  $n \approx 20\ \mu\text{m}^{-1}$  the Fermi energy is small enough ( $E_F = \hbar^2 n^2 \pi^2 / 8m \approx 0.5 - 1\ \text{meV}$  depending on the value of  $K_c$ ) for electron transport through the CEO wires to be dominated by the local disorder potential. As a consequence, electrons start to form localized states in between the highest barriers of the disorder potential. Sharp conductance peaks in the pinch off regime of the CEO wire, as seen in fig. 29, indicate the transition to electron localization in the quantum wire as previously observed by O. Auslaender, H. Steinberg and others [8, 9, 102].



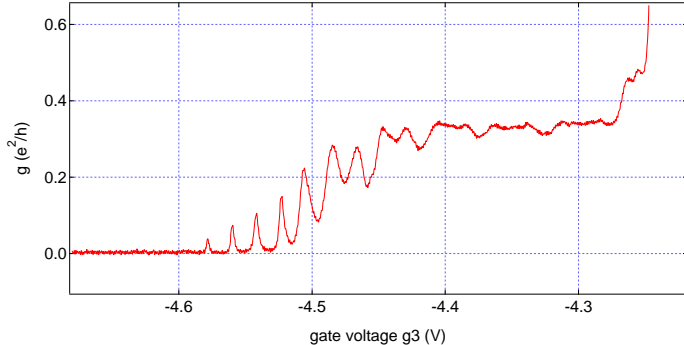


Figure 29: CEO wire conductance as a function of top gate voltage  $g_3$ . At sufficiently low electron density (in the pinch off regime) the system starts to localize. As a consequence, coulomb blockade peaks dominate the transport properties of the CEO wires.

Further verification comes from conductance measurements as a function of gate voltage  $g_3$  and source-drain bias  $V_{SD}$ . We observe the very familiar coulomb diamond pattern, see fig.30(a). The charging energy  $E_C$  for the six visible diamonds increases with decreasing gate voltage  $g_3$  and ranges from  $\approx 0.75$  mV up to  $\approx 1.5$  mV. In addition to the bare coulomb diamonds, excited states can be seen in fig.30(a) with energies ranging from  $\approx 0.5$  meV to 1 meV. A naive comparison of the QD to a "particle in a box" with a ground state energy  $E_1 = \hbar^2 \pi^2 / 2mL^2$  allows for a rough guess of the QD size. For an excited state energy of  $0.5 - 1$  meV we end up with a quantum dot length of  $L = 75 - 105$  nm.

We will now extract the gate capacitance  $C_g$  to the quantum dot by analyzing the separation of coulomb blockade peaks at zero bias (black circles in fig.30(a)). In order to do so, we plot the  $V_{SD} = 0$  conductance peak positions from fig.30(a) (black circles) versus the electron number  $N$  in the QD (black dots in fig.30(b)).

Since the charge on the QD changes by one electron between peaks, the slope of the data determines the gate capacitance,  $C_g = e/\Delta V_g$ . A linear fit (red) to the data yields  $C_g = 8.9$  aF, see fig.30(b).

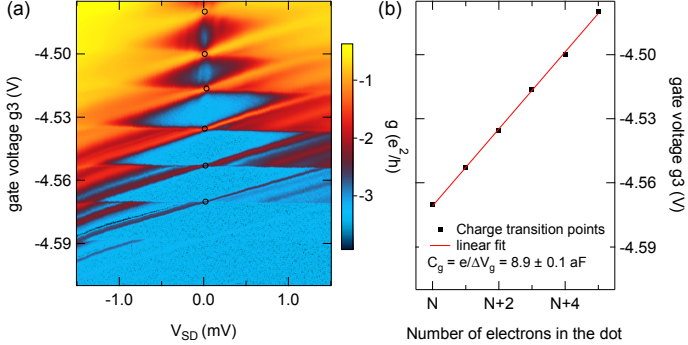


Figure 30: (a) Logarithm of the conductance  $g$  as a function of source-drain bias  $V_{SD}$  and top gate voltage  $g3$  in the pinch off regime of the double wire system. The stability diagram shows single quantum-dot behavior with clear coulomb blockade diamonds. (b) Charge transition points (black circles in (a)) versus electron number  $N$  in the quantum dot (black data points). The top gate capacitance  $C_g = 8.9 \pm 0.1$  aF is extracted from a linear fit (red trace) to the data.

For a known QD size  $L$  the gate capacitance  $C_g$  can also be calculated. In the case of two infinitely long, parallel cylinders with radii  $R_a$ ,  $R_b$  and separation  $d'$ , the capacitance per length  $C/L$  reads [128]:

$$\frac{C}{L} = \frac{2\pi\epsilon_0\epsilon_r}{\operatorname{arccosh}\left(\frac{d'^2 - R_a^2 - R_b^2}{2R_a R_b}\right)} \quad (19)$$

This geometry can easily be adapted to the present case of a cylinder and a parallel plane (top gate) with separation  $d$ . We redefine:  $d' \rightarrow d' + \Delta x$ ,  $R_b \rightarrow R_b + \Delta x$ , take the limit  $\Delta x \rightarrow \infty$  and replace  $d = (d' - R_b)$ . The resulting capacitance per length for a cylinder of radius  $R_a$  at a distance  $d$  from a "semi-infinite" plane (top gate only extends up to the cleaved edge) is given by:

$$\frac{C}{L} = \frac{\pi\epsilon_0\epsilon_r}{\operatorname{arccosh}\left(\frac{d}{R_a}\right)} \quad (20)$$

Using the previous estimate for the QD length  $L = 75 - 105$  nm,  $\epsilon_r = 12.9$  for GaAs

and  $d = 541$  nm,  $R_a = 15$  nm for the lower wire where the QD forms, we obtain  $C_g = 6.3 - 8.9$  aF. The calculated  $C_g$  is in good agreement with the measured  $C_g = 8.9$  aF which seems to support the rough guess of the QD size.

In principle the total gate capacitance  $C_{UW}$ ,  $C_{LW}$  to upper and lower wire can also be calculated with eq. 20. For  $2\mu\text{m}$  long double wires we obtain:

$$\begin{aligned} \text{UW :} & \quad d = 510 \text{ nm} ; R_{UW} = 10 \text{ nm} \quad \Rightarrow \quad C_{UW} = 155 \text{ aF} \\ \text{LW :} & \quad d = 541 \text{ nm} ; R_{LW} = 15 \text{ nm} \quad \Rightarrow \quad C_{LW} = 168 \text{ aF} \end{aligned} \quad (21)$$

There are, however, two problems with this simple capacitance calculation. Eq. 20 assumes cylinder (wire) and plane (top gate) to be translational invariant along the axis of the cylinder. For the quantum dot being much smaller than the wire length, this situation is probably satisfied (unless it forms at one end of the wire by chance). For the wires, however, eq. 20 overestimates the capacitance.

Much more important than this finite size effect is screening of e.g. LW modes by UW modes, but also within the same wire (e.g. screening of  $UW_1$  by  $UW_2$ ). The only situation where screening is absent and eq. 20 is expected to apply (apart from the finite size overestimation) is when only one mode is present in the lower wire.

Calculations including screening would be extremely complicated to do since they require precise knowledge of the wave function for each participating mode. Experimentally, the density may be determined independently for each mode by means of spectroscopy [8, 85, 92] which will be discussed in the following section.

#### 4.4.6 Electron density of upper and lower wire modes

The dispersion for 1D-systems reduces to a simple parabola with two Fermi points located at  $\pm k_F$ . Fig. 31(a) schematically depicts the dispersions at zero magnetic field for a double wire system with  $n_{UW} < n_{LW}$ . The four corresponding Fermi points are indicated as black circles.

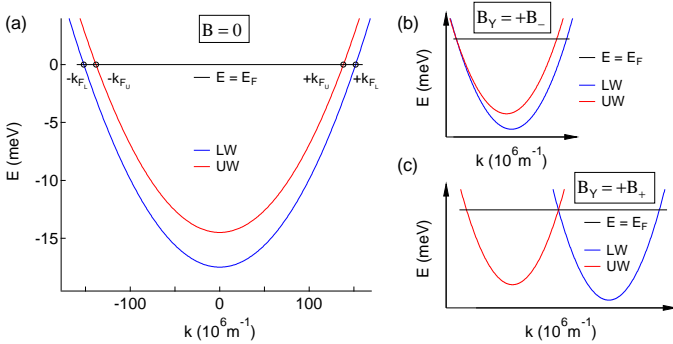


Figure 31: (a) Sketch of the dispersions in a DW system with  $n_{LW} > n_{UW}$  at zero magnetic field. The situation is depicted for a rescaled (due to interactions) effective electron mass  $m_{e,\text{GaAs}} \rightarrow 0.75 \cdot m_{e,\text{GaAs}}$ , though in presence of interactions the dispersions might not be parabolic anymore. Black circles indicate the four Fermi points, the Fermi energy is shown as black line. (b) Resonant tunneling between left movers in upper and lower wire at a magnetic field  $B = +B_-$ , applied perpendicular to the plane spanned by the DW-system. (c) Resonant tunneling between UW right movers and LW left movers at  $B = +B_+$ .

Due to translational invariance of the DW-system momentum is a conserved quantity for electrons tunneling between the wires [129]. Since none of the UW Fermi points overlaps with any of the LW Fermi points, tunneling to the LW is suppressed at  $B = 0$ . In presence of an external magnetic field  $B_y$ , applied perpendicular to the plane defined by the DW system (parallel to the 2DEG), electrons acquire a momentum kick  $\Delta p = \hbar \Delta k$  upon tunneling to the lower wire. For a separation  $d$  between UW and LW,  $\Delta p$  is given by [8, 85]:

$$\frac{\Delta p}{\Delta t} = F_{\text{Lorentz}} = evB_y = e \frac{\Delta s}{\Delta t} B_y \Rightarrow \Delta k = \frac{-|e|d \cdot B_y}{\hbar} \quad (22)$$

At  $B_y = +B_-$ , the acquired momentum kick exactly compensates for the mismatch in Fermi wave vectors between left movers  $B_- = \hbar(k_{F_U} - k_{F_L}) / |e|d$  and tunneling to the LW is resonant, see fig. 31(b). When increasing the B-field further, the resonance condition is no longer met and tunneling is again suppressed. This persists until the  $B = +B_+$  point is reached (fig. 31(c)) where resonant tunneling between UW right

movers and LW left movers takes place i.e. the acquired momentum kick is equal to the sum of Fermi wave vectors  $B_+ = \hbar(k_{FU} + k_{FL}) / |e|d$ . For a given pair of resonance points  $\{B_-^{ij}, B_+^{ij}\}$  corresponding to tunneling between UW mode  $i$  and LW mode  $j$ , the densities  $n_{UW_i}$  and  $n_{LW_j}$  are simply given by:

$$n_{UW_i} = \frac{2|e|d(B_+^{ij} - B_-^{ij})}{h} ; \quad n_{LW_j} = \frac{2|e|d(B_+^{ij} + B_-^{ij})}{h} \quad (23)$$

In practice we use three top gates,  $g3$  and its adjacent gates  $g4$  and  $g2$  to achieve suitable conditions for spectroscopy measurements on DW3. The situation is schematically depicted in fig.32. Gate  $g4$  is set to large negative voltage such that the underlying 2DEG and DW4 are pinched off. A small source-drain bias  $V_{SD} = 100 \mu\text{V}$  is applied to ohmic contact  $o4$  (contacts the 2DEG in the ungated section in between  $g3$  and  $g4$ ) to overcome the suppression of tunneling into a LL at zero bias. The current is drained at ohmic contact  $o1$  by means of an IV-converter. To make sure that only tunneling current is measured,  $g2$  is set to the first mode of its corresponding lower wire.

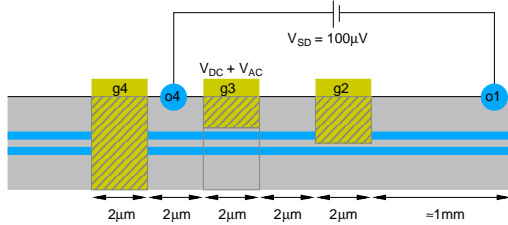


Figure 32: Gating scheme as used for tunnel spectroscopy measurements in fig. 33. Gate  $g4$  pinches the DW completely and  $g3$  transmits only the lowest mode of the LW. The differential tunneling current  $dI_T/dV_{g3}$  with respect to top gate  $g3$  is measured at  $o1$ . A small source drain bias  $V_{SD} = 100 \mu\text{V}$  is applied to the short tunnel junction to overcome the zero bias suppression of tunneling into a Luttinger liquid.

We note that the small source-drain bias induces a negligible but finite bandshift between the parallel wires (and even smaller bandfilling [130] effects). A much more important effect is magnetic depopulation of 1D subbands [131]. The magnetic field  $B_y$  introduces an additional confinement which increases the electron effective mass,

$m^* \rightarrow m^*(B_y)$ . As a consequence, lower modes are populated at the expense of higher ones. For the lowest mode in the present wires this only leads to a slight overestimation (below 5%) of the electron density. However, since precise correction for the magnetic confinement is very difficult in case of the CEO wires (triangular confinement with nonuniform level spacing), this effect was neglected for all extracted wire densities presented in this thesis.

In order to be more sensitive to electrons tunneling to the LW underneath  $g3$  where the electron density is varied through the top gate (instead of tunneling in between gates  $g4$  and  $g3$ ) and following Auslaender [8],  $g3$  is modulated with few mV AC-excitation and the differential tunneling current  $dI_T/dV_{g3}$  is measured at  $\phi 1$ . Fig. 33(b) shows such a differential tunneling current measurement as a function of  $g3$  and  $B_y$ , recorded in the gate configuration depicted in fig. 32. As the gate voltage  $g3$  is lowered, the density in UW and LW decreases, and consequently  $B_+^{ij}$  resonances (given by sum of densities in  $UW_i$  and  $LW_j$ ) move to smaller  $B_y$ . In contrast,  $B_-^{ij}$  resonances shift to larger  $B_y$  since UW modes depopulate faster than LW modes (UW screens LW), and therefore the density difference grows with decreasing gate voltage. Several pairs of  $\{B_+, B_-\}$  branches are visible in fig. 33(b). Red and blue dots indicate the pair of resonances  $\{B_+^1, B_-^1\}$  corresponding to tunneling between the lowest modes of upper and lower wire.

It turns out that the moderate AC-excitation on gate  $g3$  also induces a small modulation in the neighboring 2DEG. Therefore, in addition to the gated section, the Lockin measurement is also sensitive to electrons tunneling in the ungated section. In other words electrons from the UW can either tunnel to the LW in the ungated section, i.e. in between gates  $g3, g4$  (see fig. 32), or they tunnel from the UW section underneath  $g3$  where density is changed by the top gate. Black arrows indicate  $B_+, B_-$  resonances that arise from electrons tunneling to the LW in the ungated section. Since ideally the density in the ungated section is not affected by top gates, these resonances appear as (almost) horizontal lines in fig. 33.

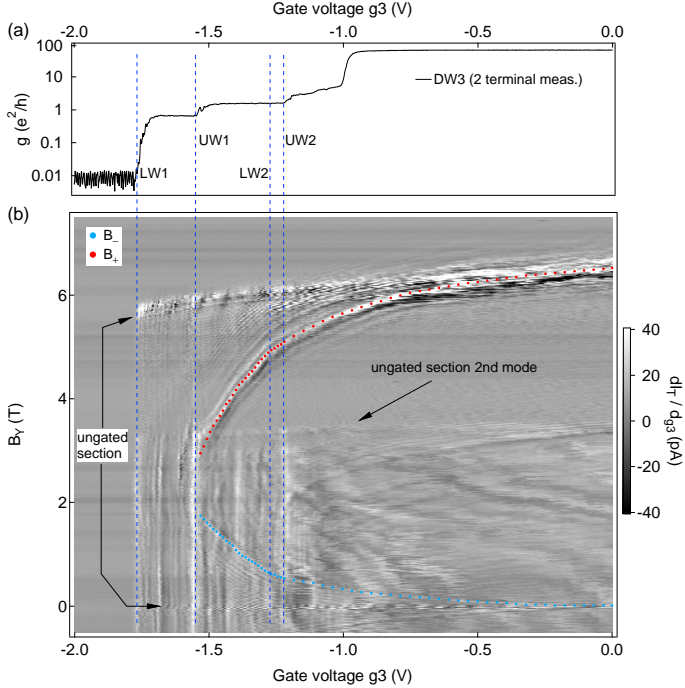


Figure 33: (a) 2 terminal conductance trace for DW3. Vertical blue dashed lines indicate gate voltages where modes  $LW_2$ ,  $LW_1$ ,  $UW_2$  and  $UW_1$  pinch off. (b) Differential trans tunneling current as a function of perpendicular magnetic field  $B_y$  ( $\perp$  to the plane spanned by the DW system) and gate voltage  $g_3$ , measured in the configuration shown in fig. 32. Blue and red dots indicate the resonance condition for co- and counter-propagating electrons in the lowest upper and lower wire modes (gated section). Arrows indicate the same resonance condition for electrons tunneling in the ungated section in between gates  $g_4$  and  $g_3$ .

This identification is supported by the observation that horizontal lines extend up to the gate voltage where  $g_3$  depletes its LW and blocks current completely (compare with 2 terminal conductance measurement of DW3 in fig. 33(a)). For the gated section, the  $\{B_+^1, B_-^1\}$  resonances obviously only exist up the point where the upper wire is pinched off. In addition, at zero top gate voltage ( $g_3 = 0$ ), the resonance condition for gated and ungated section is the same since densities in both regions are identical. Therefore

upon approaching  $g_3 = 0$  resonances arising from electrons tunneling in the ungated and gated section start to merge (see fig. 33(b)).

In addition to  $\{B_+^1, B_-^1\}$  points, vertical resonance lines (no defined momentum) are observed in fig. 33(b). They are attributed to electron localization at low density in different modes (see sec. 4.4.5 for localization in  $LW_1$ ) and have previously been observed [8, 9].

We proceed to calculate the electron densities from the  $\{B_+^1, B_-^1\}$  branches in fig. 33(b) (red and blue points) using eq. 23. The results are presented in fig. 34, along with a two terminal conductance trace (black) for comparison.

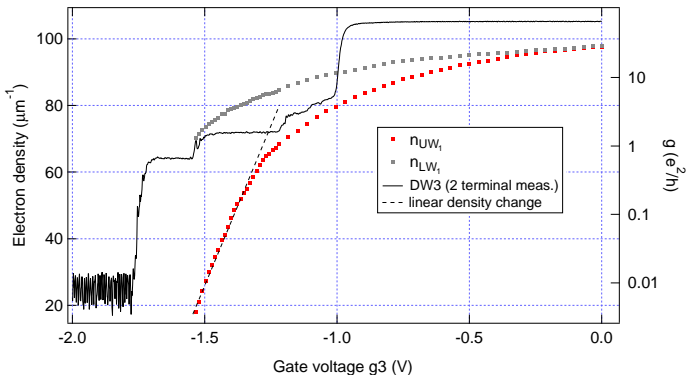


Figure 34: Electron density  $n_{UW_1}$  and  $n_{LW_1}$  for the lowest upper and lower wire mode as a function of top gate voltage  $g_3$ . Densities are calculated from the  $\{B_-^1, B_+^1\}$  resonances in fig. 33(b). A black dashed line indicates linear density change in the regime where the UW hosts only one mode. For comparison a two terminal conductance trace (black) for DW3 is shown along with the densities.

Initially, due to screening by higher modes (and the 2DEG), the densities  $n_{UW_1}$  and  $n_{LW_1}$  only change little upon lowering the top gate voltage  $g_3$ . As mentioned earlier, screening of the LW by the UW is responsible for  $n_{LW_1}$  to change slower as a function of  $g_3$ . Even though the density depends on  $g_3$  in a non trivial way, in the regime where only one mode is present in both wires, the capacitance  $C = \Delta Q / \Delta V_{g_3}$  is fairly constant (constant  $C$  is indicated as black dashed line) in agreement with simple capacitor mod-



els. If we assume that the same behavior applies for the lower wire in the regime where all UW modes have been depleted and furthermore that the LW localizes at similar densities as the UW, the capacitance  $C_{LW}$  in the unscreened region can be calculated. We therefore assume that the density  $n_{LW_1}$  drops from  $\approx 70 \mu\text{m}^{-1}$  (last data point for  $n_{LW_1}$  in fig. 34) to  $\approx 20 \mu\text{m}^{-1}$  within a gate range of 150 mV, see conductance trace in fig. 34 or fig. 29. The resulting capacitance  $C_{LW} = \Delta Q / \Delta V_{g3} = 107 \text{ aF}$  is roughly one third smaller than the previously (theoretically) calculated lower wire capacitance of  $C_{LW, \text{theory}} = 168 \text{ aF}$  (see eq. 20 in sec. 4.4.5). Considering that the calculation slightly over estimates  $C_{LW}$  due to the finiteness of the system, measured and calculated capacitance agree quite well.

All measurements in this section were performed after partial (weak) LED illumination. This can be seen from the much lower voltage needed to pinch off the DW-system in fig. 34 ( $g3 \approx -1.8 \text{ V}$ ) compared to the measurements shown in sec. 4.4.5 (pinch off at  $\approx -4.5 \text{ V}$  in fig. 29). One might mistake this drastic change in pinch off voltage as a sign for a significant change in the electron densities  $n_{UW_1}$  and  $n_{LW_1}$ . Unfortunately, at present, no spectroscopy measurements are available for DW3 after strong LED illumination. Measurements on DW5 and DW6 after strong LED illumination, however, show that though their pinch off voltage significantly differs ( $g5_{\text{pinch}} \approx -4.6 \text{ V}$ ,  $g6_{\text{pinch}} \approx -4.1 \text{ V}$ ) the densities  $n_{UW_1}$  and  $n_{LW_1}$  are very similar for corresponding gate voltages (e.g. when  $UW_1$  starts to localize in either DW5 or DW6). Consequently, similar densities would be assumed for DW3 after strong LED illumination. In addition, the ungated densities  $n_{UW_1} = 102.5 \mu\text{m}^{-1}$  and  $n_{LW_1} = 100.7 \mu\text{m}^{-1}$  for DW5 after strong LED illumination are only slightly larger (less than 5%) than the densities presented in fig. 34 for  $g3 = 0$ . It seems that little LED illumination is sufficient to saturate the densities  $n_{UW_1}$  and  $n_{LW_1}$  for the lowest modes. However, more modes are populated after illumination, resulting in an overall much higher electron density (factor 2-3) in the wires after strong LED illumination which is responsible for larger pinch off gate voltages.

## 4.5 CEO wires as 1D electronic Fabry-Perot resonators

### 4.5.1 Fabry-Perot resonances in the tunneling current

A closer look at the low B-field regime in the tunnel spectroscopy measurement (fig. 33) reveals a clear checkerboard pattern. The periodicity of the pattern changes as a function of gate voltage from slow oscillations around  $g3 = 0$  to fast oscillations in the regime where only the lowest mode in the upper wire is present (see fig. 35(a)). This becomes even more clear when looking at single cuts for a fixed magnetic field as shown in fig. 35(b). Since the checkerboard pattern is only visible around  $B = 0$ , we attribute the signal to electrons tunneling in the ungated section (compare with scheme in fig. 32 and discussion in the previous section).

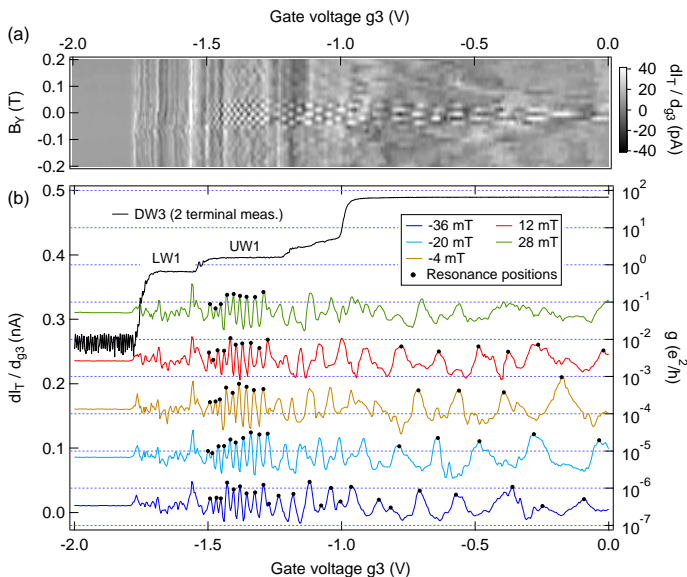


Figure 35: (a) Differential tunneling current  $dI_T/dV_{g3}$  as a function of top gate voltage  $g3$  in the low B-field regime (zoom in from fig. 33(b)). (b) Line cuts from (a) for different  $B_y$  as indicated. For clarity traces are offset by 75 pA. Black dots mark resonance peaks that are used for further analysis. To visualize the changing oscillation period in relation to the DW configuration, a two terminal conductance trace (black) is shown in addition.

The question arises how the top gate  $g_3$  would create such oscillations if we assume that the ungated section is only affected very little by  $g_3$ . We assume that coupling from the multi mode to the single mode regime (ungated versus gated section) is not perfect. Hence, we may have scattering at the left and right boundaries of gates  $g_3$  and  $g_2$ . This can lead to multiple reflections e.g. inside the gated section beneath  $g_2$  or  $g_3$ . Given the densities in different sections, it is possible to determine whether or not multiple scattering paths interfere constructively. For the measurement in fig. 35 only the top gate  $g_3$  is varied, and hence multiple reflections e.g. within  $LW_2$  ( $UW$  is pinched off below  $g_2$ ) will only contribute a fixed transmission factor to the measured tunneling current. Therefore the observed oscillations in fig. 35 as a function of  $g_3$  are attributed to Fabry-Perot resonances within  $DW_3$ , more precisely within the  $LW$  of  $DW_3$  (electrons tunnel in the ungated section in between  $g_4$  and  $g_3$ ).

In optics such resonances are very well known. Consider a pair of parallel mirrors with reflectance  $R$  and a filling material with refractive index  $n_{med}$  in between. The wavelength  $\lambda_{med}$  in between the mirrors is reduced from the bare vacuum wavelength  $\lambda_0$  by the refractive index, i.e.  $\lambda_{med} = \lambda_0/n_{med}$ . For an incident light beam hitting the parallel mirrors under normal incidence, the intensity  $I_{out}$  of the out-coming light oscillates as a function of  $\lambda_{med}$ :

$$\frac{I_{out}}{I_{in}} = \frac{(1 - R)^2}{1 + R^2 - 2R \cos\left(\frac{2\pi}{\lambda_{med}} 2L\right)} \quad (24)$$

In case of an electronic 1D-system, where electron density and wavelength are related by  $2\pi/\lambda = n\pi/2$ , the Fabry-Perot oscillations appear as a function of density  $n$  in the wire:

$$\frac{I_{out}}{I_{in}} = \frac{(1 - R)^2}{1 + R^2 - 2R \cos(\pi Ln)} \quad (25)$$

For  $L = 2 \mu\text{m}$  the argument of the cosine changes by  $2\pi$  whenever the density  $n_{LW_1}$  for  $DW_3$  changes by  $10^6 \text{ m}^{-1}$ . In other words, one full oscillation in fig. 35 corresponds to the addition of two electrons to the first lower wire mode in  $DW_3$ .

In order to verify these statements, we proceed to count the oscillations in the checkerboard pattern of fig. 35(a) and try to reconstruct the density  $n_{LW_1}$  as a function of top gate voltage  $g_3$ . For all cuts in fig 35(b) oscillation peaks can clearly be assigned (black dots) in the regime where only one mode is present in the UW. Since the LW already contains a significant amount of electrons at the position of the first assigned peak (at  $g_3 \approx -1.5$  V), counting subsequent peaks will only allow to calculate the electron density  $n_{LW_1}$  up to a constant. For all B-field cuts, we assign a density of  $74.5 \mu\text{m}^{-1}$  to the first peak (as obtained from spectroscopy measurements), thus fixing the offset. For every further peak, the density is increased by  $1 \mu\text{m}^{-1}$ . For the dark blue trace in fig. 35 oscillation peaks were assigned up zero gate voltage. However, maybe not every identified resonance in fig. 35(b) is completely obvious. Therefore this procedure is broken up into two sequences where the identification of peaks seems more clear for the  $-20 \text{ mT} / -4 \text{ mT} / 12 \text{ mT}$  traces. For the low gate voltage range ( $g_3 > -0.8$  V) a new density offset  $n_{\text{offs}}$  may be chosen ( $n_{\text{offs}} = (74.5 + m) \mu\text{m}^{-1}$  with  $m \in \mathbb{N}$ ) to match the reconstructed density with the spectroscopic data.

Fig. 36 shows the lower wire density  $n_{LW_1}$  as a function of top gate voltage  $g_3$ , extracted from the spectroscopy measurements in fig. 33. Superimposed are reconstructed densities (plus constant offset) calculated by counting oscillations in the B-field cuts from fig. 35(b). For all B-field cuts, the reconstructed lower wire density are in excellent agreement with the lower wire density  $LW_1$  obtained from spectroscopy measurements. Clearly, the reconstructed density does not match the upper wire density  $UW_1$ .

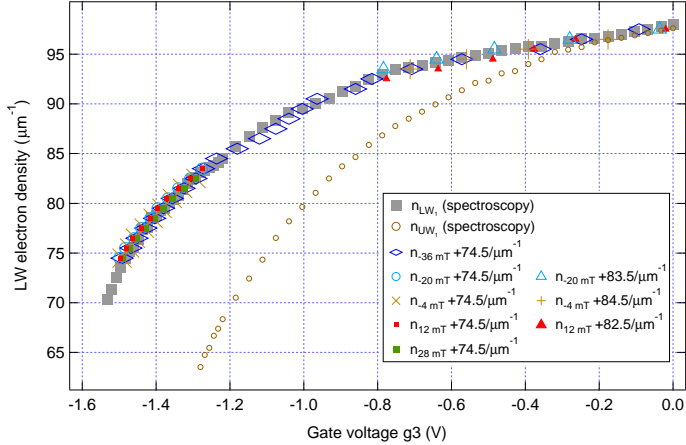


Figure 36: Reconstructed lower wire density  $n_{LW_1}$  (for DW3) by counting Fabry-Perot resonances (black dots) of corresponding cuts in fig. 35 and assigning a density change of  $1 \mu\text{m}^{-1}$  per oscillation. A fixed offset of  $74.5 \mu\text{m}^{-1}$  is added to the reconstructed densities for better comparison with the spectroscopically gained data (gray squares for lower and brown circles for the UW density). The small gate voltage range  $g_3 > -0.8$  V for the  $-20$  mT /  $-4$  mT /  $12$  mT traces was treated separately and therefore, as indicated, different offsets were assigned.

To complete the picture we return to the checkerboard pattern in fig. 35(a), this time with the focus on the B-field period. We notice that adjacent traces are phase shifted quite precisely by  $\pi$  (observed over  $\approx$  three periods in B-field direction  $\Leftrightarrow$  phase shift of  $6\pi$ ). Since neighboring traces are separated by  $16$  mT, we infer an oscillation period of  $32$  mT. Due to the low sampling rate (B-field resolution) possible oscillation periods are actually given by  $32/(2k + 1)$  mT with  $k \in \mathbb{N}_0$ . For oscillations in gate voltage direction we concluded that a density change of  $1 \mu\text{m}^{-1}$  (by changing the top gate  $g_3$ ) is required to accumulate a phase shift of  $2\pi$  over a distance of  $2L$ . Instead of changing  $g_3$ , we can also give the tunneling electron a momentum kick (during the tunneling process) that corresponds to the same density change and is small enough for UW and LW dispersions to still have a finite overlap. Using eq. 22 we calculate a B-field period  $\Delta B_y$  of:

$$B_y = \frac{\hbar \Delta k}{|e|d} = \frac{\hbar \Delta n \pi}{2|e|d} = 33.4 \text{ mT} \quad (26)$$

Though the B-field sampling rate is low, it still allows for a rough estimation of the period (32 mT) which agrees well with the 33.4 mT predicted for Fabry-Perot resonances. We would like to note that Aharonov Bohm resonances as observed e.g. in [85] for  $B_y$  versus  $V_{SD}$  spectroscopy measurements can be excluded since they would occur with double the period:  $\Delta B L d = h/e \Rightarrow \Delta B = 66.7 \text{ mT}$ . In conclusion, the density reconstruction in fig. 36 and the correctly predicted B-field period strongly support the interpretation of the checkerboard pattern as Fabry-Perot resonances.

#### 4.5.2 Fabry-Perot resonances in the upper quantum wire

The question naturally arises, whether or not Fabry-Perot resonances can also be observed for the upper wire. In sec. 4.4.4 where it was shown that two adjacent double wires add like ballistic resistors, clear horizontal and vertical lines are seen in the conductance measurement versus top gate voltage  $g_3$  and  $g_4$  (no other gates activated), indicating the presence of such oscillations. Two line scans for fixed  $g_4$  are shown in fig. 37 as a function of gate  $g_3$ . While for the red trace  $g_4$  is only set to sufficiently negative voltage (-2 V) to deplete the underlying 2DEG,  $g_4$  is set to the first mode of the corresponding upper wire for the blue trace.

The inset shows a magnified view in the regime where only one mode in the UW is present. After shifting the traces horizontally by 4.9 mV, the two oscillation patterns agree very well, which shows that they are controlled by the scanning gate  $g_3$  only. Furthermore, for the blue trace where the total conductance is limited by gate  $g_4$  to one mode in the UW, these oscillations are clearly visible even in the regime where further (higher) modes in DW3 become available. While the oscillation period is fast (but roughly constant) in the regime where only one mode is available in UW and LW, it significantly increases with less negative gate voltage. This behavior seems similar to the observations made for the differential tunneling current to the LW in fig. 35 and therefore hints towards Farby Perot resonances as possible source for these oscillations.

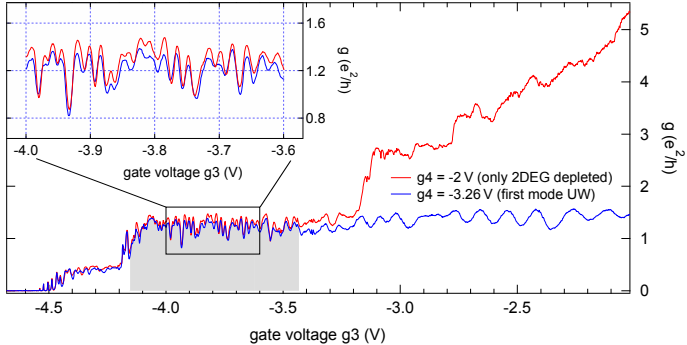


Figure 37: Conductance  $g$  as a function of top gate voltage  $g_3$ . For the red trace the neighboring gate  $g_4$  is set to  $-2$  V such that it depletes the underlying 2DEG. For the blue trace  $g_4$  is set to the lowest mode of the corresponding wire (compare with fig.28). The inset shows a zoom-in onto the pronounced conductance oscillations. For better visibility the traces in the inset have been shifted horizontally by  $4.9$  mV to match their patterns.

As mentioned earlier, no spectroscopy data is available for DW3 after strong LED illumination. After partial illumination, the density  $n_{UW_1}$  drops approximately by 40 electrons per micron (from  $60 \mu\text{m}^{-1}$  to  $20 \mu\text{m}^{-1}$ ) in the regime where only one mode in upper and lower wire are present. Within measurements uncertainties, the same values are obtained for DW5 and DW6 after full LED illumination. It seems to be a fair assumption that after full LED illumination the density  $n_{UW_1}$  in DW3 still drops by roughly  $40 \mu\text{m}^{-1}$  in that regime. The corresponding gate range from the point at which  $UW_1$  localizes ( $g_3 = -4.15$  V) until the second mode of the LW sets in ( $g_3 = -3.43$  V) measures  $\approx 720$  mV and is indicated as gray area in fig.37. For the Fabry-Perot resonances in the tunneling current to the LW we concluded that a density change by  $1 \mu\text{m}^{-1}$  in the LW of DW3 is required for one oscillation. This still holds for Fabry-Perot resonances in the UW of DW3 with the only difference that the oscillation period is controlled by the UW density  $n_{UW_1}$  instead of  $n_{LW_1}$ . We therefore expect one oscillation per 18 mV ( $720 \text{ mV} / 40$ ) in the regime where the density  $n_{UW_1}$  changes linearly with gate voltage  $g_3$  (until  $LW_2$  sets in). Within the 400 mV wide gate voltage window  $-4 \text{ V} < g_3 < -3.6 \text{ V}$  (black rectangle in fig. 37) we count 21 oscillations, corresponding

to a period of 19 mV, very close to the predicted one.

Such direct comparisons are difficult for the regime where the density does not change linearly with gate voltage unless  $n_{\text{UW}_1}$  is precisely known from spectroscopy measurements in the same configuration, as was the case for the previous section about Fabry-Perot resonances in the LW. We note that in the less negative gate voltage regime  $g_3 > -3.2$  V at least the qualitative behavior with growing oscillation periods as further UW modes are populated (slower density change in  $\text{UW}_1$  as a function of  $g_3$  due to screening) agrees with the prediction for Fabry-Perot resonances in the UW.

Finally, from the visibility of oscillations we can estimate the reflectance and transmittance of the contacts. After subtracting the parallel conductance  $\text{LW}_1$  (lowest mode of LW), the conductance oscillates in average by roughly 20% from  $1 e^2/h$  to  $0.8 e^2/h$ . Therefore we conclude (see eq. 25) that though the visibility of oscillations is quite large (20%), the reflectance  $R$  is only in the order of 5% ( $R = 0.05$ ;  $T = 0.95$ ).

We would like to add that electronic Fabry-Perot resonances have previously been observed in carbon nanotubes [132], in ballistic graphene [133] and also for (fractional) quantum hall states in GaAs heterostructures [134, 135].



## 5 Possible Evidence for Helical Nuclear Spin Order in GaAs Quantum Wires

Christian P. Scheller, Tai-Min Liu, Dominik M. Zumbühl

*Department of Physics, University of Basel, Klingelbergstrasse 82, CH-4056 Basel, Switzerland*

Gilad Barak, Amir Yacoby

*Department of Physics, Harvard University, Cambridge, Massachusetts 02138, USA*

Loren N. Pfeiffer, Ken W. West

*Department of Electrical Engineering, Princeton University, Princeton, New Jersey 08544, USA*

### Abstract

We present transport measurements of cleaved edge overgrowth GaAs quantum wires. The conductance of the first mode reaches  $2e^2/h$  at high temperatures  $T \gtrsim 10$  K, as expected. As  $T$  is lowered, the conductance is gradually reduced to  $1e^2/h$ , becoming  $T$ -independent at  $T \lesssim 0.1$  K, while the device cools far below 0.1 K. This behavior is seen in several wires, is independent of density, and not altered by moderate magnetic fields  $B$ . The conductance reduction by a factor of two suggests lifting of the electron spin degeneracy in absence of  $B$ . Our results are consistent with theoretical predictions for helical nuclear magnetism in the Luttinger liquid regime.

This chapter was published in *Phys. Rev. Lett.* **112**, 066801 (2014)

## 5.1 Motivation

Conductance quantization is a hallmark effect of ballistic one-dimensional (1D) non-interacting electrons [104, 106, 107, 136]. One mode of conductance  $e^2/h$  opens for each spin, giving conductance steps of  $2e^2/h$  for spin degenerate electrons. In presence of electron-electron (e-e) interactions, strongly correlated electron behavior arises, described by Luttinger liquid (LL) theory [88, 89, 137]. Salient LL signatures include ubiquitous power-law scaling [93, 96, 97, 102, 138], separation of spin and charge modes, and charge fractionalization - all recently observed [8, 85, 139, 140] in cleaved edge overgrowth (CEO) GaAs quantum wires [125, 126], thus establishing CEO wires as a leading realization of a LL. Interestingly, the conductance of a clean 1D channel is not affected by interactions, since it is given by the contact resistance in the Fermi liquid leads [10, 111–113, 141]. In presence of disorder, however, the conductance is reduced with LL power-laws [114, 115]. While short constrictions display universal quantization [106, 107], the ballistic CEO wires exhibit steps reduced below  $2e^2/h$  at temperatures  $T \geq 0.3$  K [2, 123], presenting an unresolved mystery [2, 85, 102, 127].

## 5.2 Main experimental findings

In this Letter, we revisit the conductance quantization in CEO wires, investigating for the first time low temperatures down to  $T \sim 10$  mK. We find that the conductance of the first wire mode drops to  $1e^2/h$  at  $T \sim 100$  mK and remains fixed at this value for lower  $T$ , while the electron temperature cools far below 100 mK. At high  $T \gtrsim 10$  K, the conductance approaches the expected universal value  $2e^2/h$  [2]. This behavior suggests a lifting of the electron spin degeneracy at low  $T$ , in absence of an external magnetic field  $B$ . The observed quantization values are quite robust, appearing in several devices, unaffected by moderate magnetic fields, and independent of the overall carrier density. A recent theory [1, 40, 118] predicts a drop of the conductance by a factor of two in presence of a nuclear spin helix - a novel quantum state of matter. Our data agree well with this model, while other available theories are inconsistent with the experiments,

thus offering a resolution of the non-universal conductance quantization mystery.

### 5.3 CEO wire sample

Ultra-clean GaAs CEO double wires (DWs) were measured (inset, Fig. 38), similar to Refs. [8, 85, 139, 140], offering mean free paths  $\sim 20 \mu\text{m}$  and subband spacings exceeding 10 meV. Details on sample fabrication are given in [2, 85, 123, 125, 126]. A surface gate allows depletion of the 2D electron gas (2DEG) below, giving edge conduction in the DW only, forming what we will refer to as the “wire”. Semi-infinite DWs with a few modes forming a 1D electron gas (1DEG) extend the wire on both sides, contacting the adjacent 2DEGs. Contacts to the 2DEGs are used to measure the two-terminal differential conductance  $g$  of the wire.

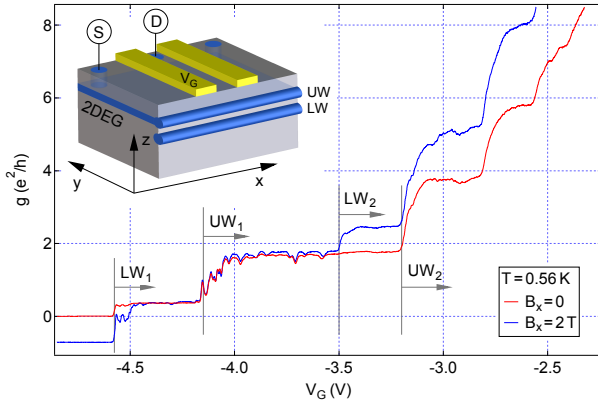


Figure 38: **Double wire mode structure** Differential conductance  $g$  (red) versus gate voltage  $V_G$  at  $T = 0.56 \text{ K}$  and  $B = 0$ . Arrows indicate  $V_G$  above which modes start to contribute to  $g$ , as labeled. Blue data is at  $B_x = 2 \text{ T}$  along the wire, offset in  $g$  to align  $LW_1$  plateaus. The inset shows a sample schematic with a coordinate system.

The sample comprises an array of gates with  $2 \mu\text{m}$  ungated spacing between  $2 \mu\text{m}$  long wires, allowing individual and serial operation. In the ungated regions, the upper wire (UW) modes run directly adjacent to the 2DEG, resulting in a 2D-1D coupling length  $\ell_{2D-1D} \sim 6 \mu\text{m}$  [127]. The 1DEG to few-mode wire transition occurs on a length

scale of about 500 nm - the distance of the UW and 2DEG to the surface gate - clearly longer than the Fermi wavelength  $\lambda_F \lesssim 200$  nm, and hence in the adiabatic regime. The lower wire (LW), on the other hand, has no adjacent 2DEG and is only weakly tunnel-coupled to the UW and 2DEG through a 6 nm thick AlGaAs barrier. UW to LW tunneling is very small in the gated segments. Thus, the  $2\mu\text{m}$  long DWs are considered as independent parallel resistors, with total conductance given by the sum of each conductance.

Figure 38 allows identifying the wire modes as a function of gate voltage  $V_G$ : increasing  $V_G$  starting from  $g = 0$  at the most negative voltages,  $g$  is increasing in a step-like manner as the DW modes are populated one by one, as indicated.  $LW_n$  ( $UW_n$ ) denotes  $n$ -th mode in lower (upper) wire. Since the first step is small  $\ll 2e^2/h$ , it is associated with the tunnel coupled  $LW_1$ . The next, larger step corresponds to  $UW_1$ , followed by the  $LW_2$  step, which becomes visible with a magnetic field  $B_X = 2$  T along the wires (blue trace, shifted to align  $LW_1$  plateaus). The tunneling process into the LW depends sensitively on parameters such as  $B$ , affecting the LW conductance. The next step has a large amplitude again and therefore corresponds to  $UW_2$ . Identifying higher modes is not easy due to a rapidly decreasing subband spacing.

## 5.4 Temperature dependence

The temperature dependence is shown in Fig. 39. At high  $T$ , the  $UW_1$  step height is approaching  $2e^2/h$ , as expected for a spin degenerate single mode wire. Thermally excited subband population and resulting inclined plateaus start to become visible at high  $T$ , as well as a feature reminiscent of 0.7 structure [142] at the low end of the plateau. At low  $T$ , on the other hand, the  $UW_1$  conductance plateau is reduced strongly to  $\sim 1e^2/h$ , contrary to the 0.7 feature, which rises to  $2e^2/h$  at low  $T$  [142]. In addition, the plateau develops pronounced, fully repeatable conductance oscillations. The same effect (transition from  $g = 2e^2/h$  to  $1e^2/h$ ) was seen in all four DWs, and also in single wires (see upper inset, Fig. 39(a)) Due to the lower quality of the single wires currently available (note the short plateaus), measurements were largely done on DWs. CEO

wires are extremely difficult to fabricate, limiting experiments to the present samples.

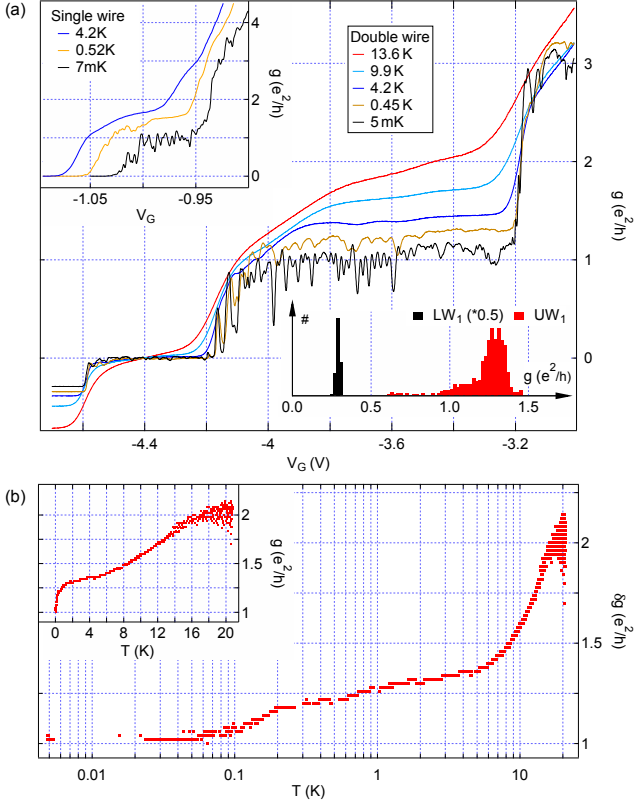


Figure 39: **Temperature effects** exhibiting conductance reduction by a factor of two (a) Gate voltage traces  $g(V_G)$  at  $T$  as labeled, shifted in  $g$  to align  $LW_1$  plateaus at  $g = 0$ . Similar measurements for a single wire are given in the upper inset. Lower inset: histogram of  $g(V_G)$  for  $LW_1$  and  $UW_1$  regions (base temperature). (b) Conductance step height  $\delta g$  of  $UW_1$  mode as a function of temperature on a logarithmic  $T$ -axis (linear axis in inset), extracted from histogram peak positions (see main text). Small but discrete steps in  $g$  result from histogram binning.

The oscillation pattern on the  $UW_1$  plateau - complicating extraction of the step height - is reproduced independent of the number of modes transmitted through an adjacent wire. This indicates ballistic addition of quantized mode steps, as expected for a mean

free path far exceeding the wire length. The oscillations are well understood as quantum interference caused by the finite size of the wire [5], giving maximal transmission  $\sim 1$  at the conductance maxima. Indeed, the maxima of the oscillations neatly line up forming an upper ceiling on the  $UW_1$  plateau, at intermediate  $T$  even forming flat tops, see Fig. 38. The minima, on the other hand, are rather dispersed over a range of conductances. A histogram extending over the first two conductance plateaus clearly reflects this behavior, see lower inset Fig. 39(a). A long, asymmetric tail to low  $g$  on the  $UW_1$  plateau (red) is seen below the peak at higher  $g$ . Therefore, we extract the peak positions  $g_{max UW_1}$  and  $g_{max LW_1}$  from the histogram and obtain the  $UW_1$  conductance step height  $\delta g = g_{max UW_1} - g_{max LW_1}$ .

The temperature dependence of  $\delta g$  at  $B = 0$  is displayed in Fig. 39(b) from 20 K down to 5 mK. Starting from the highest  $T$ , where  $\delta g$  reaches  $2e^2/h$ , lowering  $T$  continuously and monotonously decreases  $\delta g$  down to  $\sim 1e^2/h$ . We note that breaking of spin degeneracy would result in a reduction of the conductance by a factor of two. At low  $T \lesssim 100$  mK,  $\delta g$  becomes temperature independent. However, the sample temperature cools far below 100 mK: first, thermal activation of fractional quantum Hall states can be used to extract an electron temperature  $\leq 27$  mK, clearly smaller than 100 mK. Note that this  $T$  is an upper bound only, since disorder can lead to deviation from exponential activation at low  $T$ . Occasional formation of a wire quantum dot [102] leads to life-time broadened peaks not suitable for thermometry. Second, metallic Coulomb blockade thermometers [4] were measured under identical conditions, giving an electron temperature of  $10.5 \pm 0.5$  mK at refrigerator temperature  $T = 5$  mK. Details on filtering and heat sinking will be given elsewhere [3].

## 5.5 DC bias and B-field dependence

Next, we investigate the dependence on source-drain bias  $V_{SD}$ . Fig. 40(a) and (b) shows the conductance  $g_{UW}$  for  $V_G$  fixed on the  $UW_1$  plateau as a function of  $V_{SD}$ .  $g_{LW} \sim 0.3e^2/h$  depends only weakly on  $V_{SD}$ . At large  $V_{SD} > 1$  mV, conductances around  $2e^2/h$  are approached, while at low  $V_{SD} \sim 0$ , a sharp zero bias anomaly (ZBA)

of reduced  $g_{UW} \lesssim 1 e^2/h$  develops.

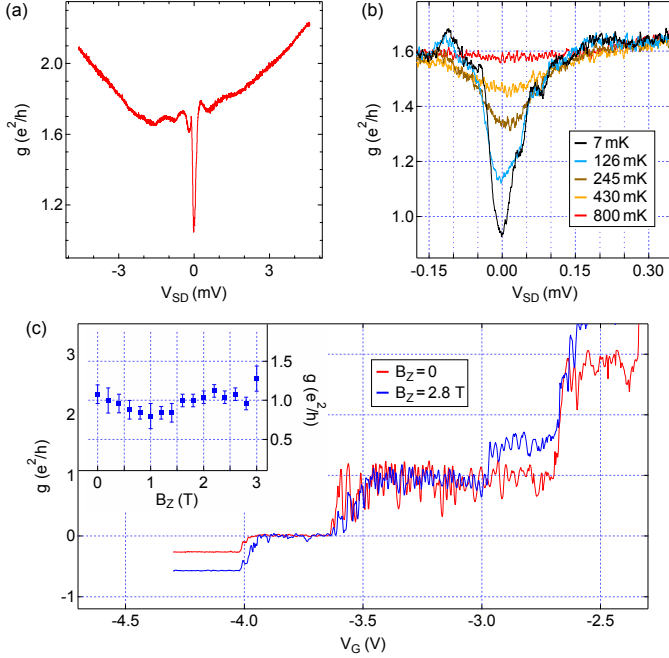


Figure 40: **Bias and B-field dependence** (a,b)  $g$  as a function of dc bias  $V_{SD}$ , for fixed  $V_G$  on the  $UW_1$  plateau. (b) shows different temperatures as labeled. (c)  $g$  at  $B = 0$  (red) and  $B_Z = 2.8$  T applied perpendicular to the 2DEG (blue), shifted in  $g$  to align  $LW_1$  plateau. The inset shows the conductance step height  $\delta g$  versus  $B_Z$ .

While the ZBA could be related to the energy to destroy the nuclear spin helix, it could also have various other origins. Further, large bias causes resistive heating, raising temperature. Indeed, the  $|V_{SD}|$  behavior and T-dependence shown in Fig. 39(b) appear qualitatively very similar. Given the sharp ZBA, great care was taken to keep  $V_{SD}$  small throughout all linear response measurements ( $V_{SD} = 3.5 \mu V$  - experimentally chosen to avoid non-linear effects).

We now turn to the influence of a magnetic field. Fig. 40(c) compares  $g$  at  $B = 0$  and  $B_Z = 2.8$  T perpendicular to the 2DEG, at base  $T$ . While  $g_{LW}$  is changed, the step

height  $\delta g$  is hardly affected at all:  $\delta g(B_Z)$  remains close to  $1 e^2/h$  within the error bars (see inset Fig. 40(c)), despite Landau levels and edge states induced by  $B_Z$  in the 2DEG, reaching filling factor  $\nu = 3$  at  $B_Z = 3$  T. Further, the transitions from  $LW_1$  to  $UW_1$  at the larger  $B$  are comparable to  $B = 0$  data (see e.g. Fig. 41) and do not provide evidence for an additional plateau. Note that at 3 T, the Zeeman splitting is much larger than temperature, and the Landau level spin splitting is already resolved for much lower  $B_Z \sim 0.3$  T. Finally,  $\delta g$  shows very little dependence on  $B_X$  (Fig. 38). Overall, we did not find evidence for qualitative changes of the  $UW_1$  conductance step in moderate  $B$ -fields.

## 5.6 Comparison with theoretical predictions

We emphasize that the experiments [2, 127], which studied single wires at  $T \geq 300$  mK, are consistent with the results presented in this Letter. New here is the full  $g$  reduction to  $g \sim 1 e^2/h$ ,  $T$ -independent for  $T \lesssim 100$  mK, combined with the sharp zero-bias dip,  $B$ -field independence, and pronounced low  $T$  conductance oscillations. In light of our new and complementary data, we now proceed to analyze different theories attempting to explain our findings, including re-examining models already discussed in Refs. [2, 127]. First, non-interacting theories must be rejected: reduced conductance quantization within the Landauer formula results from non-ideal transmission  $t < 1$  [136], in contradiction to the observation of ballistic transport in our wires, in addition to the objections already raised in Ref. [2]. Our measurements with two wires in series show that  $t$  is at most a few percent below  $t = 1$ , in any case ruling out a  $g$ -reduction by a factor of two.

Second, we examine e-e interactions in the wire. A weakly disordered LL connected to Fermi liquid (FL) leads [114] gives conductances decreasing below  $2 e^2/h$  with a power-law in  $V_{SD}$  and  $T$ . A finite conductance  $\propto L^{-1}$  is obtained at  $T = 0$  due to thermal freeze-out: when the thermal length  $L_T$  exceeds the wire length  $L$  at low enough  $T$ ,  $g$  becomes  $T$  independent. However, here,  $\delta g(T)$  remains clearly  $T$  dependent well below the freeze-out temperature  $\sim 0.6$  K (see Fig. 39) and further cannot reasonably be fit



with a single power law over the entire  $T$ -range. Therefore, LL theory for the  $2\mu\text{m}$  wire alone is an unlikely explanation.

Next, we consider e-e interactions also outside the wire. The 1DEGs may also experience non-FL correlations, albeit weaker than the wire since the 1DEGs are not single mode. The 2D-1D coupling scale  $\ell_{2D-1D} \sim 6\mu\text{m}$  sets an effective LL system length  $L_{1DEG} = 2 \cdot \ell_{2D-1D} + L$  comprised of segments  $\ell_{2D-1D}$  on each side of the  $L = 2\mu\text{m}$  wire. As  $T$  is reduced,  $L_T$  first grows larger than  $L$  before eventually surpassing  $L_{1DEG}$ , where  $g(T \rightarrow 0)$  saturates at  $g_{sat} \propto 1/L_{1DEG}$ . Hence, two temperature ranges with distinct power laws emerge, before  $g$  saturation at low  $T$ .

$\delta g(T)$  is consistent with such a model, giving decent agreement with two separate power-law fits. Further, a reasonable saturation temperature results:  $L_T > L_{1DEG}$  occurs on a temperature scale of  $\sim 0.1\text{K}$ , where indeed the  $\delta g$  data is seen to lose  $T$ -dependence. The value  $g_{sat} \sim 1e^2/h$  could then simply be a coincidence, but would depend on the details of the 2D-1D coupling. This coupling must involve scattering at an impurity or defect due to the large momentum mismatch between 1DEG and 2DEG electrons [2], and hence, within this model,  $g_{sat}$  will depend on parameters [143] such as disorder, chemical potential (density), and  $B$ -fields.

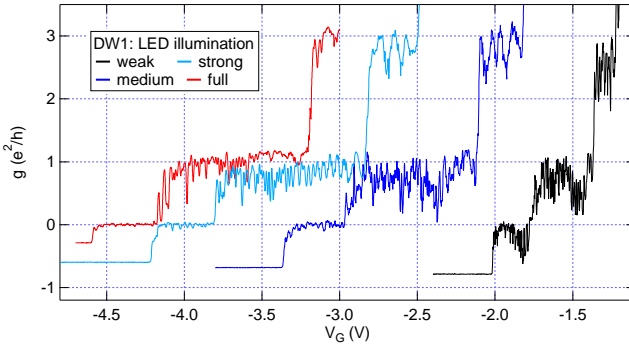


Figure 41: **Density dependence**  $g(V_G)$  for a DW, recorded after LED illumination as labeled. Traces were shifted in  $g$  only to align  $LW_1$  plateau at  $g = 0$ .  $\delta g$  appears independent of flash strength and hence carrier density.

Figure 41 displays  $g(V_G)$  for a sequence of LED illumination [85] steps, ionizing more and more donors and thereby globally increasing the carrier density and mobility after each flash. The depletion voltage is proportional to density, and is seen to become more negative with increasing LED exposure, enhancing the density by over a factor of two, see Fig. 41. Similarly, the 2D density and mobility increase by roughly a factor of two (before illumination, the density is  $1 \cdot 10^{11} \text{ cm}^{-2}$  and the mobility  $\sim 3 \cdot 10^6 \text{ cm}^2/(\text{Vs})$ ). Despite the large density change, the  $UW_1$  step height (ceiling of  $g$  oscillations) is seen to remain very close to  $1 e^2/h$ . This is seen also in the other wires. In absence of any significant density, disorder, wire, and B-field dependence (see Fig. 38 and 40) of  $g_{sat}$ , this scenario has to be abandoned.

A further model put forth in [2] and refined in [127] proposed a competition between  $\ell_{2D-1D}$  and residual backscattering in the wires on a length  $\ell_{BS} \gg L$  for the reduced  $g$  plateaus. This model is expected to exhibit a similar sensitivity to the 2D-1D coupling details as above, and can again be ruled out based on the observations in Fig. 41, augmenting objections already raised in [2, 127]. In addition, both  $\ell_{2D-1D}$  and  $\ell_{BS}$  have (weak) LL power-law  $T$ -dependence [144], leading to  $g \rightarrow 0$  for  $T \rightarrow 0$ , in contradiction to the finite  $g_{sat}$  observed. Another scenario is an incoherent LL due to Wigner crystal formation [145, 146]. In this model,  $g$  increases from  $1 e^2/h$  to  $2 e^2/h$  upon decreasing temperature, opposite to observations here. Further, very low densities  $(a_B n)^{-1} \gg 1$  are required ( $a_B$  is the GaAs Bohr radius), which is not the case for the wires used here. Finally, spin orbit coupling has to be ruled out as well, since the  $g$ -reduction is seen at  $B = 0$  and shows little  $B$ -dependence.

A recent theory by Braunecker, Simon and Loss [1, 40, 118] predicts helical nuclear spin order in a LL, causing a reduction of  $g$  by a factor of two, from  $2 e^2/h$  to  $1 e^2/h$  for a clean wire, as seen in the experiment here. Below a crossover temperature  $T^*$ , an effective RKKY interaction, strongly enhanced by e-e interactions, forces the nuclear spin system via hyperfine interaction into helical order, constituting a novel state of matter. The resulting large Overhauser field acts back on the electronic system where a large gap opens - pinned at the Fermi energy - for half of the low energy modes,

forming a helical LL and causing the  $g$  reduction at  $B = 0$ , applicable similarly for single and double wires [147]. The wire then only transmits spin-down right and spin-up left movers, therefore acting as a perfect spin filter. Note that the nuclear spin helix is a thermodynamic ground state protected by a gap, rather than a dynamic nuclear spin polarization.

The predicted  $T^*$  depends very strongly on the charge LL parameter  $K_C$  and can exceed 1 K for small  $K_C$  (strongly interacting) [1]. Full nuclear order is obtained only at  $T \ll T^*$  and zero polarization only at  $T \gg T^*$ . Estimating  $K_C$  is far from trivial both experimentally and theoretically [8]:  $K_C = 0.4$  gives  $T^* \sim 0.2$  K and  $K_C = 0.3$  already  $T^* \sim 0.6$  K, consistent with the experiment. Further, large  $T^*$  result in a rather broad, washed-out transition, as observed in the experimental  $\delta g(T)$ .  $K_C$  is expected to depend (weakly) on density  $n$ , therefore  $T^*$  will change over a conductance plateau. However, given a very broad transition, this may affect  $g$  only weakly, and give rather flat conductance plateaus, as seen in the experiment. Further, the theory derives  $g$  far below and above, rather than throughout, the nuclear transition, allowing only a qualitative comparison. Finally, a Zeeman splitting much smaller than the induced gap should affect neither the nuclear order nor the conductance, as seen in the experiment.

## 5.7 Summary and Conclusions

In summary, we have investigated B-field conductance quantization in single mode LL wires, finding a very broad transition at  $B = 0$  from  $2e^2/h$  at high  $T$  to  $1e^2/h$  at low  $T \lesssim 100$  mK, where  $g$  becomes  $T$  independent. This behavior is consistently seen in double and single wires, is independent of overall density and disorder (2D-1D coupling, illumination), is destroyed with bias  $V_{SD}$  similar to  $T$ , and is insensitive to moderate B-fields. All these observations are in good agreement with a nuclear spin helix model [1, 40, 118] which predicts a crossover temperature  $T^*$  in the observed range, while all other theories considered here and previously [2, 127] are inconsistent with the data. While we can not rule out other explanations we are not aware of, we emphasize that the data are striking and stand alone, irrespective of the model used for interpretation.

Further experiments are needed to investigate the role of the nuclear spins. Resistively detected NMR was already attempted here: While detecting clear 2DEG signals, no identifiable NMR response was found for the wires. However, it is difficult to estimate what the effect of an NMR excitation is, what the low energy nuclear spin excitations are, and whether a detectable resistive signal would result. Spectroscopic methods [85] might be used to shed more light on the electronic structure. In the nuclear spin helix state, the electron system is in the helical LL regime, equivalent to a spin-selective Peierls transition in a Rashba spin-orbit coupling wire [118]. Given proximity to an s-wave superconductor, a topological phase sustaining Majorana fermions could be created.

## Acknowledgments

We would like to thank O. Auslaender, B. Braunecker, D. Loss, D. L. Maslov, T. Meng, M. Meschke, J. Pekola, P. Simon and Y. Tserkovnyak for valuable inputs and stimulating discussions. This work was supported by the Swiss Nanoscience Institute (SNI), NCCR QSIT, Swiss NSF, ERC starting grant, and EU-FP7 SOLID and MICROKELVIN. AY acknowledges support from the NSF DMR-1206016. The work at Princeton was partially funded by the Gordon and Betty Moore Foundation through Grant GBMF2719, and by the National Science Foundation MRSEC-DMR-0819860 at the Princeton Center for Complex Materials.

## 6 Thermally Activated Charge Fluctuations in a Few Electron GaAs Double Quantum Dot

Daniel E. F. Biesinger, Christian P. Scheller, Dominik M. Zumbühl

*University of Basel, Klingelbergstrasse 82, CH-4056 Basel, Switzerland*

Bernd Braunecker

*Dpto. Física Teórica de la Materia Condensada, UAM, Madrid Spain*

J. Zimmerman, A.C. Gossard

*Materials Department, University of California, Santa Barbara, California, USA*

### Abstract

We report intrinsic metastable charge state switching in a laterally defined GaAs few electron double quantum dot in the limit of very low tunnel rates. Charge switching is recorded in real-time with a nearby charge sensor and appears within a diamond shaped region between two associated triple points of the charge stability diagram. The switching rate is gate tunable and shows an exponential temperature dependence. We provide a straight forward extension to the orthodox theory for electron transport in double dots that reproduces our experimental findings.

This chapter is in preparation for publication

## 6.1 Motivation

Quantum dots are promising candidates for the implementation of qubits, the building block of a quantum computer, in solid state systems [148]. Numerous sophisticated experiments have demonstrated the successful implementation, control and single-shot readout of electron-spin qubits in GaAs quantum dots [78, 149–153]. The dynamics of the electron spin is characterized by two time scales, the relaxation time  $T_1$  and the coherence time  $T_2$ . Since energy relaxation inevitably destroys coherent spin-states, the  $T_1$ -time always sets an upper limit for  $T_2$ ,  $2T_1 > T_2$  [154, 155]. In practice the measured  $T_2$ -time is usually much shorter than its theoretical maximum e.g. due to the interactions of the electron spin with the Overhauser-field created by the nuclear spins of the host material. In recent experiments, where the electron spin was decoupled from the slowly varying Overhauser-field by means of spin-echo techniques (also known under dynamical decoupling), dephasing up to 200  $\mu$ s were achieved [156].

## 6.2 Experimental findings

In this Letter we present intrinsic charge fluctuations (ICFs) in a GaAs few electron double quantum dot (DQD). They appear within a diamond shaped region of the charge stability diagram (CSD) with the short diagonal defined by the zero detuning line of associated triple points. ICFs are measured in real-time with a nearby charge sensor. We stress that due to limited measurement bandwidth ICFs are only visible in the limit of low electron temperatures (here  $T_e \lesssim 80$  mK), small tunnel rates and negligible interdot tunneling.

We show that these ICFs result from a metastability of e.g. the (0,1)-(1,0) states. Switching between configurations takes place via the (0,0) and (1,1) intermediate states, i.e. includes an electron exchange with the leads and consequently leads to complete loss of coherence. As the switching frequency scales with the strength of tunnel barriers (to source and drain), this effect can be a limiting factor for  $T_2$ -measurements where short initialization times are desirable.

We note that this thermally activated process could be used for thermometry purposes.

### 6.3 Sample fabrication and charge stability diagram

We fabricate our samples on an  $\text{Al}_{0.3}\text{Ga}_{0.7}\text{As}/\text{GaAs}$  heterostructure which incorporates a 2D electron gas (2DEG) 110 nm below the surface of the wafer. The 2DEG features a density of  $n = 2.6 \cdot 10^{11} \text{ cm}^{-2}$  and a mobility of  $\mu = 4 \cdot 10^5 \text{ cm}^2/\text{Vs}$ . Ti/Au surface depletion gates are used to form and control the nanostructure, see SEM picture in fig. 42(a).

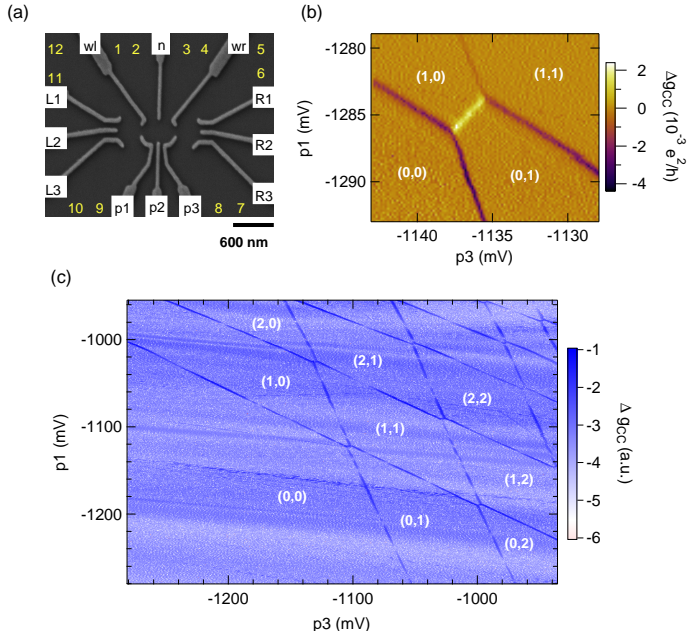


Figure 42: (a) SEM picture of a device similar to the one studied in the experiment. Yellow numbers indicate ohmic contacts and gates are labeled in black (on white background). Gates p1 and p3 are used to control the double dot while L1, L2 and L3 form the left sensor dot. (b) Sensor conductance  $g_{CC}$  in the vicinity of the (0,0) - (1,1) transition point with a smooth background subtracted. (c) Large section of the CSD with numerous charge configurations ( $N_1, N_2$ ) as indicated.

Single quantum dots on either side of the double dot are used as real-time charge

sensors and allow for single-shot charge readout with a minimum rise time of  $6 \mu s$  and sensitivities as large as  $\delta g/g \sim 1$  per electron [157–159]. All data shown in this letter was acquired with the left charge sensor, though similar results were obtained also with the right sensor. The measurement sensitivity is maximized by gate tuning of the sensor dot onto the rising (falling) edge of a coulomb blockade peak. During measurements the conductance was held approximately constant by means of a linear feed-back mechanism applied to gate L2 such that the capacitive coupling, induced by gates p1 and p3 (see fig. 42(a), is compensated. Together with an exceptional device stability, the feed-back mechanism allows for high resolution measurements of the CSD diagram across many different charge configurations as shown in fig. 42(c). Clear parallel lines with two different slopes correspond to addition of a single electron in either left or right dot as indicated in fig. 42(c) (white labels).

Measurements were done at base temperature  $T_{\text{base}} = 22 \text{ mK}$  (unless explicitly stated differently) of a standard  $^3\text{He}$ - $^4\text{He}$  dilution refrigerator with an electron temperature of  $\approx 80 \text{ mK}$ .

We now focus on the (0,0) - (1,1) transition (fig. 42(b)) and find a clear undisturbed zero detuning line separating the (1,0) and (0,1) charge states. All measurements in fig. 42 are completely reproducible and overall we observe standard textbook like behavior for a DQD.

## 6.4 Metastable region in the CSD

The situation drastically changes upon decreasing the tunnel coupling to source and drain as well as the inter-dot tunneling. The straight zero detuning line transforms into a diamond shaped region (fig. 43(a)) wherein the adjacent charge sensor records time dependent switching between the (0,1) and (1,0) charge states. Depending on the position within the diamond shape, switching frequencies range from 5 Hz up to a few kHz. An exemplary time trace is shown in fig. 44(e). Though we focus on the (0,0) - (1,1) charge transition in this Letter, we note that the diamond shape also appears at higher charge transitions. Therefore, and because the effect can be observed over a



wide range of gate voltages (the diamond remains at fixed position within the CSD upon reshaping the dot), we rule out trapped charges as a possible cause. From the real-time measurements, integrated over 20 ms, we can not only extract the average conductance (fig. 43(a)), but also the standard deviation of the sensor signal as shown in fig. 43(b). While the diamond shape clearly appears in the standard deviation, the tunneling rates are still too large for charge transition lines (white solid lines, extracted from fig. 43(a)) to be resolved. Remarkably, the borderline of the diamond (white dashed lines) is well approximated by two pairs of parallel lines with slopes equal to the lines in the CSD. Since the latter represent alignment of source or drain chemical potential with an energy level of the adjacent quantum dot, this suggests that the leads might be involved.

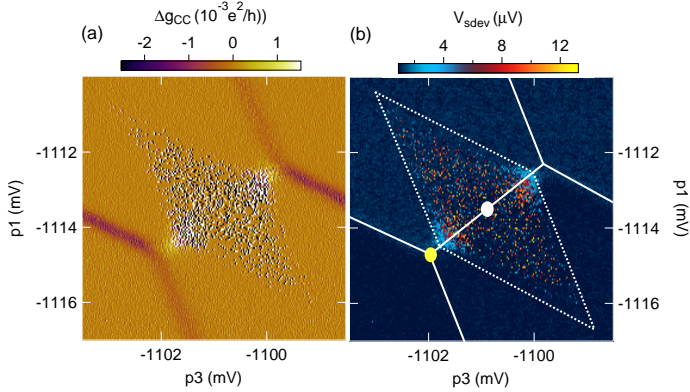


Figure 43: Real-time conductance data recorded with the left charge sensor at the (0,0) - (1,1) transition point. Every data point in (a) corresponds to an average conductance, integrated over 20 ms. The standard deviation for the same data is shown in (b). Solid white lines indicate charge transition lines from (a). The borderlines of the diamond shaped region are shown as white dashed lines. White and yellow dots refer to data analysis presented in fig. 45.

The charge switching persists even at very small bias voltages of  $5 \mu\text{V}$  across the sensor dot. Together with the low electron temperatures  $\approx 80 \text{ mK}$  and the broad energy spectrum of the diamond (short diagonal corresponds to  $148 \mu\text{eV}$  or  $1.7 \text{ K}$ ) it seems very unlikely that phonon- or photon assisted tunneling is responsible for this effect [160]. Our observations also qualitatively differ from all kind of sensor back actions

reported in literature [161–163].

## 6.5 Analysis of the measured real-time data

In order to quantify this process more thoroughly, we proceed to measure the tunneling rates  $\Gamma_L = \Gamma_{(0,1) \rightarrow (1,0)}$  and  $\Gamma_R = \Gamma_{(0,1) \rightarrow (1,0)}$  for tunneling "from the right to the left" dot and vice versa for each position within the diamond (figs. 44(a),(b)). In practice we record one 20 s long real-time trace (fig. 44(e)) for each gate position in fig. 44(a). A trigger system decides on the presence (or absence) of switching events, and in case of positive confirmation further 14 traces are recorded. The tunneling rates can easily be calculated from the real-time data. The rate  $\Gamma_L$  for tunneling to the left dot is given by the total number of switches  $N$  (in all 15 traces) divided by two times the accumulated time  $T_R$  that an electron spends in the right dot  $\Gamma_L = N/(2 T_R)$  and equivalently for the reversed process.

While  $\Gamma_L$  is largest at the left boarder of the diamond,  $\Gamma_R$  reaches its maximum values at the opposite boarder (figs. 44(a),(b)). Tunneling rates drastically drop when moving away from the boarder and are rather low inside the diamond (see logarithmic scale in figs. 44(a),(b)). Next we calculate the switching frequency  $f$  (fig. 44(c)) and probability  $P_R$  for being in the right dot (fig. 44(d)) from tunnel rates  $\Gamma_L$  and  $\Gamma_R$ ,  $f = 2(1/\Gamma_L + 1/\Gamma_R)^{-1}$  and  $P_R = \Gamma_R/(\Gamma_L + \Gamma_R)$ . The probability  $P_L$  for being in the left dot can be calculated accordingly and is equal to  $1 - P_R$ . For the switching frequency  $f$ , two pronounced maxima are observed. Since a full switching cycle includes both tunnel rates ( $f \sim \Gamma_L \cdot \Gamma_R$ ), large frequencies are observed where both  $\Gamma_L$  and  $\Gamma_R$  are large. Within the diamond  $f$  is rather small and varies only little with position.

We note that the measured tunnel rates are strongly temperature dependent. Fig. 45(f) shows  $\Gamma_L$  as a function of refrigerator temperature  $T_R$ , recorded in the center of the diamond. Apart from the low temperature saturation at  $\approx 80$  mK, attributed to a saturating electron temperature, the tunnel rate  $\Gamma_L$  increases exponentially which indicates that the switching is thermally activated.

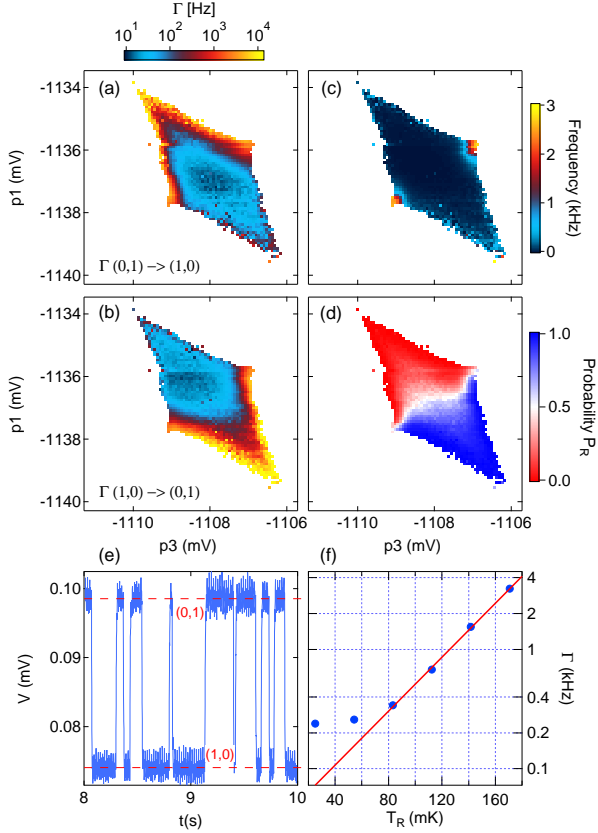


Figure 44: (a) Tunnel rate from (0,1) to (1,0) in logarithmic scale. (b) Tunnel rates for the reversed process. (c) The average switching frequency. (d) Probability  $P_R$  for being in the right dot, calculated from the tunnel rates in (a) and (b).  $P_R$  is 50% on the zero detuning line and approaches 1/0 for positive/negative detuning. The probabilities  $P_{(1,1)}$  and  $P_{(0,0)}$  are assumed to be negligible. (e) Exemplary real-time trace as used to extract  $\Gamma$ . (f) Exponential temperature dependence of  $\Gamma$  as described in the main text. The low temperature saturation is attributed to a saturating electron temperature.

The key point is to realize that the diamond shape defines the region within which both (0,1) and (1,0) state lie below the source-drain chemical potential and are therefore energetically accessible. As discussed in full length in the last section of this Letter,

the observed "apparent" switching between (0,1) and (1,0) is a result of fast electron exchange with the leads through either the (0,0) or the (1,1) intermediate state.

## 6.6 Time resolved 4-level system in the metastable region

An experimental verification, i.e. a time-resolved measurement of the four-level system would give strong support to the previous statements. In order to increase the dwell time for the short intermediate states but maintain sufficiently large switching frequencies at the same time, we increase the tunnel barriers and heat up the refrigerator to  $T_R = 200$  mK. Fig. 45 shows an example trace of the time resolved four level system with respective states as labeled, measured in the center of the diamond. More statistics is required to proof that the zoomed in trace in fig. 45(a) originates from a true 4-level system and is not just a random event. A histogram is created for each real-time trace from a large dataset. Histograms are summed up after normalizing each individual one to the peak position of the (0,1) and (1,0) charge states. Indeed we find a clear 4-level system for data acquired in the center of the diamond (fig. 45(b)). For comparison we show data recorded at the (0,0)-(0,1)-(1,0) triple point (fig. 45(c)) where, as expected, a 3-level system is observed (similar results are obtained for the adjacent triple point). Finally, at the charge transition lines, true 2-level systems can be resolved.

If we assume energy independent (identical) tunnel rates to source and drain, a sample electron temperature  $T_e$  of  $T_e = T_R = 200$  mK and furthermore assume that data in fig. 45(b) is acquired exactly in the middle of the diamond, then the ratio between high and low peaks in fig. 45(b) is given by the Boltzmann-factor. Conversely, the energy scale for the diamond can be calculated from the number of counts e.g. in the (1,1) and (0,1) states and the known temperature. We obtain  $\Delta E = 200 \pm 40 \mu\text{eV}$  in reasonable agreement with the measured width of  $148 \mu\text{eV}$ . The latter is measured in a slightly different dot configuration with larger tunnel rates. This fact together with small drifts away from the center of the diamond during data acquisition might be responsible for the discrepancies.

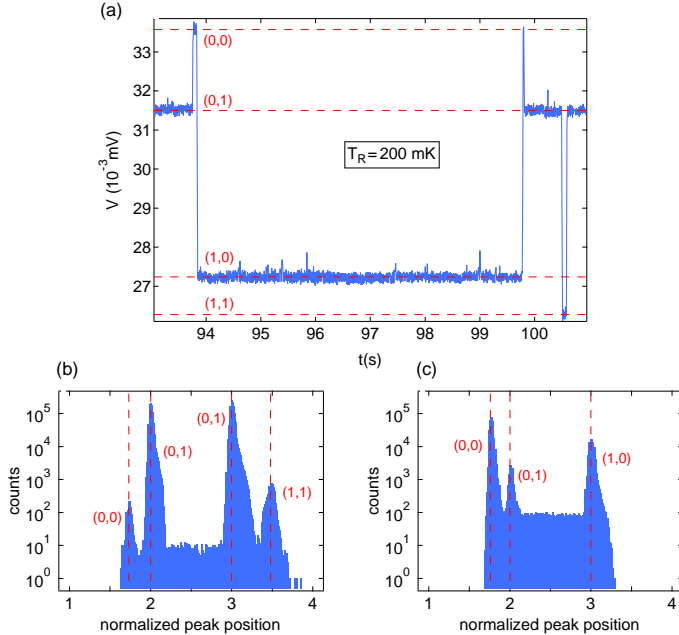


Figure 45: (a) Example trace for the time-resolved four level system, recorded at a temperature  $T_R = 200$  mK in the center of the diamond (position indicated as white dot in fig. 43(b)). (b) Histogram from numerous real-time traces as shown in (a). Peak positions are normalized to the (1,0) and (0,1) charge states before summing up histograms. (c) For comparison, we show histogram data for the lower triple point (yellow dot in fig. 43(b)) where the expected three level system can be clearly identified.

## 6.7 Extension of the orthodox theory for transport in DQDs

We provide in the following a straightforward dynamical extension of the orthodox theory for transport in double dot systems [23] that captures the main features of the charge fluctuations with a minimum of assumptions. Following this, we discuss which further nonuniversal effects must be taken into account for direct comparison with the experimental data.

We start by noting that the switching rates observed in the experiment are slow enough such that we can use a semi-classical description with definite occupation numbers  $N_j$

of dots  $j = 1, 2$ . The charge fluctuations lead to switching between different configurations  $x = (N_1, N_2)$ , which we express through a master equation for the occupation probabilities  $p(x)$ ,

$$\partial_t p(x) = \sum_{x' \neq x} [\Gamma_{xx'} p(x') - \Gamma_{x'x} p(x)], \quad (27)$$

with  $\Gamma_{xx'}$  the tunneling rate from configuration  $x'$  to  $x$ . In accordance with the experiment, the four configurations of relevance for the investigated region of the CSD are  $x = (1, 0), (0, 1), (0, 0)$ , and  $(1, 1)$ . From the data we see that we can neglect a direct tunneling between the two quantum dots,  $(1, 0) \leftrightarrow (0, 1)$ , because it would lead to resonant switching rates at the boundary between the  $(1, 0)$  and  $(0, 1)$  regions of the CSD, which are not observed. Instead the switching rates increase towards the borders of the diamond indicated by the dashed lines in fig. 43, where the chemical potential of one of the dots comes close to the Fermi level of the neighboring lead [see fig. 46(a)]. This indicates that the  $(1, 0) \leftrightarrow (0, 1)$  transition takes place mainly through the intermediate of the  $(0, 0)$  and  $(1, 1)$  states, in which electrons are exchanged between dots and leads, and for eq. 27 we keep only the rates between the states  $(1, 0) \leftrightarrow (0, 0) \leftrightarrow (0, 1)$  and  $(1, 0) \leftrightarrow (1, 1) \leftrightarrow (0, 1)$ . By the Pauli principle, the bare tunneling rate  $\Gamma_j$  between dot  $j$  and its neighboring lead are weighted by the number of occupied lead states when tunneling onto the dot,  $f(\mu_j(N_1, N_2))$ , and by the number unoccupied lead states when tunneling out of the dot,  $1 - f(\mu_j(N_1, N_2))$ . Here  $\mu_j(N_1, N_2)$  is the chemical potential of dot  $j$  [23],  $f(\epsilon) = [1 + \exp(\epsilon/k_B T)]^{-1}$  the Fermi function (with Boltzmann constant  $k_B$  and temperature  $T$ ), and we have chosen the zero of energy at the Fermi level  $\epsilon_F = 0$  of the unbiased leads. This leads to the set of rates  $\Gamma_{(1,0),(0,0)} = \Gamma_1 f(\mu_1(1, 0))$ ,  $\Gamma_{(0,0),(1,0)} = \Gamma_1 [1 - f(\mu_1(1, 0))]$ ,  $\Gamma_{(1,1),(1,0)} = \Gamma_2 f(\mu_2(1, 1))$ ,  $\Gamma_{(1,0),(1,1)} = \Gamma_2 [1 - f(\mu_2(1, 1))]$ . With exchanged dot indices  $1 \leftrightarrow 2$  we obtain the corresponding rates involving  $(0, 1)$ . We have furthermore assumed energy independent  $\Gamma_j$ . The stationary solution  $\partial_t p(x) = 0$  of eq. 27 becomes now the straightforward inversion of a  $4 \times 4$  matrix and leads to the results shown in fig. 46 (c) - (f), which reproduce the main features shown in fig. 44.

To understand better the implications of this model, let us assume that  $(0, 1)$  is the dot

ground state and focus on the transition to the metastable state  $(0, 1) \rightarrow (0, 0) \rightarrow (1, 0)$  as shown in fig. 46(a).

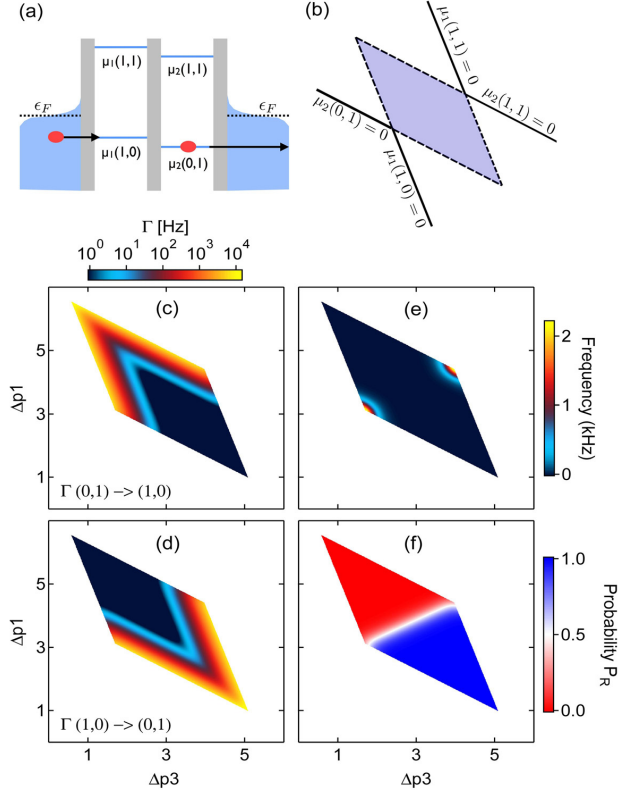


Figure 46: (a) Illustration of the effective switching  $(1, 0) \rightarrow (0, 1)$  by first tunneling out of the right dot (slow rate, suppressed by almost unavailable unoccupied states in the lead), and then tunneling onto left dot into the metastable  $(1, 0)$  state (fast rate due to high occupation number in lead at this energy). (b) Chemical potential at the borderlines of the honey comb with blue area indicating where both  $\mu_1(1, 0), \mu_2(0, 1) < \epsilon_F = 0$ . (c)-(f) Calculated transition rates, average switching frequency and probability qualitatively matching the experimental results shown in fig. 3(a)-(d). For the calculations  $T_e = 80$  mK and  $\Gamma_1 = \Gamma_2 = 20$  kHz were assumed.

The first transition, the tunneling of the dot electron into the lead, is strongly sup-

pressed, as  $\mu_2(0,1) < 0$  and as the number of available unoccupied lead states is described by the exponentially small tail of the Fermi function  $1 - f(\mu_2(0,1))$  only. Such rare transitions set the overall time scale for the slow switching rates. The state  $(0,0)$  obtained after this tunneling event, however, is highly unstable since tunneling back into  $(0,1)$  is weighted by  $f(\mu_1(0,1))$ , and so the rate is on the order of the bare tunneling rate  $\Gamma_2$ . Yet, within the shaded diamond-shaped region shown in fig. 46(b), the chemical potential of dot 1 for the configuration  $(1,0)$  lies below the Fermi level as well,  $\mu_1(1,0) < 0$  [fig. 46(a)], and tunneling into this metastable state has a large rate  $\Gamma_1 f(\mu_1(1,0)) \sim \Gamma_1$ , too. This tells us that the particle indeed spends a notable fraction of time in  $(1,0)$ , with short excursions over  $(0,0)$  as well as over  $(1,1)$ . The weighting by the Fermi functions shows that the switching frequency increases when  $\mu_1(1,0), \mu_2(0,1)$  or  $\mu_1(1,1), \mu_2(1,1)$  (for transitions over  $(1,1)$ ) approach 0, which corresponds to approaching the dashed boundaries of the shaded region in fig. 46(b). Close to the lower triple point  $\mu_1(1,0) = \mu_2(0,1) = 0$ , the average time spent in  $(0,0)$  becomes of the same order as the time spent in  $(0,1)$  and  $(1,0)$ , while state  $(1,1)$  is almost never populated and decays very quickly. Close to the upper triple point  $\mu_1(1,1) = \mu_2(1,1) = 0$ , the role of  $(0,0)$  and  $(1,1)$  is reversed. On the other hand, the line  $\mu_1(1,0) = \mu_2(0,1)$  marking the separation between the  $(0,1)$  and  $(0,1)$  regions in the CSD has no special feature since the direct tunneling  $(0,1) \leftrightarrow (1,0)$  is absent. All these characteristics reproduce the main experimental observations.

### 6.7.1 Discrepancies between measured data and theoretical predictions

Of course, there are discrepancies between the minimal model and the realistic data. Most prominent is the S-shape seen in fig. 44(d). We can think of two different origins of the S-shape. First, if each dot is tunnel coupled to more than a single lead, slight differences in the Fermi levels lead to a multi-step shape of the transition rates, due to the sum over shifted Fermi functions. Second, the changed Coulomb repulsion of the lead electrons by the changed number of charges on the dots can be seen as a slight shift of the lead ground state energy, and so of  $\epsilon_F$ . The different energy shifts induced



by the  $(1,1)$  and  $(0,0)$  configurations introduce an asymmetry along the  $(0,1), (1,0)$  boundary.

## 6.8 Summary

In summary we report intrinsic metastability in a GaAs DQD. A straight forward extension to canonical theory of electron transport in double dots captures our experimental observations. As the observed metastability is based on thermally activated electron exchange with the leads, the corresponding time scale sets an upper limit on the  $T_2$ -time. In GaAs systems this becomes relevant when the hyperfine interaction has already been reduced by dynamical decoupling. The positive aspect is that the switching frequency is gate tunable and can be made very small. The drawback is, however, that long switching times would automatically imply long qubit initialization times, vastly exceeding recently demonstrated time scales of 50 ns [164].

## Acknowledgments

We gratefully acknowledge funding by the SNF.

B.B. acknowledges the support by the EU-FP7 project SE2ND [271554].



## 7 Summary and Outlook

### Going to lower electron temperatures

Quite some efforts were made to achieve low electron sample temperatures. In particular, new cryogenic microwave filters were developed and installed for all signal cables. Their design is similar to the well known copper powder filters, however, the filling material (outer conductor) is replaced with conductive silver epoxy to improve thermalization properties. In terms of transmission characteristics we were able to significantly lower the cut-off frequency by means of a special winding technique that reduces parasitic capacitive couplings. In addition to microwave filters, mounted at the mixing chamber plate and a second stage inside the sample can, a home built and heat-sunk silver epoxy sample holder was installed.

Electron temperatures as low as 7.5 mK, measured in metallic coulomb blockade thermometers, demonstrate a very efficient cooling strategy. The present low temperature setup system enables very fragile effects to be measured such as the  $5/2$  fractional quantum hall state which is part of ongoing research.

A further attempt to lower the electron temperature even more does not make much sense for the present dilution refrigerator with a base temperature of roughly 5 mK. However, a different experiment in our group focuses on approaching the  $\mu$ -Kelvin regime by means of adiabatic demagnetization. There, initial measurements with a second filtering stage and a new silver epoxy sample holder already showed significant improvements and allowed to reduce the electron temperature in a CBT down to 5.2 mK.

### Cleaved edge overgrowth wires

A low temperature saturation of nonuniversal conductance step size is observed in CEO single and double quantum wires. While conductance reduction in surface gated GaAs quantum wires was attributed to finite disorder, this does not seem to apply in our DWs where Fabry-Perot resonances are found, a demonstration of ballistic transport over at

least  $6\ \mu\text{m}$  i.e. 3 times the wire length. Also, scattering mechanisms as considered by A. Yacoby, R. de Picciotto and others, do not agree with our observations as they do not predict low temperature saturation.

The conductance measurements on CEO double wires did indeed show the theoretically predicted low temperature limit of  $1e^2/h$  for a clean LL confined to one transversal mode and embedded in a 3D system of nuclear spins. The predicted high temperature limit of  $2e^2/h$  is only restored at  $T \approx 16\ \text{K}$  which is consistent with previous measurements but much higher than expected in the picture of helical nuclear magnetism.

While transport measurements with focus on the reduced conductance address the predicted partial opening of an electronic gap induced by the nuclear Overhauser field, NMR type measurements could give direct evidence for nuclear ordering. It is not so clear though what to expect from NMR measurements. On one hand, if we assume that in the ordered phase the whole helimagnet has to be flipped in NMR, then attributed NMR frequencies would be gigantic. On the other hand, since electrons only possess a finite weight in the order of 1% at nuclear sites, a standard NMR response at elevated frequencies might exist.

However, the fundamental excitations for a nuclear helimagnet are spin density waves, so called magnons, rather than individual spin flips. A mapping of the magnon spectrum as a function of temperature could give further evidence for the presence of nuclear order.

In the following some preliminary measurement results are shown for a CEO wire under RF-irradiation using the NMR setup presented in chapter 1. We underline that the following data is not understood, and hence no final conclusions will be drawn. The intention is to give the reader a brief overview on different approaches that have been pursued and to present some preliminary experimental observations.

In the upper panel of fig. 47 we present CEO wire conductance data as a function of top gate voltage and frequency. In order to visualize small conductance changes as a function of frequency on a largely varying background ( $g > 1000e^2/h$  at zero top gate voltage and  $< 0.01e^2/h$  in the pinch off regime) we renormalize  $g(\nu)$  separately

for each gate voltage  $g_3$  separately (each vertical linescan) in fig. 47. Normalized current, voltage and calculated relative resistance are shown in the three lower panels. For orientation we plot a CEO wire conductance trace (blue) superimposed to the normalized conductance data in the upper panel.

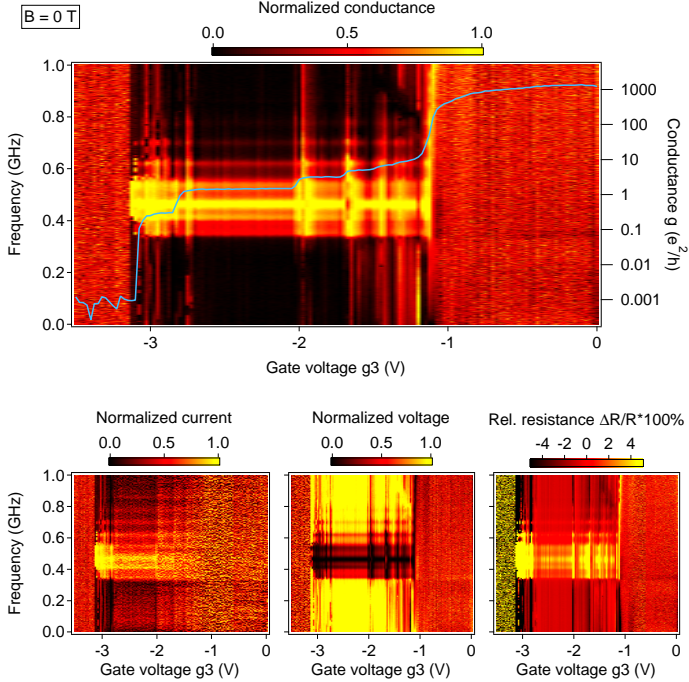


Figure 47: The top panel shows the CEO wire conductance as a function of gate voltage  $g_3$ , recorded at base temperature (with large bias voltage, equiv.  $T \lesssim 4$  K) and zero B-field. For visibility reasons each vertical line is renormalized. Superimposed to the false color data is a single conductance trace (horizontal cut at the lowest frequency). In the lower panels we present normalized current and voltage data as well as the calculated (percentual) relative resistance change.

The measurement is done at base temperature of the refrigerator for zero external magnetic field. However, quite large currents were used for the current biased measurement in fig. 47, leading to a large AC voltage drop across the wire ( $V_{AC} \leq 300 \mu\text{V}$ ) and

consequently the electron sample temperatures significantly larger than the refrigerator temperature  $T_R$ .

We observe a clear response to RF-irradiation in the regime where current flows only through the edge channel. These resonances are absent when the quantum wire is pinched off completely (no current flow). Also we do not observe any response to RF-irradiation for small gate voltages where current is carried mainly by the 2DEG. In the latter case, this could simply be due to the small 2DEG resistance which results in a very small voltage drop, i.e. it is difficult to measure the voltage drop with high precision (signal to noise ratio). In order to exclude this simple effect, we calculate the relative resistance change, shown in the lower right panel in fig. 47. The limits for the color scale, -5% to +5% resistance change, are chosen such that the resonances are clearly visible. In the pinch off regime all data points are saturated (exceed the color scale). This is obvious since the current is zero within some noise level, and consequently current fluctuations are large compared to its average value. For the regime where the 2DEG contributes to the current, surprisingly, the relative resistance change is smaller than the observed size of resonances. This suggests that the absence of RF response is not due the limited measurements sensitivity and that resonant features in fig. 47 due to RF-irradiation are related to edge conductance.

The situation changes in presence of an external magnetic field  $B_z$  applied perpendicular to the 2DEG. Data shown in fig. 48 was recorded under the same experimental conditions as data in fig. 47 but with an additional B-field  $B_z = 3.3$  T, corresponding to a filling factor in between 2 and 3 (standard RDNMR was observed in this configuration even with applied top gate voltage, as long as the wire is not pinched off). There is still response to RF-irradiation in a similar frequency regime around 400-600 MHz that stops when the quantum wire is pinched off. In contrast to the zero B-field data these resonances extend up to zero gate voltage. Since electron transport in a (sufficiently strong) perpendicular B-field is reduced to edges, even at zero top gate voltage the 2DEG does not contribute to the total current. Therefore, also data recorded at finite B-field indicates a connection between observed RF resonances and current transport through the sample edges.

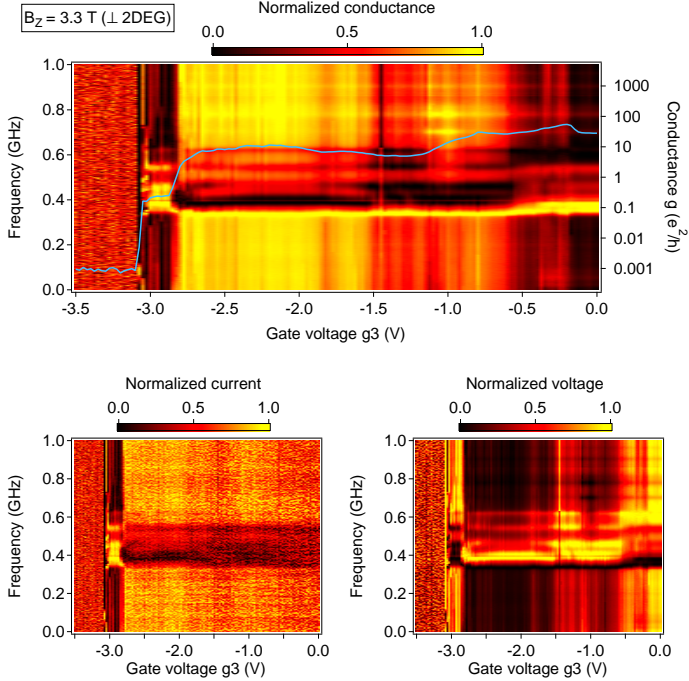


Figure 48: The top panel shows the CEO wire conductance as a function of gate voltage  $g_3$ , recorded at base temperature (with large bias voltage, equiv.  $T \lesssim 4$  K) in a perpendicular (to the 2DEG) magnetic field of 3.3 T. For visibility reasons each vertical trace (horizontal cut at the lowest frequency). In the lower panels, normalized current and voltage data are presented.

In a different cool down we investigated the temperature dependence for these resonances. For orientation, a low and high temperature conductance trace for DW3 are shown in fig. 49a. For the low temperature data the conductance step height  $g_{UW1}$  is  $\approx 1 e^2/h$  as discussed in detail in chapter 5. We proceed to measure the conductance as a function of frequency and temperature for gate positions indicated by the black arrows in fig. 49a. The results are presented in fig. 49c for the lower and fig. 49d for the upper wire. For visibility reasons traces have been shifted, i.e. for each trace we subtract its

conductance measured at 1 MHz (first data point). While the resonances maintain their specific fingerprint at high temperatures, their amplitude is strongly reduced. Only at quite large  $T_R \approx 10$  K we completely lose the response to RF-irradiation and the measured conductance becomes independent of frequency. The temperature at which the signal is lost also depends on the measurement sensitivity (can be increased e.g. by increasing the bias across the wire) and the choice of irradiated RF-power.

In fig. 49e we plot the RF signal size (blue dots), defined as the difference  $g_{\max} - g_{\min}$  for conductance traces as shown in fig. 49c, as a function of refrigerator temperature  $T_R$ . For comparison we additionally plot the CEO wire conductance (black dots), measured under 1 MHz RF-irradiation. As in chapter 5, we observe that upon increasing  $T_R$  the conductance stays constant and starts to increase only above a critical temperature. For the RF-signal size we observe the opposite. The signal is largest at the lowest temperatures and then starts to decay quickly with increasing  $T_R$  above the critical temperature. In order to check whether this low temperature saturation results from RF-heating, we further increase the power to from -45 dBm to -35 dBm and repeat the measurement (data is actually recorded in the same warmup), shown as red dots in fig. 49e. For clarity, this data has been scaled by a factor of 1/2. Corresponding conductance data is shown in gray. We note, though the increased RF-power increases the RF-signal size, the saturated low temperature behavior is the same, i.e. the saturation temperature does not change. Also the conductance data (recorded under 1 MHz RF-irradiation) is identical to the low RF-power data. We conclude that the increase in RF-power does not further increase the conductance. Together this indicates that the saturation is not caused by RF-heating. The same observations hold for the upper wire yet with a different saturation temperature. Finally, we note that the saturation of RF-signal size coincides with the saturation temperature for the conductance step size.

For the sake of completeness we plot the conductance step size as a function of temperature in fig. 49b) i.e. the difference of black data points in f) and e). We find a similar temperature dependent reduced conductance step as for measurements presented in chapter 5.



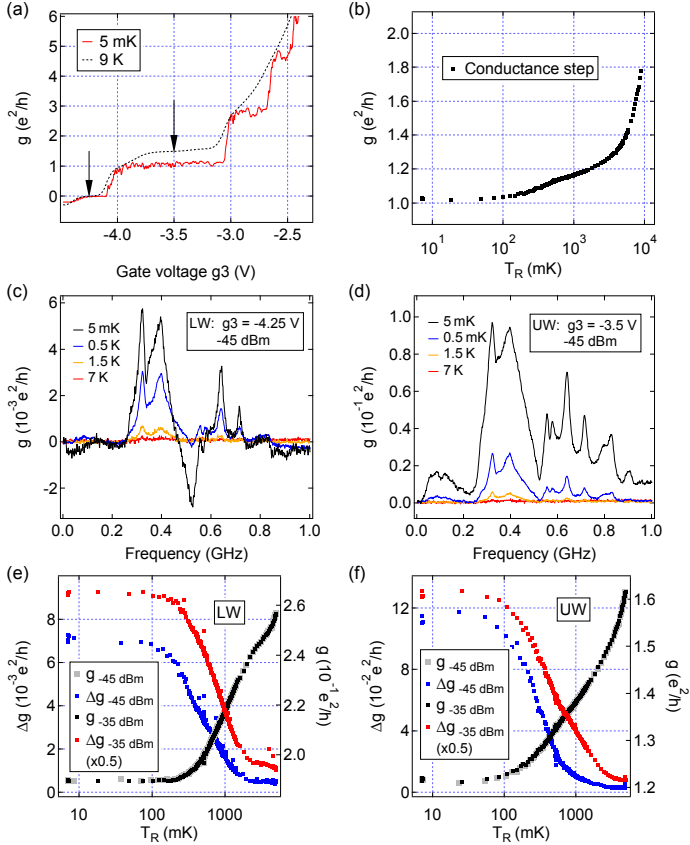


Figure 49: a) CEO wire conductance for temperatures as indicated. Traces are shifted to align  $LW_1$  with  $g = 0$ . b) Conductance step height  $g_{UW1}$ , calculated by subtracting the black data points in e) from the ones in f). c)  $g_{LW}$  as a function of RF frequency for various temperatures. Traces are shifted to align the first data point (low frequency) with  $g = 0$ . RF power and gate voltage  $g_3$  are indicated. d) Same as c) for the UW. e) Signal size, defined as  $g_{\max} - g_{\min}$  from c), versus refrigerator temperature  $T_R$  (blue data). Red data points are recorded at larger RF power (-35 dBm). For the conductance data (black, gray) we plot the lowest frequency point in c) as a function of  $T_R$ . f) Same as e) for the UW.

The outlook on CEO wires in connection with RF-irradiation can be summarized as follows: we find a strong response to RF-irradiation that is observed only when the

system is conducting and the current is carried by edge channels. The amplitude of this response is strongly temperature dependent (suppressed at large  $T_R$ ) and saturates at low temperatures in coincidence with the saturation of reduced conductance steps.

We note that for all CEO wire measurements under RF-irradiation the conductance through the DWs was measured as a function of RF-frequency. As mentioned earlier, the conductance steps for a quantum wire arise only from contact resistance without contribution from the actual ballistic CEO wires. Therefore, the measured conductance might not be very sensitive to changes in the magnetic environment inside the quantum wire. We therefore propose tunnel spectroscopy measurements under RF-irradiation. A mapping of the dispersions via spectroscopy offers highly B-field dependent transport properties as required for RDNMR. In addition, tunnel spectroscopy directly probes the wire rather than the contacts.

## Metastable charge state switching

Intrinsic charge fluctuations as observed in chapter 6 set an upper limit on the T1-time since they are based on electron exchange with the leads which inevitably destroys coherence. The good news is that these fluctuations can be made very slow simply by gate tuning of relevant tunnel barriers. The negative aspect is that slow switching rates also imply slow qubit initialization times.

Seen from another point of view, these intrinsic charge fluctuations in a double quantum dot could be used to study the coupling to a bath (Fermi-reservoirs) in a controlled, gate tunable manner.

The next step for this project is a successful resolution of the Zeeman splitting which then allows for a T1-measurement. At that point one could e.g. measure the T1-time as a function of coupling to the bath as proposed above.

## References

- [1] B. Braunecker, P. Simon, and D. Loss. *Nuclear magnetism and electron order in interacting one-dimensional conductors*. Phys. Rev. B **80**, 165119 (2009).
- [2] A. Yacoby, H. Stormer, N. S. Wingreen, L. N. Pfeiffer, K. W. Baldwin, and K. W. West. *Nonuniversal Conductance Quantization in Quantum Wires*. Phys. Rev. Lett. **77**, 4612 (1996).
- [3] C. Scheller, S. Heizmann, K. Bedner, M. Meschke, J. Pekola, and D. M. Zumbühl. *Miniature Microwave Filters for Thermalization below 10 mK*. (In preparation).
- [4] L. Casparis, M. Meschke, D. Maradan, A. C. Clark, C. P. Scheller, K. K. Schwarzwalder, J. P. Pekola, and D. M. Zumbühl. *Coulomb Blockade Thermometry down to 10 mK and below*. Rev. Sci. Instrum. **83**, 083903 (2012).
- [5] C. P. Scheller, L. N. Pfeiffer, K. W. West, and D. M. Zumbühl. *One dimensional Fabry-Perot Resonances in a ballistic GaAs Quantum Wire*. (In preparation).
- [6] C. P. Scheller, T.-M. Liu, G. Barak, A. Yacoby, L. N. Pfeiffer, K. W. West, and D. M. Zumbühl. *Evidence for Helical Nuclear Spin Order in GaAs Quantum Wires*. (Submitted for publication in Phys. Rev. Lett.).
- [7] D. E. F. Biesinger, C. P. Scheller, B. Braunecker, J. Zimmerman, A. C. Gossard, and D. M. Zumbühl. *Thermally Activated Charge Fluctuations in a Few Electron GaAs Double Quantum Dot*. (In preparation).
- [8] O. M. Auslaender, H. Steinberg, A. Yacoby, Y. Tserkovnyak, B. I. Halperin, K. W. Baldwin, L. N. Pfeiffer, and K. W. West. *Spin-Charge Separation and Localization in One Dimension*. Science **308**, 88 (2005).
- [9] H. Steinberg, O. M. Auslaender, A. Yacoby, J. Qian, G. A. Fiete, Y. Tserkovnyak, B. I. Halperin, K. W. Baldwin, L. N. Pfeiffer, and K. W. West. *Localization transition in a ballistic quantum wire*. Phys. Rev. B **73**, 113307 (2006).

- [10] R. de Picciotto, H. L. Stormer, L. N. Pfeiffer, K. W. Baldwin, and K. W. West. *Four-terminal resistance of a ballistic quantum wire*. Nature **411**, 51 (2001).
- [11] A. Leanhardt, T. Pasquini, M. Saba, A. Schirotzek, Y. Shin, D. Kielpinski, D. Pritchard, and W. Ketterle. *Cooling Bose-Einstein Condensates Below 500 Picokelvin*. Science **301**, 1513 (2003).
- [12] T. A. Knuuttila, J. T. Tuoriniemi, and K. Lefmann. *Relaxation of Polarized Nuclei in Superconducting Rhodium*. Phys. Rev. Lett. **85**, 2573 (2000).
- [13] Brookhaven National Laboratory. *'Perfect' liquid hot enough to be quark soup*. ScienceDaily (2010).
- [14] F. Pobell. *Matter and Methods at Low Temperatures* (Springer, Berlin, Germany, 2007), 3 edition.
- [15] W. Meissner and R. Ochsenfeld. *Ein neuer Effekt bei Eintritt der Supraleitfähigkeit*. Naturwissenschaften **41**, 787 (1933).
- [16] L. Kouwenhoven. *Coupled Quantum Dots as Artificial Molecules*. Science **268**, 1440 (1995).
- [17] M. Kastner. *Artificial Atoms*. Physics Today **46**, 24 (1993).
- [18] D. Zumbühl. *Introduction to Mesoscopic Physics and Quantum Dots*. Lect. Notes Phys. (2008).
- [19] L. P. Kouwenhoven, C. M. Marcus, P. L. McEuen, S. Tarucha, R. M. Westervelt, and N. S. Wingreen. *Electron transport in quantum dots*. Kluwer Series **E345**, 105 (1997).
- [20] J. Elzerman, R. Hanson, L. van Beveren, S. Tarucha, L. Vandersypen, and L. Kouwenhoven. *Semiconductor Few-Electron Quantum Dots as Spin Qubits*. Lect. Notes Phys. **667**, 25 (2005).

- [21] S. Amasha. *Electron Tunneling and Spin Relaxation in a Lateral Quantum Dot*. PhD dissertation, Massachusetts Institute of Technology, Department of Physics (2007).
- [22] E. B. Foxman, P. L. McEuen, U. Meirav, N. S. Wingreen, Y. Meir, P. A. Belk, N. R. Belk, and M. A. Kastner. *Effects of quantum levels on transport through a Coulomb island*. Phys. Rev. B **47**, 10020 (1993).
- [23] W. van der Wiel, S. D. Franceschi, J. Elzerman, T. Fujisawa, S. Tarucha, and L. Kouwenhoven. *Electron transport through double quantum dots*. Rev. Mod. Phys. **75**, 1 (2003).
- [24] W. Desrat, D. K. Maude, M. Potemski, J. C. Portal, Z. R. Wasilewski, and G. Hill. *Resistively Detected Nuclear Magnetic Resonance in the Quantum Hall Regime: Possible Evidence for a Skyrme Crystal*. Phys. Rev. Lett. **88**, 256807 (2002).
- [25] M. Paget, G. Lampel, V. Sapoval, and V. I. Safarov. *Low field electron-nuclear spin coupling in gallium arsenide under optical pumping conditions*. Phys. Rev. B **15**, 5780 (1977).
- [26] G. Armstrong, A. S. Greenberg, and J. R. Sites. *Very low temperature thermal conductivity and optical properties of Stycast 1266 epoxy*. Rev. Sci. Instr. **49**, 345 (1978).
- [27] D. M. Pozar. *Microwave Engineering* (John Wiley & sons Inc., 2005), third edition.
- [28] M. Dobers, K. v. Klitzing, J. Schneider, G. Weimann, and K. Ploog. *Electrical Detection of Nuclear Magnetic Resonance in GaAs – Al<sub>x</sub>Ga<sub>1-x</sub>As Heterostructures*. Phys. Rev. Lett. **61**, 1650 (1988).
- [29] G. Gervais, H. L. Stormer, D. C. Tsui, P. L. Kuhns, W. G. Moulton, A. P. Reyes, L. N. Pfeiffer, K. W. Baldwin, and K. W. West. *Evidence for Skyrmion*

- Crystallization from NMR Relaxation Experiments*. Phys. Rev. Lett. **94**, 196803 (2005).
- [30] S. Kronmüller, W. Dietsche, K. v. Klitzing, G. Denninger, W. Wegscheider, and M. Bichler. *New Type of Electron Nuclear-Spin Interaction from Resistively Detected NMR in the Fractional Quantum Hall Effect Regime*. Phys. Rev. Lett. **82**, 4070 (1999).
- [31] O. Stern, N. Freytag, A. Fay, W. Dietsche, J. H. Smet, K. von Klitzing, D. Schuh, and W. Wegscheider. *NMR study of the electron spin polarization in the fractional quantum Hall effect of a single quantum well: Spectroscopic evidence for domain formation*. Phys. Rev. B **70**, 075318 (2004).
- [32] L. A. Tracy, J. P. Eisenstein, L. N. Pfeiffer, and K. W. West. *Resistively detected NMR in a two-dimensional electron system near  $\nu = 1$ : Clues to the origin of the dispersive lineshape*. Phys. Rev. B **73**, 121306(R) (2006).
- [33] *CRC Handbook of Chemistry and Physics* (Internet Version, 2012-2013).
- [34] I. P. Radu, J. B. Miller, C. M. Marcus, M. A. Kastner, L. N. Pfeiffer, and K. W. West. *Quasi-Particle Properties from Tunneling in the  $\nu = 5/2$  Fractional Quantum Hall State*. Science **320**, 899 (2008).
- [35] N. Samkharadze, A. Kumar, M. J. Manfra, L. N. Pfeiffer, K. W. West, and G. A. Cs athy. *Integrated electronic transport and thermometry at milliKelvin temperatures and in strong magnetic fields*. Rev. Sci. Instr. **82**, 053902 (2011).
- [36] M. Dolev, M. Heiblum, V. Umansky, A. Stern, and D. Mahalu. *Observation of a quarter of an electron charge at the  $\nu = 5/2$  quantum Hall state*. Nature **452**, 829 (2008).
- [37] P. L. Gammel, D. J. Bishop, J. P. Eisenstein, J. H. English, A. C. Gossard, R. Ruel, and H. L. Stormer. *Ultralow-temperature behavior of the  $\nu = 5/2$  fractional quantum hall effect*. Phys. Rev. B **38**, 10128 (1988).

- [38] J. S. Xia, E. D. Adams, V. Shvarts, W. Pan, H. L. Stormer, and D. C. Tsui. *Ultra-low-temperature cooling of two-dimensional electron gas*. Physica B **280**, 491 (2000).
- [39] W. Pan, J. S. Xia, V. Shvarts, D. E. Adams, H. L. Stormer, D. C. Tsui, L. N. Pfeiffer, K. W. Baldwin, and K. W. West. *Exact Quantization of the Even-Denominator Fractional Quantum Hall State at  $\nu = 5/2$  Landau Level Filling Factor*. Phys. Rev. Lett. **83**, 3530 (1999).
- [40] B. Braunecker, P. Simon, and D. Loss. *Nuclear Magnetism and Electronic Order in  $^{13}\text{C}$  Nanotubes*. Phys. Rev. Lett. **102**, 116403 (2009).
- [41] P. Simon and D. Loss. *Nuclear Spin Ferromagnetic Phase Transition in an Interacting Two Dimensional Electron Gas*. Phys. Rev. Lett. **98**, 156401 (2007).
- [42] P. Simon, B. Braunecker, and D. Loss. *Magnetic ordering of nuclear spins in an interacting two-dimensional electron gas*. Phys. Rev. B **77**, 045108 (2008).
- [43] J. P. Pekola, V. F. Maisi, S. Kafanov, N. Chekurov, A. Kemppinen, Y. A. Pashkin, O. P. Saira, M. Möttönen, and J. S. Tsai. *Environment-Assisted Tunneling as an Origin of the Dynes Density of States*. Phys. Rev. Lett. **105**, 026803 (2010).
- [44] O. P. Saira, A. Kemppinen, V. F. Maisi, and J. P. Pekola. *Vanishing quasiparticle density in a hybrid Al/Cu/Al single-electron transistor*. Phys. Rev. B **85**, 012504 (2012).
- [45] J. M. Hergenrother, J. G. Lu, M. T. Tuominen, D. C. Ralph, and M. Tinkham. *Photon-activated switch behavior in the single-electron transistor with a superconducting island*. Phys. Rev. B **51**, 9407 (1995).
- [46] J. M. Martinis, M. H. Devoret, and J. Clarke. *Experimental tests for the quantum behavior of a macroscopic degree of freedom: The phase difference across a Josephson junction*. Phys. Rev. B **35**, 4682 (1987).

- [47] A. Lukashenko and A. Ustinov. *Improved powder filters for qubit measurements*. Rev. Sci. Instrum. **79**, 014701 (2008).
- [48] F. P. Milliken, J. R. Rozen, G. A. Keefe, and R. H. Koch. *50 $\Omega$  characteristic impedance low-pass metal powder filters*. Rev. Sci. Instrum. **78**, 024701 (2007).
- [49] A. Fukushima, A. Sato, A. Iwasa, Y. Nakamura, T. Komatsuzaki, and Y. Sakamoto. *Attenuation of Microwave Filters for Single-Electron Tunneling Experiments*. IEEE Trans. Instrum. Meas. **46**, 289 (1997).
- [50] H. le Sueur and P. Joyez. *Microfabricated electromagnetic filters for millikelvin experiments*. Rev. Sci. Instrum. **77**, 115102 (2006).
- [51] D. Vion, P. F. Orfila, P. Joyez, D. Esteve, and M. H. Devoret. *Miniature electrical filters for single electron devices*. J. Appl. Phys. **77**, 2519 (1995).
- [52] H. Courtois, O. Buisson, J. Chaussy, and B. Pannetier. *Miniature low temperature high frequency filters for single electronics*. Rev. Sci. Instrum. **66**, 3465 (1995).
- [53] L. Longobardi, D. A. Bennett, V. Patel, W. Chen, and J. E. Lukens. *Microstrip filters for measurement and control of superconducting qubits*. Rev. Sci. Instrum. **84**, 014706 (2013).
- [54] A. B. Zorin. *The thermocox cable as the microwave frequency filter for single electron circuits*. Rev. Sci. Instr. **66**, 4296 (1995).
- [55] D. C. Glatthli, P. Jacques, A. Kumar, P. Pari, and L. Saminadayar. *A noise detection scheme with 10 mK noise temperature resolution for semiconductor single electron tunneling devices*. J. Appl. Phys. **81**, 7350 (1997).
- [56] H. Bluhm and A. Moler. *Dissipative cryogenic filters with zero dc resistance*. Rev. Sci. Instrum. **79**, 014703 (2008).
- [57] L. Spietz, J. Teufel, and R. J. Schoelkopf. *A Twisted Pair Cryogenic Filter*. arXiv:cond-mat/0601316v1 (2006).



- [58] I. Jin, A. Amar, and F. C. Wellstood. *Distributed microwave damping filter for superconducting quantum interference devices*. Appl. Phys. Lett. **70**, 2186 (1997).
- [59] D. H. Slichter, O. Naaman, and I. Siddiqi. *Millikelvin thermal and electrical performance of lossy transmission line filters*. Appl. Phys. Lett. **94**, 192508 (2009).
- [60] K. Bladh, D. Gunnarsson, E. Hürfeld, S. Devi, C. Kristoffersson, B. Smålander, S. Pehrson, T. Claeson, P. Delsing, and M. Taslavkov. *Comparison of cryogenic filters for use in single electronics experiments*. Rev. Sci. Instrum. **74**, 1323 (2003).
- [61] Silver epoxy E4110, available at EPO–TEK.
- [62] Pacific Aerospace and Electronics, [www.pacaero.com](http://www.pacaero.com).
- [63] R. M. Potok, I. G. Rau, H. Shtrikman, Y. Oreg, and D. Goldhaber-Gordon. *Observation of the two-channel Kondo effect*. Nature **446**, 167 (2007).
- [64] I. Karakurt, V. J. Goldman, J. Liu, and A. Zaslavsky. *Absence of Compressible Edge Channel Rings in Quantum Antidots*. Phys. Rev. Lett. **87**, 146801 (2001).
- [65] A. Mavalankar, S. J. Chorley, J. Griffiths, G. A. C. Jones, I. Farrer, D. A. Ritchie, and C. G. Smith. *A non-invasive electron thermometer based on charge sensing of a quantum dot*. Appl. Phys. Lett. **103**, 133116 (2013).
- [66] P. Torresani, M. J. Martínez-Pérez, S. Gasparinetti, J. Renard, G. Biasiol, L. Sorba, F. Giazotto, and S. D. Franceschi. *Nongalvanic primary thermometry of a two-dimensional electron gas*. Phys. Rev. B **88**, 245304 (2013).
- [67] A. Rossi, T. Ferrus, and D. A. Williams. *Electron temperature in electrically isolated Si double quantum dots*. Appl. Phys. Lett. **100**, 133503 (2012).
- [68] D. M. Zumbühl, C. M. Marcus, M. P. Hanson, and A. C. Gossard. *Asymmetry of Nonlinear Transport and Electron Interactions in Quantum Dots*. Phys. Rev. Lett. **96**, 206802 (2006).

- [69] H. van Houten, C. W. J. Beenakker, and A. A. M. Staring. *Coulomb Blockade Oscillations in Semiconductor Nanostructures* (Published in Single Charge Tunneling, edited by H. Grabert and M. H. Devoret, NATO ASI Series B294, Plenum, New York, 1992).
- [70] M. A. Kastner. *The single-electron transistor*. Rev. Mod. Phys. **64**, 849 (1992).
- [71] M. Meschke, J. P. Pekola, F. Gay, R. E. Rapp, and H. Godfrin. *Electron Thermalization in Metallic Islands Probed by Coulomb Blockade Thermometry*. J. Low Temp. Phys. **134**, 1119 (2004).
- [72] J. P. Pekola, K. P. Hirvi, J. P. Kauppinen, and M. A. Paalanen. *Thermometry by Arrays of Tunnel Junctions*. Phys. Rev. Lett. **73**, 2903 (1994).
- [73] A. V. Feshchenko, M. Meschke, D. Gunnarsson, M. Prunnila, L. Roschier, J. S. Penttilä, and J. P. Pekola. *Primary Thermometry in the Intermediate Coulomb Blockade Regime*. J. Low Temp. Phys. **173**, 36 (2013).
- [74] S. Farhangfar, K. P. Hirvi, J. P. Kauppinen, J. P. Pekola, J. J. Toppari, D. V. Averin, and A. N. Korotkov. *One dimensional arrays and solitary tunnel junctions in the weak coulomb blockade regime: CBT thermometry*. J. Low Temp. Phys. **108**, 191 (1997).
- [75] M. Meschke, J. Engert, D. Heyer, and J. P. Pekola. *Comparison of Coulomb Blockade Thermometers with the International Temperature Scale PLTS-2000*. Int. J. Thermophys. **32**, 1378 (2011).
- [76] Insulated copper wire CUL 200/0.1, available at distrelec, [www.distrelec.ch](http://www.distrelec.ch).
- [77] G. K. White and P. J. Meeson. *Experimental techniques in low-temperature physics* (Oxford University Press, 2002).
- [78] R. Hanson, L. Kouwenhoven, J. Petta, S. Tarucha, and L. Vandersypen. *Spins in few-electron quantum dots*. Rev. Mod. Phys. **79**, 1217 (2007).

- [79] C. Nayak, S. Simon, A. Stern, M. Freedman, and S. D. Sarma. *Non-Abelian anyons and topological quantum computation*. Rev. Mod. Phys. **80**, 1083 (2008).
- [80] A. Stern. *Non-Abelian states of matter*. Nature **464**, 187 (2010).
- [81] O. Lounasmaa. *Experimental Principles and Methods Below 1K*. Academic, London (1974).
- [82] G. Pickett. *Microkelvin physics*. Rep. Prog. Phys. **51**, 1295 (1988).
- [83] J. Huang, J. Xia, D. Tsui, L. Pfeiffer, and K. West. *Disappearance of Metal-Like Behavior in GaAs Two-Dimensional Holes below 30 mK*. Phys. Rev. Lett. **98**, 226801 (2007).
- [84] A. Clark, K. Schwarzwälder, T. Bandi, D. Maradan, and D. Zumbühl. *Method for cooling nanostructures to microkelvin temperatures*. Rev. Sci. Instr. **81**, 103904 (2010).
- [85] O. M. Auslaender, A. Yacoby, R. de Picciotto, K. W. Baldwin, L. N. Pfeiffer, and K. W. West. *Tunneling Spectroscopy of the Elementary Excitations on a One-Dimensional Wire*. Science **295**, 825 (2002).
- [86] J. Voit. *One-dimensional Fermi liquids*. Rep. Prog. Phys. **57**, 977 (1994).
- [87] F. Bloch. *Bremsvermögen von Atomen mit mehreren Elektronen*. Z. Phys. **81**, 363 (1933).
- [88] S. Tomonaga. *Remarks on Bloch's Method of Sound Waves applied to Many-Fermion Problems*. P.T.P **5**, 544 (1950).
- [89] J. M. Luttinger. *An Exactly Soluble Model of a Many-Fermion System*. J. Math. Phys. **4**, 1154 (1963).
- [90] D. C. Mattis and E. H. Lieb. *Exact Solution of a Many-Fermion System and Its Associated Boson Field*. J. Math. Phys. **6**, 304 (1965).

- [91] V. V. Deshpande, M. Bockrath, L. I. Glazman, and A. Yacoby. *Electron liquids and solids in one dimension*. Nature **464**, 209 (2010).
- [92] Y. Jompol, C. J. B. Ford, J. P. Griffiths, I. Farrer, G. A. C. Jones, D. Anderson, D. A. Ritchie, T. W. Silk, and A. J. Schofield. *Probing Spin-Charge Separation in a Tomonaga-Luttinger Liquid*. Science **325**, 597 (2009).
- [93] M. Bockrath, D. H. Cobden, J. Lu, A. G. Rinzler, R. E. Smalley, L. Balents, and P. L. McEuen. *Luttinger-liquid behaviour in carbon nano tubes*. Nature **397**, 598 (1999).
- [94] H. Ishii, H. Kataura, H. Shiozawa, H. Yoshioka, H. Otsubo, Y. Takayama, T. Miyahara, S. Suzuki, Y. Achiba, M. Nakatake, T. Narimura, M. Higashiguchi, K. Shimada, H. Namatame, and M. Taniguchi. *Direct observation of Tomonaga-Luttinger-liquid state in carbon nanotubes at low temperatures*. Nature **426**, 540 (2003).
- [95] Y. Tserkovnyak, B. I. Halperin, O. M. Auslaender, and A. Yacoby. *Finite-Size Effects in Tunneling between Parallel Quantum Wires*. Phys. Rev. Lett. **89**, 136805 (2002).
- [96] Y. Tserkovnyak, B. I. Halperin, O. M. Auslaender, and A. Yacoby. *Interference and zero-bias anomaly in tunneling between Luttinger-liquid wires*. Phys. Rev. B **68**, 125312 (2003).
- [97] A. M. Chang and L. N. Pfeiffer. *Observation of Chiral Luttinger Behavior in Electron Tunneling into Fractional Quantum Hall Edges*. Phys. Rev. Lett. **77**, 2538 (1996).
- [98] M. Grayson, D. C. Tsui, L. N. Pfeiffer, K. W. West, and A. M. Chang. *Continuum of Chiral Luttinger Liquids at the Fractional Quantum Hall Edge*. Phys. Rev. Lett. **80**, 1062 (1998).

- [99] M. Grayson, D. C. Tsui, L. N. Pfeiffer, K. W. West, and A. M. Chang. *Resonant Tunneling into a Biased Fractional Quantum Hall Edge*. Phys. Rev. Lett. **86**, 2645 (2001).
- [100] S. Hofferberth, I. Lesanovsky, B. Fischer, T. Schumm, and J. Schmiedmayer. *Non-equilibrium coherence dynamics in one-dimensional Bose gases*. Nature **449**, 324 (2007).
- [101] S. Hofferberth, I. Lesanovsky, T. Schumm, A. Imambekov, V. Gritsev, E. Demler, and J. Schmiedmayer. *Probing quantum and thermal noise in an interacting many-body system*. Nat. Phys. **4**, 489 (2008).
- [102] O. M. Auslaender, A. Yacoby, R. de Picciotto, K. W. Baldwin, L. N. Pfeiffer, and K. W. West. *Experimental Evidence for Resonant Tunneling in a Luttinger Liquid*. Phys. Rev. Lett. **84**, 1764 (2000).
- [103] M. J. Biercuk, N. Mason, J. Martin, A. Yacoby, and C. M. Marcus. *Anomalous Conductance Quantization in Carbon Nanotubes*. Phys. Rev. Lett. **94**, 026801 (2005).
- [104] R. Landauer. *Spatial variation of currents and fields due to localized scatterers in metallic conduction*. IBM J. Res. Dev **1**, 223 (1957).
- [105] M. Büttiker, Y. Imry, R. Landauer, and S. Pinhas. *Generalized many-channel conductance formula with application to small rings*. Phys. Rev. B **31**, 6207 (1985).
- [106] B. J. van Wees, H. van Houten, C. W. J. Beenakker, J. G. Williamson, L. P. Kouwenhoven, D. van der Marel, and C. T. Foxon. *Quantized Conductance of Point Contacts in a Two-Dimensional Electron Gas*. Phys. Rev. Lett **60**, 848 (1988).
- [107] D. A. Wharam, T. J. Thornton, R. Newbury, M. Pepper, H. Ahmed, J. E. F. Frost, D. G. Hasko, D. C. Peacock, D. A. Ritchie, and G. A. C. Jones. *One-*

- dimensional transport and the quantisation of the ballistic resistance.* J. Phys. C **21**, L209 (1988).
- [108] W. Apel and T. M. Rice. *Combined effect of disorder and interaction on the conductance of a one-dimensional fermion system.* Phys. Rev. B **26**, 7063 (1982).
- [109] C. L. Kane and M. P. A. Fisher. *Transport in a One-Channel Luttinger Liquid.* Phys. Rev. Lett. **68**, 665 (1992).
- [110] C. L. Kane and M. P. A. Fisher. *Transmission through barriers and resonant tunneling in an interacting one-dimensional electron gas.* Phys. Rev. B **45**, 15233 (1992).
- [111] D. L. Maslov and M. Stone. *Landauer conductance of Luttinger liquids with leads.* Phys. Rev. B **52**, R5539 (1995).
- [112] I. Safi and H. J. Schulz. *Transport in an inhomogeneous interacting one-dimensional system.* Phys. Rev. B **52**, R17040 (1995).
- [113] V. V. Ponomarenko. *Renormalization of the one-dimensional conductance in the Luttinger-liquid model.* Phys. Rev. B **52**, R8666 (1995).
- [114] D. L. Maslov. *Transport through dirty Luttinger liquids connected to reservoirs.* Phys. Rev. B **52**, R14368 (1995).
- [115] S. Tarucha, T. Honda, and T. Saku. *Reduction of quantized conductance at low temperatures observed in 2 to 10  $\mu\text{m}$  long quantum wires.* Solid State Commun. **94**, 413 (1995).
- [116] E. Levy, A. Tsukernik, M. Karpovskii, A. Palevski, B. Dwir, E. Pelucchi, A. Rudra, E. Kapon, and Y. Oreg. *Luttinger-Liquid Behavior in Weakly Disordered Quantum Wires.* Phys. Rev. Lett. **97**, 196802 (2006).
- [117] R. Peierls. *Quantum Theory of Solids* (Oxford: Oxford University Press, 1955).

- [118] B. Braunecker, G. I. Japaridze, J. Klinovaja, and D. Loss. *Spin-selective Peierls transition in interacting one-dimensional conductors with spin-orbit interaction*. Phys. Rev. B **82**, 045127 (2010).
- [119] M. Governale, D. Boese, U. Zülicke, and C. Schroll. *Filtering spin with tunnel-coupled electron wave guides*. Phys. Rev. B **65**, 140403(R) (2002).
- [120] M. Governale, D. Boese, U. Zülicke, and C. Schroll. *Antisymmetric Spin Filtering in One-Dimensional Electron Systems with Uniform Spin-Orbit Coupling*. Phys. Rev. Lett. **90**, 256601 (2003).
- [121] C. H. L. Quay, T. L. Hughes, J. A. Sulpizio, L. N. Pfeiffer, K. W. Baldwin, K. W. West, D. Goldhaber-Gordon, and R. de Picciotto. *Observation of a one-dimensional spin-orbit gap in a quantum wire*. Nat. Phys. **6**, 336 (2010).
- [122] D. J. Reilly, G. R. Facer, A. S. Dzurak, R. G. Clark, P. J. Stiles, R. G. Clark, A. R. Hamilton, J. L. O'Brian, N. E. Lumpkin, L. N. Pfeiffer, and K. W. West. *Conductance through contact barriers of a finite-length quantum wire*. Phys. Rev. B **63**, 121311(R) (2001).
- [123] A. Yacoby, H. L. Stormer, K. W. Baldwin, L. N. Pfeiffer, and K. W. West. *Magneto Transport Spectroscopy on a Quantum Wire*. Solid State Commun. **101**, 77 (1997).
- [124] L. Pfeiffer, K. W. West, H. L. Stormer, J. P. Eisenstein, K. W. Baldwin, D. Gershoni, and J. Spector. *Formation of a high quality two-dimensional electron gas on cleaved GaAs*. Appl. Phys. Lett. **56**, 1697 (1990).
- [125] L. Pfeiffer, H. L. Stormer, K. W. Baldwin, K. W. West, A. R. Goñi, A. Pinczuk, R. C. Ashoori, M. M. Dignam, and W. Wegscheider. *Cleaved edge overgrowth for quantum wire fabrication*. J. Cryst. Growth. **127**, 849 (1993).
- [126] W. Wegscheider, W. Wang, L. N. Pfeiffer, K. W. West, H. L. Stormer, and K. W. Baldwin. *High-mobility transport along single quasi-1D quantum wires formed by cleaved edge overgrowth*. Solid State Electron. **37**, 547 (1994).

- [127] R. de Picciotto, H. L. Stormer, A. Yacoby, L. N. Pfeiffer, K. W. Baldwin, and K. W. West. *2D-1D Coupling in Cleaved Edge Overgrowth*. Phys. Rev. Lett. **85**, 1730 (2000).
- [128] J. P. Jackson. *Classical Electrodynamics* (John Wiley & Sons, Inc., New Jersey, USA, 1991), 3rd edition.
- [129] E. Noether. *Invariante Variationsprobleme*. Nachr. D. König. Gesellsch. D. Wiss. Zu Göttingen, Math-phys. Klasse 235 (1918).
- [130] D. Boese, M. Governale, A. Rosch, and U. Zülicke. *Mesoscopic effects in tunneling between parallel wires*. Phys. Rev. B **64**, 085315 (2001).
- [131] K. F. Berggren, T. J. Thornton, D. J. Newson, and M. Pepper. *Magnetic Depopulation of 1D Subbands in a Narrow 2D Electron Gas in a GaAs:AlGaAs Heterojunction*. Phys. Rev. Lett. **57**, 1769 (1986).
- [132] W. Liang, M. Bockrath, D. Bozovic, J. H. Hafner, M. Tinkham, and H. Park. *Fabry-Perot interference in a nanotube electron waveguide*. Nature **411**, 665 (2001).
- [133] A. F. Young and P. Kim. *Quantum interference and Klein tunneling in graphene heterojunctions*. Nat. Phys. **5**, 222 (2009).
- [134] N. Ofek, A. Bid, M. Heiblum, A. Stern, V. Umansky, and D. Mahalu. *Role of interactions in an electronic Fabry-Perot interferometer operating in the quantum Hall effect regime*. PNAS **107**, 5276 (2010).
- [135] D. T. McClure, W. Chang, C. M. Marcus, L. N. Pfeiffer, and K. W. West. *Fabry-Perot Interferometry with Fractional Charges*. Phys. Rev. Lett. **108**, 256804 (2012).
- [136] C. W. J. Beenakker and H. van Houten. in *Solid State Physics*, edited by H. Ehrenreich and D. Turnbull, Semiconductor Heterostructures and Nanostructures (Academic Press, New York (1991)).



- [137] F. D. M. Haldane. *Luttinger liquid theory of one-dimensional quantum fluids: I. Properties of the Luttinger model and their extension to the general 1D interacting spinless Fermi gas*. J. Phys. C **14**, 2585 (1981).
- [138] H. W. C. Postma, T. Teepen, Z. Yao, M. Grifoni, and C. Dekker. *Carbon Nanotube Single-Electron Transistors at Room Temperature*. Science **293**, 76 (2001).
- [139] H. Steinberg, G. Barak, A. Yacoby, L. N. Pfeiffer, K. W. West, B. I. Halperin, and K. L. Hur. *Charge fractionalization in quantum wires*. Nat. Phys. **4**, 116 (2008).
- [140] G. Barak, H. Steinberg, L. Pfeiffer, K. West, L. Glazman, F. Oppen, and A. Yacoby. *Interacting electrons in one dimension beyond the Luttinger-liquid limit*. Nat. Phys. **6**, 489 (2010).
- [141] Y. Oreg and A. M. Finkel'stein. *dc transport in wires*. Phys. Rev. B **54**, R14265 (1996).
- [142] K. J. Thomas, J. T. Nicholls, M. Y. Simmons, M. Pepper, D. R. Mace, and D. A. Ritchie. *Tunneling Spectroscopy of the Elementary Excitations on a One-Dimensional Wire*. Phys. Rev. Lett. **77**, 135 (1996).
- [143] Y. Tserkovnyak. Private communication.
- [144]  $\ell_{2D-1D} \propto T^{-p_1}$  and  $\ell_{BS} \propto T^{p_2}$ , with  $0 < p_{1,2} < 1$ .
- [145] K. A. Matveev. *Conductance of a Quantum Wire in the Wigner-Crystal Regime*. Phys. Rev. Lett. **92**, 106801 (2004).
- [146] K. A. Matveev. *Conductance of a quantum wire at low electron density*. Phys. Rev. B **70**, 245319 (2004).
- [147] T. Meng and D. Loss. *Helical nuclear spin order in two-subband quantum wires*. Phys. Rev. B **87**, 235427 (2013).

- [148] D. Loss and D. P. DiVincenzo. *Quantum computation with quantum dots*. Phys. Rev. A **57**, 120 (1998).
- [149] J. Petta, A. Johnson, J. Taylor, E. Laird, and A. Yacoby. *Coherent Manipulation of Coupled Electron Spins in Semiconductor Quantum Dots*. Science **309**, 2180 (2005).
- [150] F. Koppens, K. Nowack, and L. Vandersypen. *Spin Echo of a Single Electron Spin in a Quantum Dot*. Phys. Rev. Lett. **100**, 236802 (2008).
- [151] S. Foletti, H. Bluhm, D. Mahalu, V. Umansky, and A. Yacoby. *Universal quantum control of two-electron spin quantum bits using dynamic nuclear polarization*. Nat. Phys. **5**, 903 (2009).
- [152] K. Nowack, F. Koppens, Y. Nazarov, and L. Vandersypen. *Coherent Control of a Single Electron Spin with Electric Fields*. Science **318**, 1430 (2007).
- [153] C. Barthel, D. Reilly, C. Marcus, M. Hanson, and A. Gossard. *Rapid Single-Shot Measurement of a Singlet-Triplet Qubit*. Phys. Rev. Lett. **103**, 160503 (2009).
- [154] V. Golovach, A. Khaetskii, and D. Loss. *Phonon-Induced Decay of the Electron Spin in Quantum Dots*. Phys. Rev. Lett. **93**, 016601 (2004).
- [155] S. Amasha, K. MacLean, I. Radu, D. Zumbühl, M. Kastner, M. Hanson, and A. Gossard. *Electrical Control of Spin Relaxation in a Quantum Dot*. Phys. Rev. Lett. **100**, 046803 (2008).
- [156] H. Bluhm, S. Foletti, I. Neder, M. Rudner, D. Mahalu, V. Umansky, and A. Yacoby. *Dephasing time of GaAs electron-spin qubits coupled to a nuclear bath exceeding 200  $\mu$ s*. Nat. Phys. **7**, 109 (2010).
- [157] M. Field, C. Smith, M. Pepper, D. Ritchie, J. Frost, G. Jones, and D. Hasko. *Measurements of Coulomb blockade with a noninvasive voltage probe*. Phys. Rev. Lett. **70**, 1311 (1993).

- [158] C. Barhel, M. Kjærgaard, J. Medford, M. Stopa, C. Marcus, M. Hanson, and A. Gossard. *Fast sensing of double-dot charge arrangement and spin state with a radio-frequency sensor quantum dot*. Phys. Rev. B **81**, 161308(R) (2010).
- [159] J. Elzerman, R. Hanson, L. W. van Beveren, B. Witkamp, L. Vandersypen, and L. Kouwenhoven. *Single-shot read-out of an individual electron spin in a quantum dot*. Nature **430**, 431 (2004).
- [160] T. Fujisawa, T. Oosterkamp, W. van der Wiel, B. Broer, R. Aguado, S. Tarucha, and L. Kouwenhoven. *Spontaneous Emission Spectrum in Double Quantum Dot Devices*. Science **282**, 932 (1998).
- [161] D. Harbusch, D. Taubert, H. Tranitz, W. Wegscheider, and S. Ludwig. *Phonon-Mediated versus Coulombic Backaction in Quantum Dot Circuits*. Phys. Rev. Lett. **104**, 196801 (2010).
- [162] D. Taubert, M. Pioro-Ladrière, D. Schrör, D. Harbusch, A. Sachrajda, and S. Ludwig. *Telegraph Noise in Coupled Quantum Dot Circuits Induced by a Quantum Point Contact*. Phys. Rev. Lett **100**, 176805 (2008).
- [163] P. Roulleau, S. Baer, T. Choi, F. Molitor, J. Güttinger, T. Müller, S. Dröscher, K. Ensslin, and T. Ihn. *Coherent electron-phonon coupling in tailored quantum systems*. Nat. Comm. **2**, 239 (2011).
- [164] M. Shulman, O. Dial, S. Harvey, H. Bluhm, V. Umansky, and A. Yacoby. *Demonstration of Entanglement of Electrostatically Coupled Singlet-Triplet Qubits*. Science **336**, 202 (2012).

## List of Figures

1	Mutual inductance of CMN thermometer versus temperature . . . . .	12
2	CMN temperature versus mixing chamber temperature . . . . .	13
3	Schematic of a lateral quantum dot . . . . .	14
4	Schematic of a differential conductance trace through a single quantum dot at zero source-drain bias . . . . .	15
5	Transport through a QD at zero and finite source-drain bias . . . . .	17
6	Charge stability diagram for a double quantum dot with and without interdot coupling . . . . .	20
7	DQD energy level diagram in the vicinity of the (0,1)-(1,0) zero detuning line . . . . .	21
8	NMR coil and HF thermalizing stages . . . . .	26
9	(a) NMR resonance condition . . . . .	
	(b) Fast frequency scans . . . . .	
	(c) Quadrupolar splitting for $^{75}\text{As}$ . . . . .	28
10	(a) Observed NMR resonances at 3.75 T . . . . .	
	(b) Gyromagnetic ratio for the resonances in (a) . . . . .	29
11	Room temperature attenuation characteristics for various microwave filters	33
12	Electron temperature versus mixing chamber temperature, measured with a GaAs quantum dot . . . . .	36
13	Electron base temperature with and without microwave filters . . . . .	39
14	Electron temperature versus mixing chamber temperature, measured with metallic coulomb blockade thermometers . . . . .	40

15	Measured room temperature attenuation characteristics for a single layer microwave filter (no interlayer coupling) with $z = 1.51$ m of copper wire (red data). A theory curve using eq. 11 and the parameters from Tab. 1, is shown as dotted, black curve. In dashed grey, a standard first order low-pass filter ( $R_0 = R_{\text{tot}}z$ and $C_0 = Cz$ from theory curve) is shown for comparison. . . . .	44
16	Layout of novel nanosample microkelvin refrigerator and CBT array . . .	49
17	CBT normalized differential conductance $g/g_T$ versus source-drain dc bias $V_{SD}$ for various NR temperatures . . . . .	51
18	CBT electron temperature $T_{CBT}$ versus NR temperature . . . . .	54
19	(a) Nuclear spins in the cross section of a 1D conductor . . . . .	
	(b) Sketch of the RKKY interaction . . . . .	64
20	(a) Electronic dispersion and nuclear spin helix . . . . .	
	(b) Regular Peierls transition for comparison . . . . .	65
21	Reduced conductance step height in a CEO wire . . . . .	67
22	First mode in a CEO quantum wire . . . . .	68
23	CEO wire schematic and coordinate system . . . . .	71
24	Conductance as a function of top gate voltage for a GaAs CEO double quantum wire . . . . .	72
25	2DEG density extraction before and after LED illumination by means of quantum hall measurements. . . . .	74
26	CEO wire conductance as a function of top gate voltage in an external magnetic field applied along the wire . . . . .	76
27	(a) Sample schematic with adjacent double wires DW3 and DW4 . . . . .	
	(b) Simulated conductance trace for DW3 and DW4 . . . . .	
	(c),(d) Calculated conductance of the combined DW system in the diffusive (c) and ballistic limit (d) . . . . .	78

28	Measured ballistic addition of two double wire systems connected in series	80
29	CEO wire conductance in the pinch off regime showing coulomb peaks	81
30	(a) Coulomb diamonds in the CEO wire pinch off regime	
	(b) Charge transition points as a function electron number in the quantum dot	82
31	(a) Sketch of the DW dispersions for zero magnetic field and rescaled effective electron mass.	
	(b) Resonant tunneling between left movers in UW and LW	
	(c) Resonant tunneling between right movers in UW and left movers in the LW	84
32	Gating scheme for subsequent tunneling spectroscopy measurements	85
33	(a) 2 terminal conductance trace for DW3	
	(b) Tunneling spectroscopy for DW3 as a function of top gate and perpendicular magnetic field	87
34	Upper and lower wire electron density as a function of top gate voltage.	88
35	(a) Checkerboard pattern for the differential tunneling current versus gate voltage in the low B-field regime.	
	(b) Various line cuts from (a) showing clear oscillations in the differential tunneling current	90
36	Reconstructed lower wire density from Fabry-Perot resonances versus spectroscopically gained data	93
37	Fabry-Perot resonances in the UW	95
38	Double wire mode structure	99
39	Temperature effects	101
40	Bias and B-field dependence	103
41	Density dependence	105

42	(a) SEM picture a DQD similar to the one used in the experiment . . . . .	
	(b) DQD (0,0)-(1,1) charge transition point . . . . .	
	(c) DQD charge stability diagram . . . . .	111
43	(a) Averaged real-time data at the (0,0)-(1,1) transition point . . . . .	
	(b) Standard deviation for the real-time data in (a) . . . . .	113
44	(a) Tunnel rate from state (0,1) to (1,0) . . . . .	
	(b) Tunnel rate from state (1,0) to (0,1) . . . . .	
	(c) Average switching frequency . . . . .	
	(d) Probability $P_R$ for being in the right dot . . . . .	
	(e) Example of a real-time trace . . . . .	
	(f) Temperature dependence of the tunneling rate . . . . .	115
45	(a) Time resolved four level system at the (0,0)-(1,1) transition . . . . .	
	(b) Histogram from real-time traces as in (a) . . . . .	
	(c) Equivalent histogram for a triple point (three level system) . . . . .	117
46	(a) Schematic of the (1,0)-(0,1) switching process . . . . .	
	(b) Schematic of the chemical potential around the (0,0)-(1,1) transition	
	(c),(d) Calculated tunneling rates . . . . .	
	(e),(f) Calculated switching frequency and occupation probability . . . . .	119
47	CEO wires under RF-irradiation at zero B-field . . . . .	125
48	CEO wires under RF-irradiation in an external B-field . . . . .	127
49	Zero B-field RF resonances versus temperature . . . . .	129

## Acknowledgment

The Physics Department at University Basel, though quite small, is well positioned among the world leading universities. Next to good experimental physics groups, University Basel hosts strong theory groups and a very good electronics and mechanics work shop. Together, these factors created a productive working environment throughout my PhD.

I would like to thank Prof. Dr. Dominik Zumbühl for giving me the opportunity to work in his group where all conditions are met to conduct research on an international top level. The independence and confidence I experienced were key to an intense learning process. I also wish to thank Prof. Dr. Dominik Zumbühl for his overturning inputs in moments of blockage and frustration.

Science is teamwork! This thesis was only possible due to the help of a large group of people who significantly contributed to the measurements and interpretations presented in this thesis. Without doubt, the body of this thesis are the measurements on CEO wires performed in collaboration with Prof. Dr. Amir Yacobys group at Harvard University in Cambridge USA. I acknowledge Prof. Dr. Amir Yacoby for many stimulating discussions and for providing these unique samples. I was lucky enough to have the opportunity to discuss the electron order and nuclear spin helix physics in person with all three authors from ref. [1], Dr. Bernd Braunecker, Prof. Dr. Pascal Simon and Prof. Dr. Daniel Loss. I especially acknowledge very intense and fruitful discussions with Dr. Bernd Braunecker and Prof. Dr. Daniel Loss. I benefited very much from Prof. Dr. Ophir Auslaenders expert knowledge on the double wire samples as well. I acknowledge Prof. Dr. Dmitrii L. Maslov for theory inputs and Dr. Tobias Meng for his efforts in trying to break things down to a simpler understanding level. I thank Dr. Tai-Min Liu, who joined the wire project toward the end of my PhD for the valuable teamwork.

The electron temperature measurements using a GaAs quantum dot were done with (former PhD) Dr. Sarah Heizmann on a sample fabricated by Kristine Bedner. I would like to thank both of them for all the good times we shared in the laboratory but also



outside the university. The low temperature measurements required the construction of cryogenic microwave filters beforehand. The extensive electronics know-how of Michael Steinachers proved to be of priceless value. I would like to thank Dominik Giss, who made his master project on this topic, for the contribution to the theoretical modeling of the filters which this thesis falls short of.

Electron temperatures were additionally analyzed by means of metallic coulomb blockade thermometers. This work was done in collaboration with Prof. Dr. Jukka Pekolas research group at Aalto University in Finland. Here I also want to acknowledge Dr. Matthias Meschke who fabricated the devices and with whom I performed initial measurements. Finally, only the active communication with the  $\mu$ -Kelvin team in our group allowed for construction of such an ultra low electron temperature setup. My special thanks goes to Lucas Casparis and Dario Maradan from the  $\mu$ -Kelvin team and to our former postdoc Dr. Tony Clark.

With Daniel Biesinger I spent a lot of time watching single electrons tunnel in real-time, recording big amounts of data and writing program codes to analyze it. Many thanks to him for the close collaboration on the metastable charge state project and also to Dr. Bernd Braunecker who immediately came up with a theory explaining our observations. In addition to people I worked with directly on a project, I was inspired by many discussions with group members but also other people in the house.

The fact that throughout my PhD technical problems were always solved smoothly, I owe to the electronics workshop with Michael Steinacher and the mechanics workshop, especially Patrick Stöcklin and Sasha Martin. Thanks to Dominik Sifrig for the reliable and flexible liquid helium deliveries.

I am also very thankful to Barbara Kammermann and Astrid Kalt who relieved me of any sort of administrative problems.

And of course, thanks to Joana, family and friends for all the good times outside the university.

# Curriculum Vitae

Christian Philipp Scheller

1997 - 2001	Gymnasium Kirschgarten, Basel
2001	Military service
2002	Summer semester at University of Louisville (UofL)
2002 - 2007	Studies at the Federal Institute of Technology (ETHZ)
Mar. - Aug. 2008	Diploma thesis at Paul Scherrer Institute (PSI)
Feb. 2009	Diploma in physics
2008 - 2013	PhD at University of Basel

## Publications

Christian P. Scheller, Tai-Min Liu, Amir Yacoby, Loren N. Pfeiffer, Ken W. West and Dominik M. Zumbühl, *Possible evidence for helical nuclear spin order in GaAs quantum wires*. Phys. Rev. Lett. **112**, 066801 (2014)

C.P. Scheller, S. Heizmann, K. Bedner, D. Giss, M. Meschke, D.M. Zumbühl, J.D. Zimmerman, and A.C. Gossard *Miniature Microwave Filters for Thermalization below 10 mK*. In preparation for publication.

Daniel E. F. Biesinger, Christian P. Scheller, Bernd Braunecker, J. Zimmerman, A.C. Gossard, and Dominik M. Zumbühl, *Intrinsic charge fluctuations in a few electron GaAs double quantum dot*. In preparation for publication.

L. Casparis, M. Meschke, D. Maradan, A. C. Clark, C. P. Scheller, K. K. Schwarzwälder, J. P. Pekola, D. M. Zumbühl, *Metallic Coulomb blockade thermometry down to 10 mK and below*. Rev. Sci. Instr. **88**, 083903 (2012)

D. Maradan, L. Casparis, T.-M. Liu, D. E. F. Biesinger, C. P. Scheller, D. M. Zumbühl, J. Zimmerman, and A. C. Gossard, *GaAs Quantum Dot Thermometry Using Direct Transport and Charge Sensing*. submitted to J. Low Temp. Phys. (2014)

Christian P. Scheller, Loren N. Pfeiffer, Ken W. West and Dominik M. Zumbühl, *One dimensional Fabry-Perot resonances in a GaAs quantum wire*. In preparation for publication.